DEVELOPMENT OF FABRICATION PROCESS TO PROTOTYPE A NOVEL ANNULAR THERMOELECTRIC GENERATOR DESIGN

Development of Fabrication Process to Prototype a Novel Annular Thermoelectric Generator Design

By

Mustafa Morsy, B.A.Sc. Engineering

A Thesis Submitted to the School
of Graduate Studies in Partial Fulfillment
of the Requirements for the Degree
Masters of Applied Science

McMaster University, Department of Mechanical Engineering

MASTERS OF APPLIED SCIENCE (2015) McMaster University
(Department of Mechanical Engineering) Hamilton, Ontario

TITLE: **Development of Fabrication Process to Prototype a Novel Annular Thermoelectric Generator Design**

AUTHOR: **Mustafa Morsy, B.A.Sc. Engineering (Ain Shams University)**

SUPERVISOR: **Dr. J.S. Cotton**

NUMBER OF PAGES: xv, 122

To my parents, my brother and the lady in my life

Abstract

The goal of this project is to develop a fabrication process for an annular thermoelectric module using a powder methodology that can potentially later be automated for high volume manufacturing. Prototypes were produced and experimentally tested to study and characterize thermal and effective Seebeck performance. Manufacturing procedure parameters were changed systematically to characterize the impact on key performance parameters and develop the fabrication process. Parameters investigated were sintering temperature, pressing pressure, oxide reduction and geometry.

A novel design for an annular thermoelectric generator geometry has been proposed. The new geometry utilizes more of the module material into power production making the geometry more efficient than the typical ring-structured modules similar to that proposed by Min & Rowe (2007). Experimental results tests highlighting only geometry differences showed V-shaped modules with higher effective Seebeck coefficient compared to ring-structured modules.

Experimental results showed the proposed V-shaped annular thermoelectric generator prototype with a Seebeck coefficient of 190.75 μV/K compared to (Min & Rowe, 2007)'s earlier ring-structured prototype measuring a Seebeck coefficient of 145 μV/K.

A numerical simulation model was created to compare electrical and thermal behaviour for different TEG module geometries. ANSYS Workbench® simulation results show that V-shaped TEG module outperforms the ring-structured design similar to Min et al.'s design by 7% to 9% under different conditions.

Acknowledgments

The author would like to express his gratitude to his supervisor Dr. James Cotton for his valuable guidance and support throughout the course of this M.A.Sc. Program. The author feels the necessity to acknowledge the work done in the project by Mr. Corbin Bruce. This research project is building on steps he initiated without the chance to cite his unpublished work.

The author would also like to give special thanks to Dr. Chan Ching for his support and advice on both the technical and personal level. Gratitude is also extended to the technicians, Mr. Ron Lodewyks, Mr. Mark MacKenzie, Mr. John Colenbrander, Mr. Joe Verhaeghe and Mr. Jim Garrett for their patient help. The author would like to express his cordial appreciation to the TMRL team for their team spirits and guidance throughout the project. It has been truly inspiring being part of the team. Tremendous gratitude falls in place to the wizard behind the scene and a key contributor for every project in the TMRL lab, Dr. Hossam Sadek.

The author would like express his special gratitude to all his family members for their continuous support throughout the course of this program. They always provided him with solid support and encouragement in all his endeavors, whether it was a success or failure.

Table of Contents

List of Tables

List of Figures

Nomenclature

Symbol / Acronym	Description	Applicable units
T_{1a}	Hot block 1, 1st thermocouple from the TEG test section	°C
T_{1b}	Hot block 1, 2nd thermocouple from the TEG test section	°C
T_{1c}	Hot block 1, 3rd thermocouple from the TEG test section	°C
T_{1d}	Hot block 1, 4th thermocouple from the TEG test section	°C
T_{2a}	Hot block 2, 1st thermocouple from the TEG test section	°C
T_{2b}	Hot block 2, 2nd thermocouple from the TEG test section	°C
T_{2c}	Hot block 2, 3rd thermocouple from the TEG test section	°C
T_{2d}	Hot block 2, 4th thermocouple from the TEG test section	°C
T_{3a}	Hot block 3, 1st thermocouple from the TEG test section	°C
T_{3b}	Hot block 3, 2nd thermocouple from the TEG test section	°C
T_{3c}	Hot block 3, 3rd thermocouple from the TEG test section	°C
T_{3d}	Hot block 3, 4th thermocouple from the TEG test section	°C
$T_{water\ in\ 1}$	Cold water temperature at inlet mixing chamber	°C
$T_{water\ in\ 2}$	Cold water temperature at inlet mixing chamber	°C
$T_{water\ in\ 3}$	Cold water temperature at inlet mixing chamber	°C
$T_{water\ out\ 1}$	Cold water temperature at outlet mixing chamber	°C
$T_{water\ out\ 2}$	Cold water temperature at outlet mixing chamber	°C
$T_{water\ out\ 3}$	Cold water temperature at outlet mixing chamber	°C
V_{output}	Output Voltage of TEG module	mV
V_{OC}	Open Circuit Voltage output of TEG module	mV
I_{output}	Output Current of TEG module	A
$R_{external}$	External Resistance added to the circuit	Ω
R_{TEG}	Internal Resistance of the TEG module	Ω
$V_{input\ heater}$	Input Voltage of both heaters combined	V
$I_{input\ heater}$	Input Current of both heater combined	A
V'_{water}	Volumetric Flow Rate of water	l/min
Q_w , Q_{water}	Heat transfer to the chilled water	W
Q_H, $Q_{Hot\ Block}$	Heat transfer through the Hot block	W
T_{Hot}	Temperature of TEG hot side	°C
T_{Cold}	Temperature of TEG cold side	°C
ΔT_{TEG}	Differential temperature over TEG module	°C
$T_{TEG\ avg}$	Average temperature over the TEG module	°C
α	Seebeck Coefficient	μV/K
$T_{water\ average}$	Average Chilled water temperature through the test section	°C
TEG	Thermoelectric Generator	

Chapter 1: Introduction to Thermo-Electrics

1. Introduction to Thermo-Electrics

In the recent two decades, the interest in thermo-electrics has been increasing rapidly. To quantify the interest increase, the number of papers published about thermos-electrics were compared. The papers published in 2007 about thermo-electrics are more than twice the papers published in 1997 (J. Yang, 2005; Zheng, 2008). Though that increase in interest, thermoelectric materials are not a new discovery. In fact the physical phenomenon of thermoelectrics was discovered 200 years ago by Thomas Seebeck. In this chapter, principles of thermoelectrics will be discussed along with recent thermoelectric research developments and motivation behind recent interest of thermoelectric materials.

1.1 Seebeck Effect

In 1821 Thomas Johann Seebeck (1770-1831, a German Physicist) noticed that two connected dissimilar metals under a differential temperature altered the compass arrow direction resulting from an electric current flowing. Seebeck was experimenting the magnetization of different material pairs, when he observed a measurable current flowing between a bismuth and copper rods while heating the junction as shown in Figure 1. The phenomenon works on any dissimilar metals connected (Britannica, n.d.).

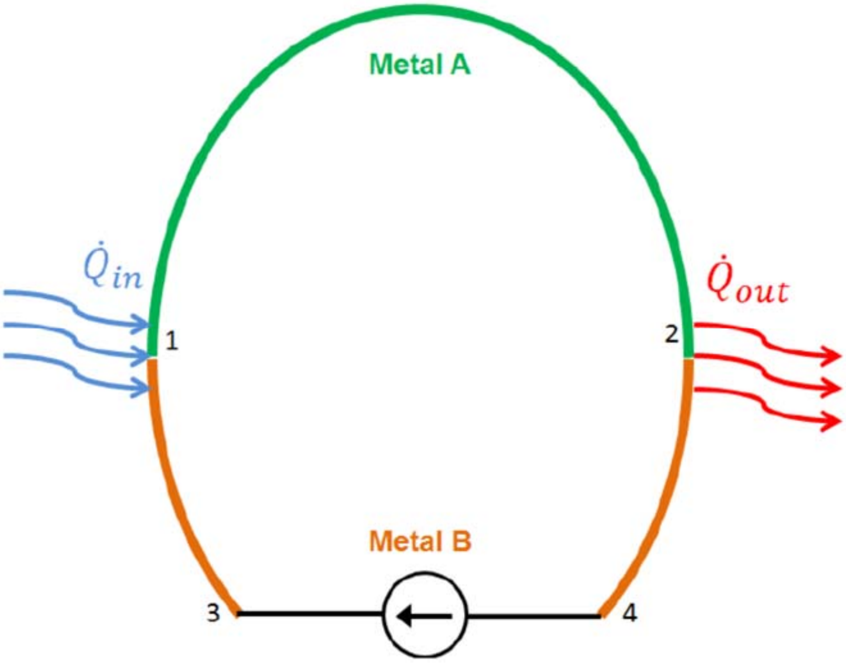

Figure 1- Seebeck effect diagram (Cino, 2014)

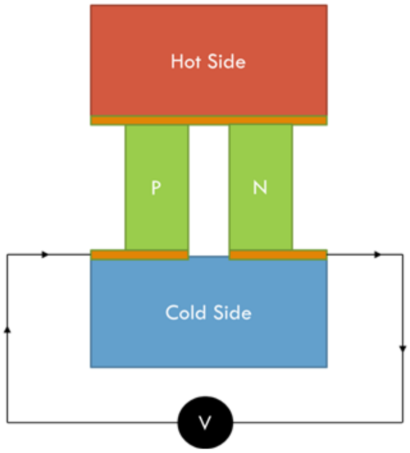

Electrons flowing Due to Seebeck Effect

Figure 2- Thermoelectric Module 1 thermoelectric couple (P&N)

Seebeck coefficient is a material property that determines its capacity to produce voltage when put under a differential temperature. Based on the fact that electrons act as a carrier for both heat and electricity, a differential temperature on an electric conductive rod would cause a net diffusion of electrons from the hot end towards the cold end creating an opposing electric field (Moffat, 1997). Seebeck coefficient can be defined as the voltage produced for a unit temperature difference over the material.

$$\alpha_{couple} = \frac{V_{Produced}}{\Delta T_{TEG}} \qquad \text{Eq. 1. 1}$$

α_{couple} = Seebeck coefficient for the couple (p & n junctions)

ΔT_{TEG} = Temperature Difference

The asymmetry of the electron distribution around the Fermi level determines the sign and magnitude of the material (Moffat, 1997). That is, the sign of the Seebeck coefficient is based on the majority of charge carriers in the material, (i.e. positively doped material would have a positive Seebeck coefficient). Seebeck coefficient depends as well on the cell structural composition of the material and the temperature.

The representation of Seebeck coefficient has to be in a relative manner (in most cases are relative to Platinum). The Seebeck coefficient of a thermoelectric couple can be calculated by subtracting Seebeck coefficient values for both p & n junctions. Therefore, for a thermocouple, putting materials with the highest plus and minus Seebeck coefficient would be preferred. Another important factor when choosing materials for a temperature measurement thermocouple, is the robustness of the material such that it could be shaped into wires to use for measurement. The latter is the main reason why commercial temperature measurement thermocouples are usually made from metals that does not necessarily have a high Seebeck coefficient.

1.2 Peltier Effect

Peltier effect is the physical phenomenon of a differential temperature forming across the module when an electric current is applied through the material. The application of electric current forces causes heat to flow from one side to the other creating a cold side on one end and a hot side on the other as shown in Figure 3.

This phenomenon can be used as a solid state alternative for cooling. It is named after its discoverer, French physicist Jean-Charles Peltier in 1834. Peltier effect can be defined as the amount of heat carried per unit charge. Today, more applications are utilizing Peltier effect for solid state cooling than Seebeck effect in power generation.

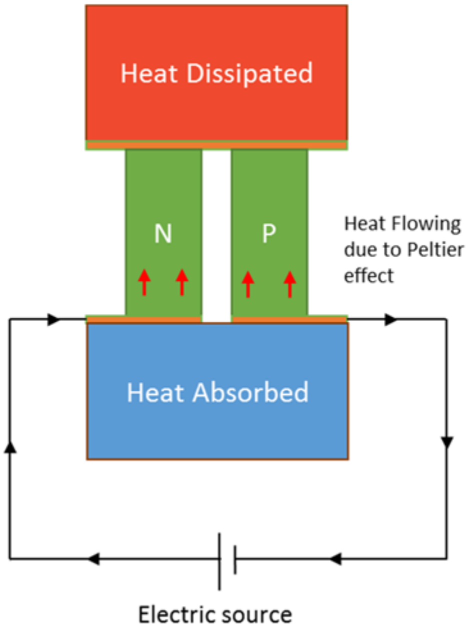

Figure 3- Peltier Effect on a thermoelectric module (1 couple)

1.3 Thomson Effect

Lord Kelvin was investigating Seebeck and Peltier effect in 1851 when he discovered the Thomson effect. Kelvin found that current flowing through the thermoelectric material causes a temperature change due to joule heating. The temperature gradient across the thermoelectric module is the combination of heating or cooling exerted on the module and joule heating due to flowing electric current. The heat flowing through the module is affected by the electric current flowing causing Peltier effect and therefore changes the overall performance of the module.

Seebeck effect usually varies over temperature. When exerting a differential temperature on a module, it forms a spectrum of changing Seebeck coefficients due to temperature gradient. The Thomson effect results from the change of Seebeck coefficient as a function of temperature. Seebeck effect, Peltier effect and joule heating are not isolated phenomena, they exist concurrently and affect the overall performance. Thomson effect can better forecast a realistic steady state performance of the module.

1.4 Carrier concentration and Figure of Merit

Thermal conductivity increases with the increase of material carrier concentration. Materials with low carrier concentration have a low thermal conductivity, insulators. Materials with high carrier concentration have a high thermal conductivity, called conductors or metals. In between these two categories falls the semi-conductors area. Similarly, electrical conductivity increases with the increase of material carrier concentration as well. The Seebeck coefficient, it decreases with the increase of carrier concentration. That means that the higher the carrier concentration, the lower the Seebeck coefficient is for the material (as shown in Figure 4).

For a thermoelectric material, a low thermal conductivity would be preferred to exert a high thermal resistance, therefore creating a differential temperature between the two ends of the module that is as large as possible. To maximize the current produced by the module, electrical conductivity is maximized. Since both thermal and electrical conductivities increase with the increase of carrier concentration, it is impossible to satisfy both minimizing thermal conductivity and maximizing electrical conductivity. To maximize the performance of the thermo-electrical material, a point in-between has to be found.

Figure of Merit is a dimensionless parameter that describes the ability of the material to efficiently produce thermoelectric power. It can be calculated as follows:

$$ZT = \frac{\sigma\, \alpha^2\, T}{\lambda} \qquad \text{Eq. 1. 2}$$

where,

Z : Figure of Merit

σ : Electrical Conductivity

λ : Thermal Conductivity

α : Seebeck coefficient

T : Temperature

Using Figure of Merit to determine optimum performance, a maximum over the spectrum of carrier concentrations has been found to be $1\text{x}10^{19}$ cm^{-3} (Rowe et al., 2006) as shown in Figure 4.

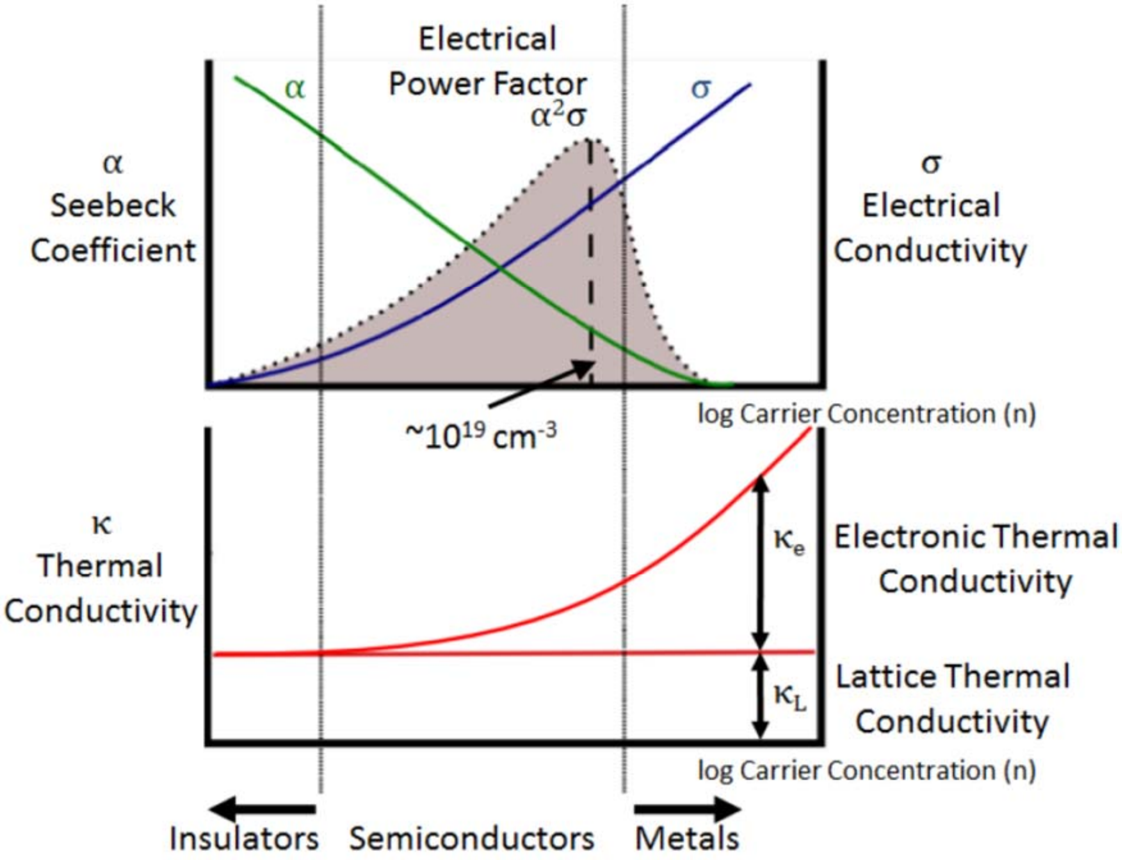

Figure 4- Schematic dependence of electrical conductivity, Seebeck coefficient, power factor, and thermal conductivity on carrier concentration, (Cino, 2014)*, reconstructed from* (Rowe et al., 2006)

1.5 Thermoelectric research timeline

The concept of using thermoelectric materials to produce electricity is not a recent discovery. Figure 5 shows the number of papers on thermoelectric materials published as a function of year from 1955 to 2007. There are two main periods with increasing interest in thermoelectric material research. In the period 1945-1970 interest was increasing in thermoelectric materials as for the interest in space research. In 1965, researchers claimed that Figure of Merit (ZT) of any material can never exceed 1 due to contradiction of needed high electrical conductivity and low thermal conductivity for the same material (Zheng, 2008). Figure 6 shows progress in ZT performance of thermoelectric materials as a function of year. Since 1995 and the advances of Nano material research, ZT values of prototypes have significantly increased to as high as 3.5 and is expected to improve more in the upcoming years.

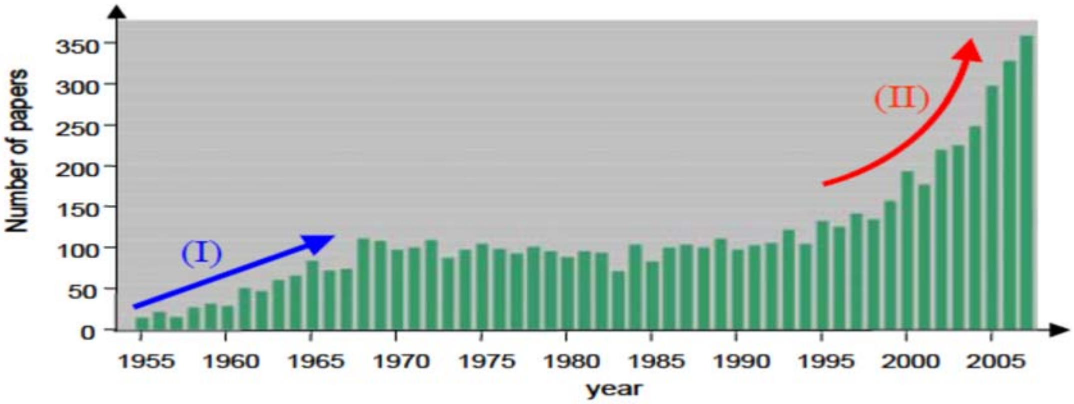

Figure 5- Number of papers on thermoelectric materials published as a function of year from 1955 to 2007 (Zheng, 2008)

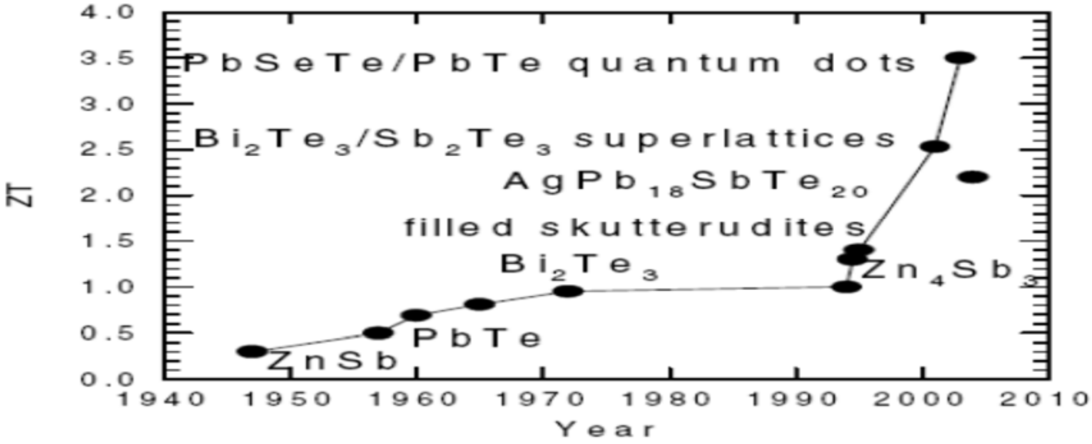

Figure 6- ZT of many typical thermoelectric materials as a function of year (Zheng, 2008)

1.6 Research motivation

The interest in thermoelectric generator materials has been increasing since 1995 with the advance in Nano material research and the promise of manipulating coupled material properties separately. The amount of annual published papers about thermoelectrics is doubling every five years (Zheng, 2008). Although the Figure of Merit value of current commercially available materials is relatively low, the rate of recent advances holds promise for new efficient thermoelectric materials.

Most of today's thermoelectric generator modules rely on a flat plate design. Flat plate TEG modules are manufactured manually in a labour intensive operation that results in an inconsistent performance (Finnerty, 2013). Flat plates are fine to use with applications where heat flows from a flat surface. But in applications where heat flows radially, it becomes very challenging to fit flat plate TEG modules on cylindrical surfaces, especially when the diameter of the heat source gets smaller than 1 cm (Min & Rowe, 2007). Therefore the need for an annular TEG module has been proposed (Weinberg et al., 2002 (a); 2002 (b)). Min & Rowe (2007) produced and tested a novel ring-structured thermoelectric module prototype. Schmitz et al. (2013) built on that initial step and produced a second ring-structured or annular thermoelectric module prototype using a more innovative manufacturing methodology, however performance results were not reported.

This research is aimed to study, produce, and test a novel annular thermoelectric generator design using a powder metallurgy methodology that can be automated. Powder metallurgy is a multi-direction grain growth method through pressing the material powder. Key manufacturing parameters were studied to develop the fabrication process. Parameters investigated includes sintering temperature, pressing pressure, geometry and oxidation.

Chapter 2: Literature Review

2. Literature Review

A thermoelectric generator (TEG) module is typically made to produce electricity from a heat source. Although a lot of research has been done to develop innovative shaped modules, most of these modules rely on the flat plate concept. Figure 7 shows a typical flat plate TEG with p & n type cube elements connected alternatively in series through a metallic contact (copper in this case). The outer ceramic plate is used as both a heat conductor and for electric insulation. This flat plate TEG module arrangement is used in most commercially produced TEGs.

Flat plates are fine to use with applications where heat flows from a flat surface. But in application where heat flows radially, it becomes very challenging to fit flat plate TEG modules on cylindrical surfaces, especially when the diameter of the heat source less than 1 cm (Min & Rowe, 2007). Therefore the need for cylinder or tube shaped TEG modules for such applications was proposed (Weinberg et al., 2002(a); 2002(b)). Arranging multiple ring-shaped p and n type junctions in series would form the mentioned tube TEG module as shown in Figure 8. Only few prototype modules were reported to be manufactured and will be discussed in the next section.

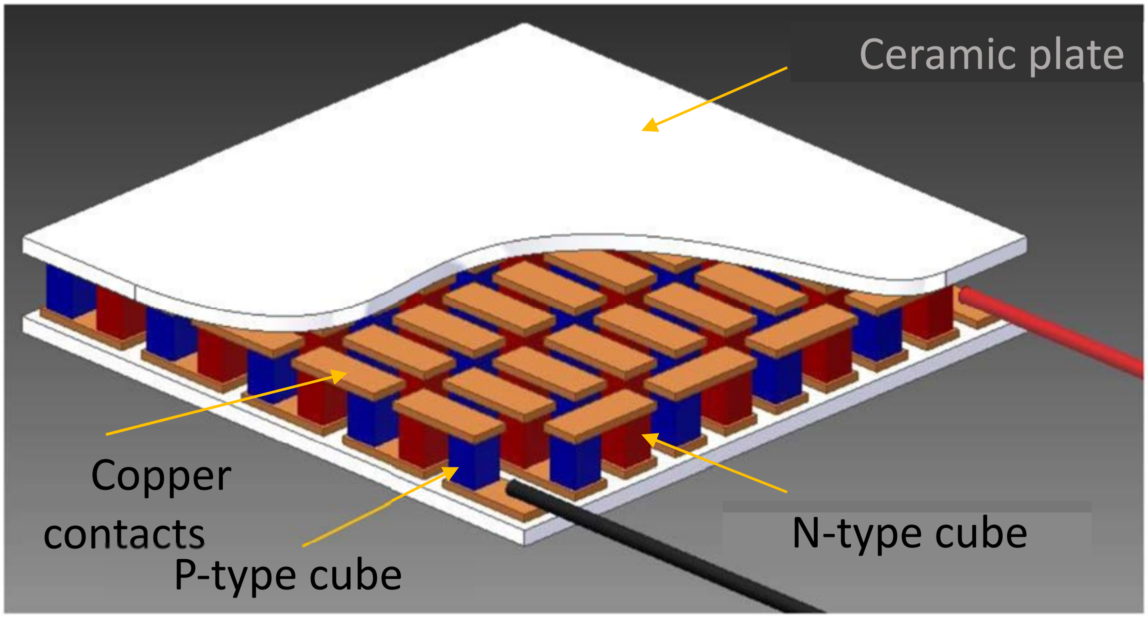

Figure 7- Typical arrangement for a flat plate TEG module (Cino, 2014)

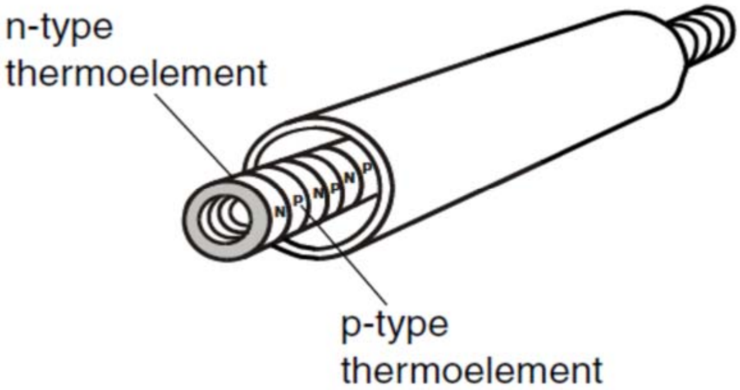

Figure 8- P-type and n-type rings arranged in series to form a tube shaped TEG module (Min & Rowe, 2007)

2.1 Ring-Structured Prototypes

Min & Rowe (2007) developed a prototype of ring-structured thermoelectric module as a proof of concept and investigated its performance theoretically and experimentally.

The proposed a prototype that would be the base of a tube shaped thermoelectric module that consists of a large number of coaxial rings, Figure 9. The design proposed flat p-type and n-type thermoelectric washers or ring-structured modules to be arranged alternating. In between thermoelectric rings, a copper washer was put either on the inner or the outer edge alternately creating hot and cold junctions. Vacant spaces within the arrangement was filled with a thermally and electrically insulating material. The arrangement would be creating a ‘thermoelectric tube’ with the inner surface creating one side (hot or cold) and the outer surface creating the other (Min & Rowe, 2007).

A prototype was created of 2 p-type and 2 n-type rings fabricated from Bridgeman grown ingot of Bi_2Te_3 based alloys. The 14mm diameter ingot was cut into 2mm thick discs. These disks were made into rings using spark-erosion to cut a 6.4mm inner diameter. Copper rings were made with outer and inner diameters 14mm, 12mm and 8.4mm, 6.4mm for the rings on the outer edge and inner edge respectively. This prototype was tested and compared against theoretical values from the analytical model.

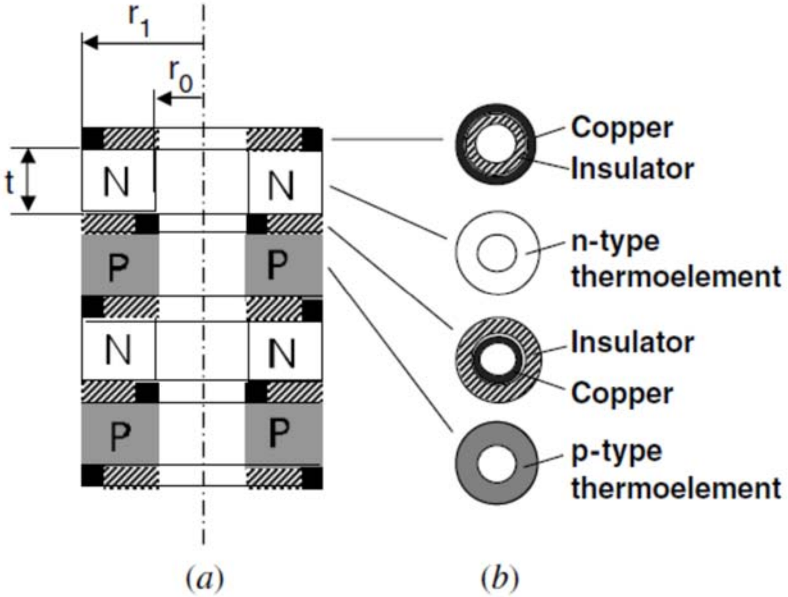

Figure 9 - Ring-structured thermoelectric module: (a) side elevation and (b) plane view (compressed). r_0 and r_1 are the inner and outer diameters for the thermoelectric ring respectively and t is the thickness of each ring (Min & Rowe, 2007)

Min & Rowe developed an analytical model for estimating the expected performance of a ring-structured thermoelectric generator. It is assumed that both p-type and n-type have very similar thermoelectric properties for simplification,

$$\left|\alpha_p\right| = |\alpha_n| = \alpha \qquad \text{Eq. 2. 1}$$

$$\rho_p = \rho_n = \bar{\rho} \qquad \text{Eq. 2. 2}$$

$$\lambda_p = \lambda_n = \bar{\lambda} \qquad \text{Eq. 2. 3}$$

where,

α : Seebeck coefficient

ρ : Electrical resistivity

λ : Thermal conductivity

The electrical resistance of a single ring structure (*R*) can be expressed as

$$R = \int_{r_0}^{r_1} \frac{\rho(r)}{2\pi t r}\, dr = \frac{(\rho_n+\rho_p)}{\pi t}\, ln(\frac{r_1}{r_0}) \qquad \text{Eq. 2. 4}$$

where,

t : Thickness

r_1 : Outer radius of the ring

r_0 : Inner radius of the ring

The thermal conductance of a single ring structure (*K*) can be expressed as

$$K = \frac{2\,(\lambda_n+\lambda_p)\pi t}{ln(r_1/r_0)} \qquad \text{Eq. 2. 5}$$

Figure of Merit (*Z*) can be expressed as

$$Z = \frac{(\alpha_n-\alpha_p)^2}{R\,K} = \frac{\alpha^2}{\rho\lambda} \qquad \text{Eq. 2. 6}$$

Conventional efficiency (*Φ*) can be expressed as

$$\phi = \frac{T_h-T_c}{T_h} \cdot \frac{(1+Z\bar{T})^{1/2}-1}{(1+Z\bar{T})^{1/2}+T_c/T_h} \qquad \text{Eq. 2. 7}$$

where,

T_h : Absolute temperature of the hot junction

T_c : Absolute temperature of the cold junction

$\bar{T}$: Average temperature of the cold and the hot junction $\frac{T_H+T_C}{2}$

Maximum power output (*P_{max}*) for a thermoelectric tube

$$P_{max} = \frac{V^2}{4R} \qquad \text{Eq. 2. 8}$$

Where (*V*) is the voltage output of a thermocouple and can be expressed as

$$V = \alpha(T_h - T_c) \qquad \text{Eq. 2. 9}$$

Therefore,

$$P_{max} = \frac{N\pi t\left(\alpha_n - \alpha_p\right)^2 (T_h - T_c)^2}{2\left(\rho_n + \rho_p\right) ln(r_0/r_1)} = \frac{N\pi t\alpha^2 (T_h - T_c)^2}{\rho\, ln(r_0/r_1)} \qquad \text{Eq. 2. 10}$$

where,

N : number of thermocouples in a thermoelectric converter

Equations mentioned above are based on the assumption that contact resistance is negligible and that heat and electricity are only flowing radially (Min & Rowe, 2007).

Min & Rowe conducted an experimental investigation to the proposed prototype. It was created of 2 p-type and 2 n-type rings fabricated from Bridgeman grown ingot of Bi_2Te_3 based alloys, Figure 9. The contact areas on the thermoelectric rings were coated with a thin layer of $Bi_{0.95}Sb_{0.05}$ and vacant spaces within the assembly were filled with mica rings. The assembly was then put in a furnace at 200^o C for 15 min for annealing.

Using techniques reported in Rowe & Min (1998), Power output was obtained measuring open circuit voltage and short circuit current while exerting a differential temperature on the thermoelectric module prototype. To create the differential temperatures across the junctions, hot water was flowing inside the TEG module while the outside surface was kept cold by putting the test section into a cold water bath as shown in Figure 10. The water was assumed isothermal on the outer surface of the TEG pipe although it was stagnant and no energy balance was made for the test facility.

Thermoelectric materials fabricated using a single crystal growth method creates a material ingot with different properties in the growth direction (axial) than in the perpendicular direction (radial). The ingot has a lower thermal conductivity perpendicular to the growth direction, Therefore, heat is preferred to flow in the perpendicular direction to crystal growth to create a higher temperature gradient. In Figure 11, three results are presented in which show the experimental data, compared to analytical calculation using the prototype effective Seebeck coefficient (fabricated with its radius perpendicular to the preferred direction) and analytical calculation using the material Seebeck coefficient (if fabricated with its radius along the preferred orientation) (Min & Rowe, 2007). Results show experimental measured performance to be lower than the analytical model. Effective Seebeck coefficient describes the measured Seebeck coefficient of the TEG module after assembly which factors in the contact resistance, heat flow pattern and geometry.

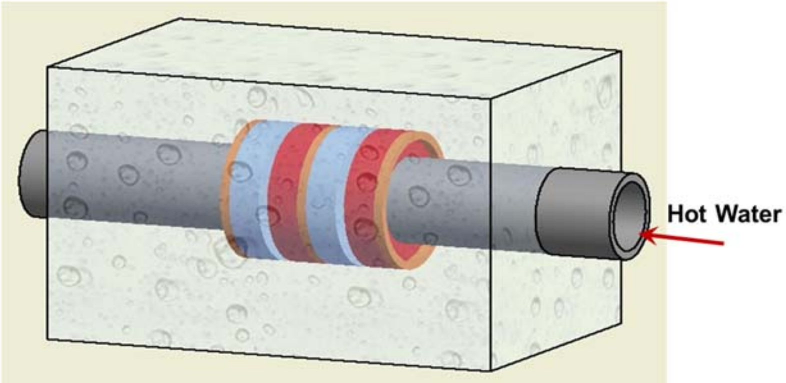

Figure 10- The test arrangement used by Rowe to test the ring-shaped thermoelectric modules

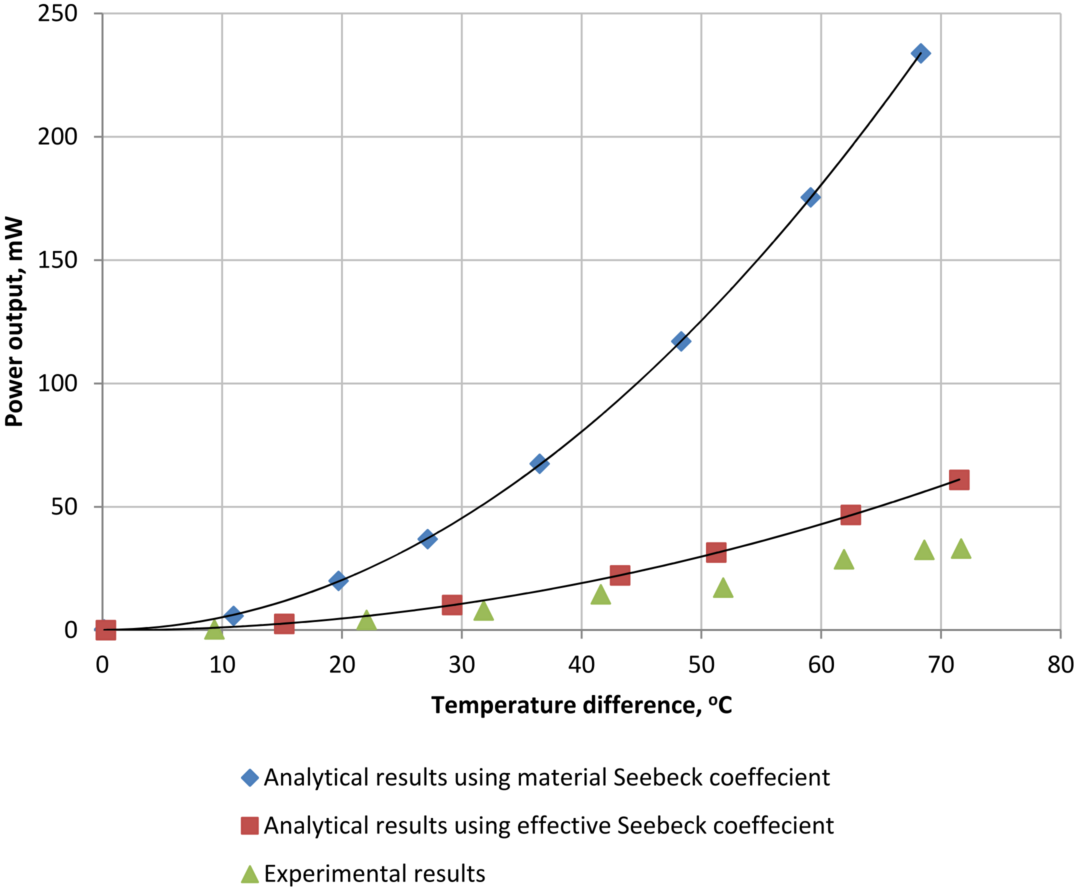

Figure 11- Power output of Min & Rowe's prototype as a function of temperature differences. comparing experimental data and analytical models using material and effective Seebeck coefficients, reconstructed using data from (Min & Rowe, 2007)

One of the issues that affected experimental results was that during preparation of thermoelectric rings, they were cut in the axial direction of the ingot and perpendicular to the grain growth direction, which means that electricity flowing radially is not flowing in the preferred direction and the acting electrical resistivity value is higher. Electrical resistivity in the radial direction of the ring is 2.32×10^{-3} Ω cm compared with the grain growth direction (axial) which is 1.05×10^{-3} Ω cm. Since electricity in the prototype is flowing radially, the samples are expected to generate less current. Min & Rowe reported a measured Seebeck coefficient of the rings after contact formation is 145 μ V K^{-1} compared to the theoretical value of the material 201 μ V K^{-1} which they reported to be due to poor contact between thermoelectric rings in the prototype.

Min & Rowe produced a novel prototype as a proof of concept representing a ring shaped thermoelectric generator module. The prototype performance did not match analytically predicted performance due to several reasons including contact resistance between thermoelectric rings and heat flowing perpendicular to the preferred direction.

More recently, Schmitz et al. (2013) produced a similarly configured thermoelectric ring shaped module. Unlike Min & Rowe, Schmitz et al. used a different manufacturing methodology as well as a different design for conductor rings.

This thermoelectric generator was designed for an EGR Cooler of a diesel engine. An EGR Cooler is a heat exchanger that cools down recirculated exhaust gases before introducing them into the engine intake gas to lower NO_x emissions. Twenty p-n couples would be mounted to form a thermoelectric tube, with sixteen of these pipes mounted in parallel to forms the heat exchanger. Typically within an automobile application gases forms the hot side or heat source while the cold side is the liquid coolant. To study this application, a prototype was proposed and fabricated for a portion of the TEG module (only 2 p-type & 2 n-type rings).

Schmitz et al built on the same concept prototype Min & Rowe fabricated. The radial heat flow concept was adopted but a different geometrical arrangement and manufacturing methodology was employed. The prototype produced by Schmitz et al. had p-type and n-type thermoelectric rings alternately arranged coaxially. To prevent an electrical short circuit, insulative washers separate the thermoelectric rings. A nickel cylindrical bridge was put on the outer and the inner surface creating Hot and Cold junctions as shown in Figure 12. The Figure compares assemblies made by Schmitz et al. and Min & Rowe showing the difference in the metal conductor position.

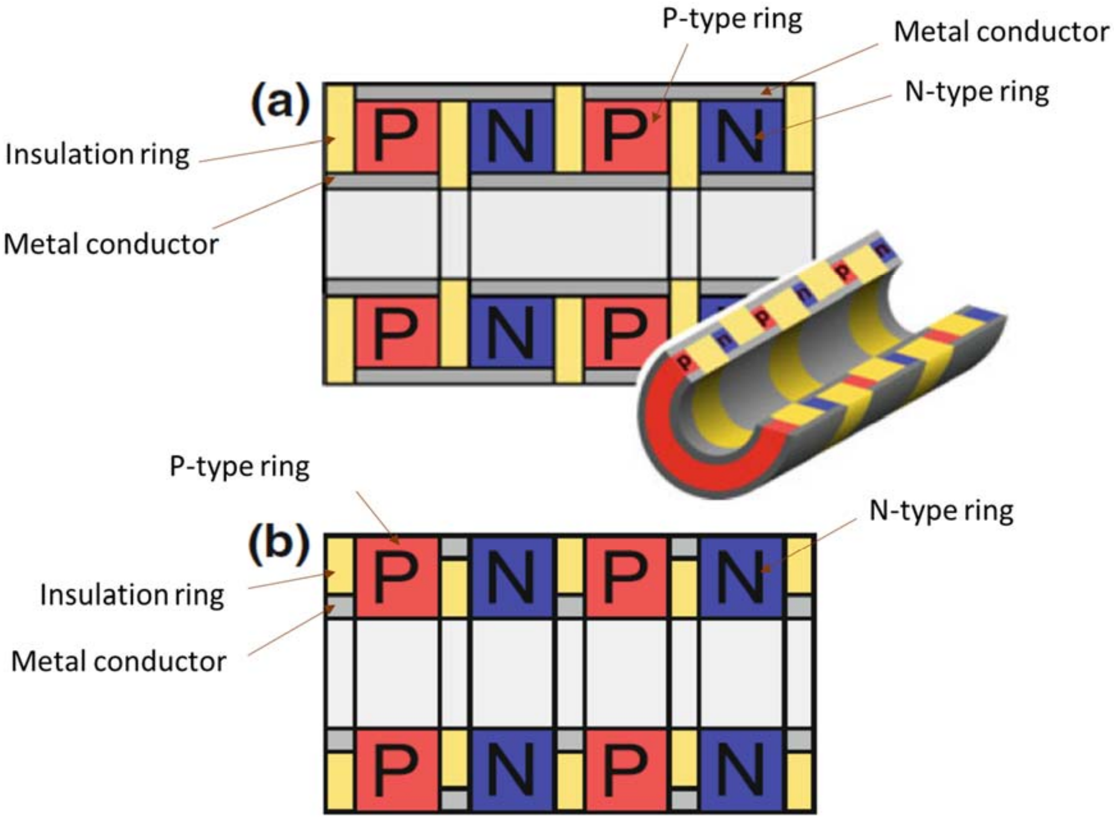

Figure 12- Section drawing of a tubular TE module (a) as proposed by Schmitz (b) as proposed by Gao Min *(Schmitz et al., 2013)*

Min et al proposed that one of the reasons that caused their prototype not to achieve theoretical performance values was heat flow perpendicular to the preferred direction of crystal growth of the sample. Using crystal growth as a manufacturing method initially made it impossible for heat to flow in the preferred direction in a ring module. Therefore, Schmitz et al. moved to a powder methodology to fabricate their samples, hot pressing in particular. Different manufacturing methodologies will be discussed in the upcoming chapter.

One of the most important and novel contributions for Schmitz et al. is the discussion and methodology for hot pressing thermoelectric rings or hollow cylindrical shaped modules. Lead telluride (the material used in his research, but same concept applies for others) has a relatively high thermal expansion coefficient of 20 x 10^{-6} K^{-1}. When hot pressing disc specimen, grains forms at sintering temperature, then while cooling down shrink more than the die material, which usually has a lower thermal expansion. This provides sufficient clearance from the outer surface for extraction from the die. For ring modules, the die would include an internal rod to form the hollow center as shown in Figure 13. If made from the same die material, typically graphite, the thermoelectric ring would shrink more than the internal rod. Thus, an internal shaft with a different material that has a slightly higher thermal expansion was used. This cause it to shrink more than the thermoelectric ring leaving room on the inner surface for removal from the die. Silver, aluminum and cobalt have higher thermal expansion value, but cannot be used as they have a low young modulus on higher temperatures which would limit the pressure used during hot pressing. To overcome that, a special alloy was needed (Schmitz et al., 2013).

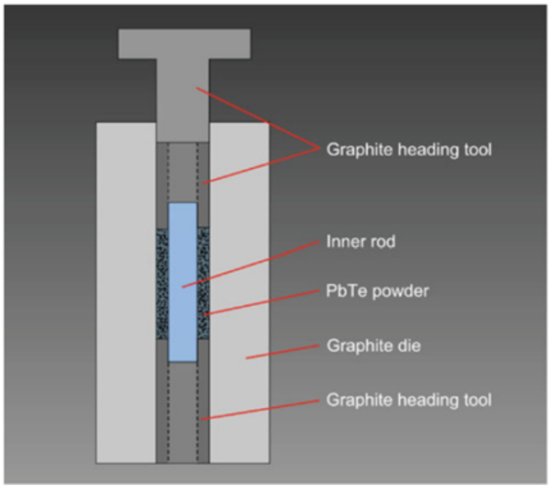

Figure 13- Sectional view of the sintering mold construction. The material of the inner rod is chosen to match the CTE of the thermoelectric material. Both heading tools are constructed as tubes, so that the inner rod can be pushed out of the mold after sintering without removing the sintered sample *(Schmitz et al., 2013)*

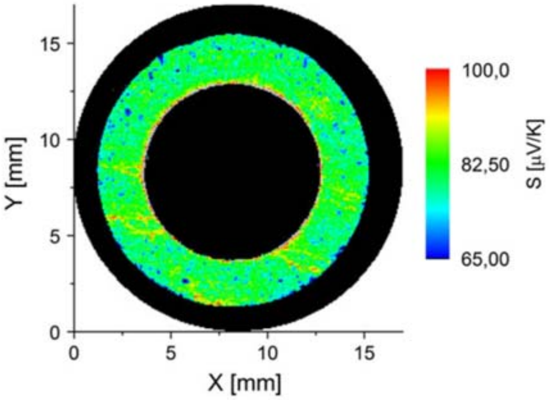

Figure 14- Scan of the Seebeck coefficient's local distribution on the surface of a p-type lead telluride ring cut from a sintered tube. No macroscopic inhomogeneity is observed. Cracks at 5 and 8 o'clock are clear *(Schmitz et al., 2013)*

Although every precaution was made during the sintering process, cracks in the produced samples were never eliminated. Produced prototype rings were scanned using Potential-Seebeck Microprobe (PSM). Figure 14 shows clear cracks at the 5 and 8 o'clock positions. Schmitz claimed that the internal cracks were a result of hot embedding of the ring required for the measurement. PSM applies a heated probe tip at the surface to measure Seebeck coefficient at that point.

Characterization and performance experimental tests were not made at the time the paper was published (2013) and is not known to be reported yet. Schmitz mentioned that it would be reported in a later publication.

2.2 Commercial flat plate TEG module

Commercially produced TEG modules currently available are all based on a flat plate design. Production of such modules is labour intensive, therefore almost all these units are produced in China, Taiwan and Vietnam where labour cost is considerably less expensive. In the next section the current manufacturing methodology and experimental performance results of these modules will be discussed. TEG materials can be produced using either Crystal Growth or Powder methodologies. Current commercial TEG modules use the crystal growth method while a lot of research prototypes utilize the powder methodology.

The first step of manufacturing is the production of the thermoelectric material. The Bridgman Growth method, which is a crystal growth method, is commonly used. In this method the material is melted into a quartz ampoule that has a pointed edge at the bottom. When solidifying the material, solidification starts from the bottom tip of the ampoule creating the origin single crystal. Then the cooler temperature front is moved slowly upward preserving crystal formation in the axial direction and producing a rod of the thermoelectric material.

After the rods are formed, 25-40% of the rod is removed from both ends as rod ends have lower thermoelectric properties. The remaining part of the rod is chopped radially into around 1 mm thickness discs, then sliced into cubes. Cubes formed are rotated 90 degrees and arranged into alternative P and N series connection to form thermoelectric couples as shown schematically in Figure 7 and photograph in Figure 15. Arranging, soldering (cold side) and flame brazing (hot side) thermoelectric cubes and conductors to the ceramic plate is done manually. Therefore, it is a labour intensive process and the end product TEG module performance is inconsistent. Finnerty (2013) tested several Flat plate TEG modules where their performance in some cases varied as much as 50%, (Figure 17) and typically were below the manufacturer suggested performance rating. Figure 15 and Figure 16 show the inconsistency and irregular soldering and flame brazing thicknesses.

Using this method for TEG modules manufacturing wastes 25-40% of the material. Thermoelectric properties varies over the length of the rod, therefore TEG modules manufactured from different portions of the rod would perform differently. Manual labour cost limits ability to produce such products cost effectively at high volumes. Moving to an automated manufacturing methodology is a necessity that would boost TEG modules performance and consistency. Powder methodology appears to be potential candidate when it comes to producing ring-structured modules.

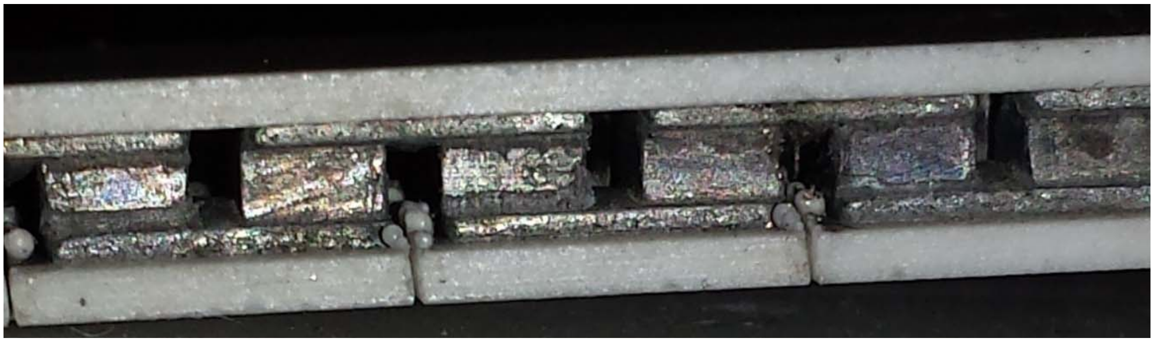

Figure 15 – Image of a commercial flat plate TEG module, irregular soldering and inconsistency are visible

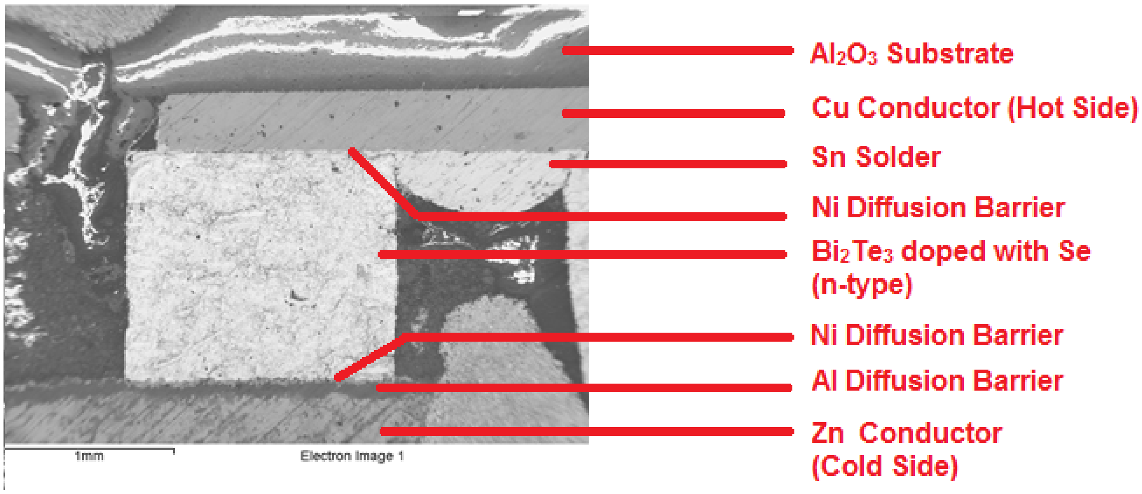

Figure 16 - a commercial flat plate TEG module, irregular soldering is visible (Cino, 2014)

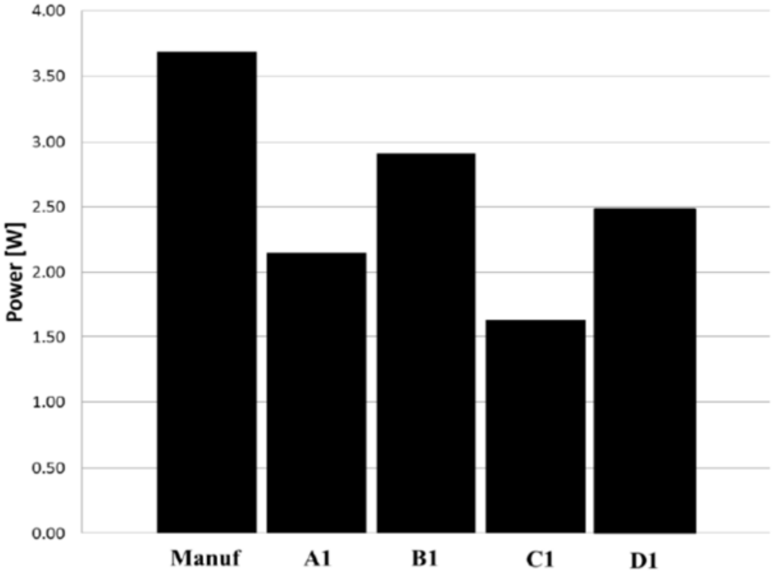

Figure 17 – Commercial Flat plate TEG modules measured performance worse than reported by manufacturer (Finnerty, 2013)

Chapter Three: Literature review; Manufacturing TEG modules using Powder methodology

3. Literature review; Manufacturing TEG modules using Powder methodology

Using powder metallurgy methodology to create an automated and consistent manufacturing methodology for TEG geometries and materials has been researched extensively. In this Chapter, different powder methodology methods will be reviewed and discussed. Previous powder methodology studies produced solid cylinder shaped prototype ingots to measure resultant thermoelectric properties. This research aimed to integrate means of using powder methodology into producing ring-structured thermoelectric generator modules.

To produce a solid ingot using powder metallurgy, typically material mechanically alloyed powder would go through three main steps or more. The first step is preparing the existing mechanical alloyed powder by reducing its oxidized content. Second step is pressing the powder into the proposed sample shape using a die. Third step is sintering at elevated temperatures to allow multi-directional crystal formation to take place. Second and third steps can take place simultaneously or separately depending on the methodology. Some of the reported work has started from raw material in the form of pure bismuth, telluride and dopants, but this research will focus on the fabrication process of previously mechanically alloyed powders. This chapter will discuss different examples of reported work done concerning these three main steps starting with the first step.

3.1 Oxides Contamination and Reduction

First step is to prepare the mechanically alloyed powder for pressing. Powder stored gets contaminated by oxygen over time, therefore prior to any manufacturing process, powder must be cured first and restored to its original composition. The process of oxidation of Bi_2Te_3 was investigated by Bando et al. (2000) with X-ray photoelectron spectroscopy (XPS). To perform his investigation, samples of bismuth telluride were prepared then left in a 24°C air environment with 30% humidity. Samples were then scanned with XPS over hourly intervals to detect the oxide layer thickness over powder grains. An oxide layer of the thermoelectric material has been found to contain Bi_2O_3 and TeO_3. From the results shown in Figure 18 and Figure 19, it is noticed that over the first 100 hours it was found to be a rapid process where bismuth telluride grains developed a 1.25nm thick oxide layer. It grew linearly with exposure time after that where bismuth telluride developed an additional 0.5nm thick oxide layer every 1000 hours.

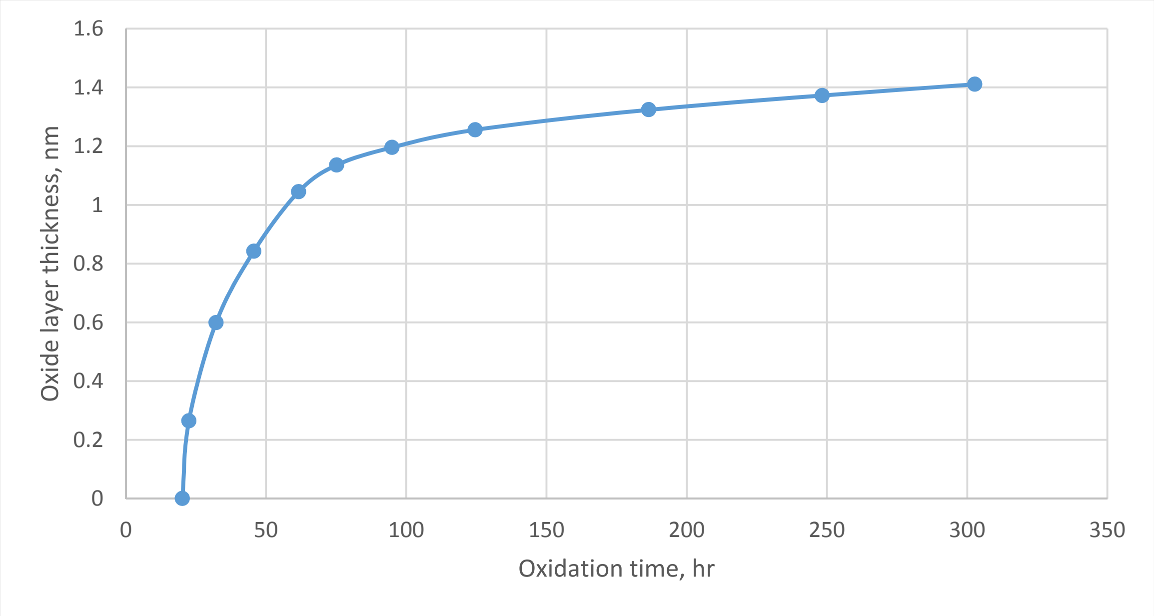

Figure 18 – Oxide contamination over a short time (300 hr and less) for bismuth telluride, reconstructed from (Bando et al., 2000)

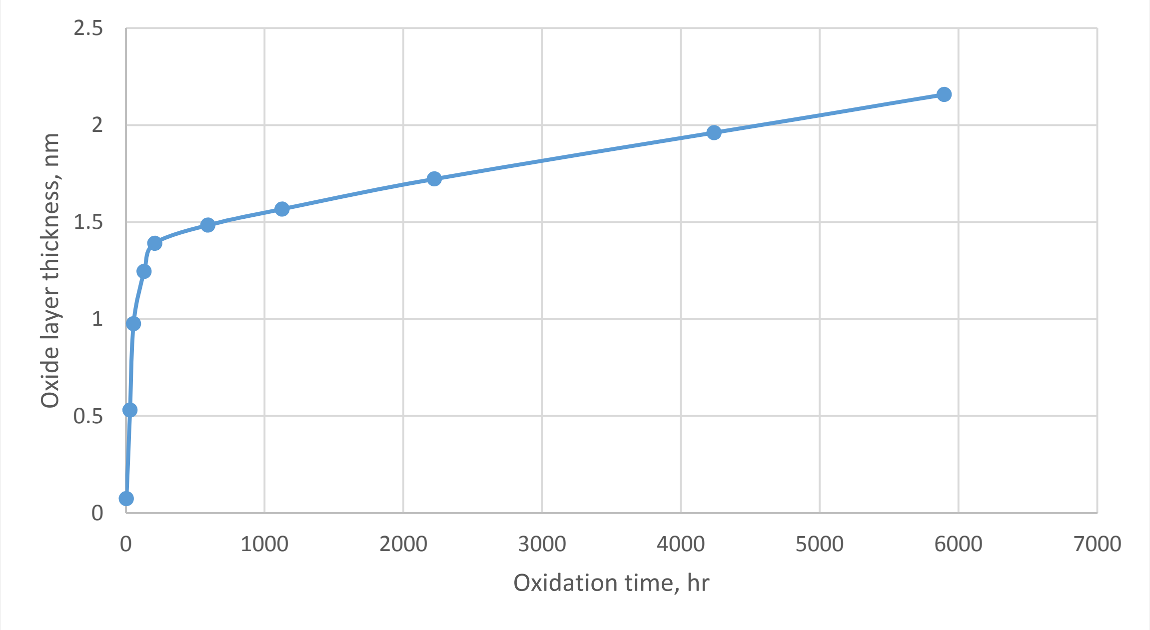

Figure 19 - Oxide contamination over a long time (6000 hr and less) for bismuth telluride, reconstructed from (Bando et al., 2000)

Performance characterization was done to study the effect of oxygen contamination in bismuth telluride under an accelerated environment. Pressed sample was placed in a hot furnace for 40 hours in an oxygen environment at 450ºC which would maximize oxygen contamination. Samples have been found to lose 17% to 55% of its Seebeck coefficient (Schultz et al., 1962). Another researcher reported that to produce samples with good electrical conductivity it is especially crucial to prevent powder from oxidation (Poudel et al., 2008).

It is important to clean the powder and remove oxides prior to any further steps in the manufacturing process. To remove oxides, either wet etching using solutions or dry oxide reduction through gases can be used. Both methods will be discussed.

3.1.1 Wet Etching

Wet Etching is the process to remove oxide contamination from a powder by exposure to a solution that would react with oxygen leaving the powder clean or oxide free. Various methods have been reported to etch bismuth telluride. Lee et al. (2000) reported using a 10% solution of nitric acid, acetone and distilled water to remove oxides from bismuth and tellurium powders. Francombe (1958) reported using a 1:1 solution of nitric acid and distilled water to etch bismuth telluride single crystal fragment prior to manufacturing.

Another reported method included using nitric acid, ethylene glycol and tartaric acid in distilled water solution with bismuth oxide and tellurium solution. The mix was initially heated up to 90ºC for 20 minutes where a vigorous evolution of nitrogen oxides takes place and evaporates leaving the solution. Heating is continued near 100ºC to reduce the solvent volume until it approaches about one-sixth of its original volume. After that remaining mixed-metal ion/polymer-like composite is heated up to about 350ºC where ignition eventually takes place (Ritter & Maruthamuthu, 1995). This last process was carried on the powder of pure elements (bismuth and tellurium) before forming bismuth telluride.

3.1.2 Dry Oxide Reduction

Another process to reduce oxide content is by gas exposure, which is called dry oxide reduction. This process usually involves exposing the powder to a gas that would react with oxygen producing another gas or vapour. The flow of gas through the porous powder would result in oxides reduction. To shorten the process and trigger oxygen to chemically react, the process is conducted at an elevated temperatures. One gas that is commonly used is hydrogen. Under elevated temperatures (ranging 200ºC to 400ºC) a stream of flowing hydrogen would react with existing oxygen producing water vapour that would be filtered from the circulating gas flow typically using chemical substances as desiccants.

One of the reported processes to remove the oxide from the mechanically alloyed powder, Hyun et al. (2001) exposed the powder to 50% Hydrogen + 50% argon mix for 24 hours at 400ºC. Oxides were reported to be removed from the powder during the process. Samples were fabricated from the powder before and after the dry oxide reduction process to compare performance. Seebeck coefficient was reported to have decreased by 5% and the overall Figure of Merit was reported to have improved by 2%. Mechanical properties of the oxide reduced samples were not reported.

Similar to Hyun et al. (2001), Ritter et al. suggested a similar method of removing the oxide where Bismuth Telluride powder were exposed to Hydrogen at 350^oC for six hours. He reported that this method was sufficient for oxide reduction of the material (Bando et al., 2000; Ritter & Maruthamuthu, 1995). Ritter (1994) reported used flowing hydrogen at 275^oC for 12 hours to remove the oxide layer. From these different sources, dry reduction of the powder using hot hydrogen gas is reported to be successful with no solid residuals.

3.2 Pressing & Sintering

Once the oxide in the bismuth telluride powder is reduced, it can be processed to fabricate the end product solid ingot. A variation of operations can happen to achieve that result, including cold pressing, cold pressing then annealing, hot pressing, spark plasma sintering (SPS) or several other methods. Researchers have studied different combinations of operations and operational conditions within the same operation, with the target of achieving a better performing thermoelectric materials. Key performance indicators of the material are figure of merit, Seebeck coefficient, thermal conductivity, electrical conductivity and mechanical properties.

The treated powder initially would have to be pressed into the shape desired. This process can happen with or without temperature elevation. With no heat addition it is called cold pressing, with heat addition it is named after the method of heating. For example an external heat source around the sample while pressing is called a hot pressing process, while an internal joule heating of the sample by a passing current while pressing is called spark plasma sintering (SPS).

3.2.1 Cold pressing

Cold pressing is the process of applying pressure on a powder that has been pre-mounted into a die with no addition of heat. Cold pressing bismuth telluride has been reported over a spectrum of pressures ranging from 5 MPa to 1200 MPa with no more than 15% difference in resultant thermoelectric properties. Kosalathip et al. (2008) reported preparing bismuth telluride samples by cold pressing them using only 5 MPa. Same process was reported by Ionescu et al. (1975) and Jaklovszky et al. (1975) using 780 MPa. Navrátil et al. (1996) reported using 1200 MPa to cold press bismuth telluride antimony alloys. Although these pressing pressures seems to vary, the resultant thermoelectric properties reported seems to be very similar with no more that 15% difference. Comparing effect of using different pressing pressures; Hyun et al. (2001) cold pressed $(Bi_{0.25}Sb_{0.75})_2Te_3$ to 425 MPa achieving a Seebeck coefficient of 145 µV/K. Hyun et al. increased the cold pressing pressure to 700 MPa achieving almost the same Seebeck coefficient. Mechanical properties were not discussed for pressed samples.

Hyun et al. (2001) tested the effect of repeating the pressing process several times. Samples were cold pressed to 700 MPa, flipped 90 degrees and repressed again up to 11 times. The maximum Seebeck coefficient achieved from cold pressing was slightly above 150 μV/K. Although it seems that the material performance did not improve from heavy deformation from higher pressure and repeated pressing, but once samples were hot pressed or annealed, performance seemed to differ between samples as discussed in upcoming sections. `

3.2.2 Heat Treatment via Furnace Annealing

Annealing is the process of heat treating the sample after cold pressing. During the process material grains forms the crystal structure without melting which is called sintering. Annealing is done by placing the sample in a furnace while in an inert environment to avoid oxidation. Annealing bismuth telluride samples is known to raise the Seebeck coefficient of a specimen that has been cold pressed. Annealing solidified ingot samples produced using the Bridgeman growth method (were not pre-pressed) at 350°C for over 48 hours does not change its properties. However, a sample that was cold pressed reported a Seebeck coefficient of 200 μV/K, 215 μV/K, 218 μV/K and 225 μV/K after 5, 10, 20 and 48 hours of annealing at 350°C as shown in Figure 20 (Hyun et al., 2001). That clearly shows increasing Seebeck coefficient with annealing.

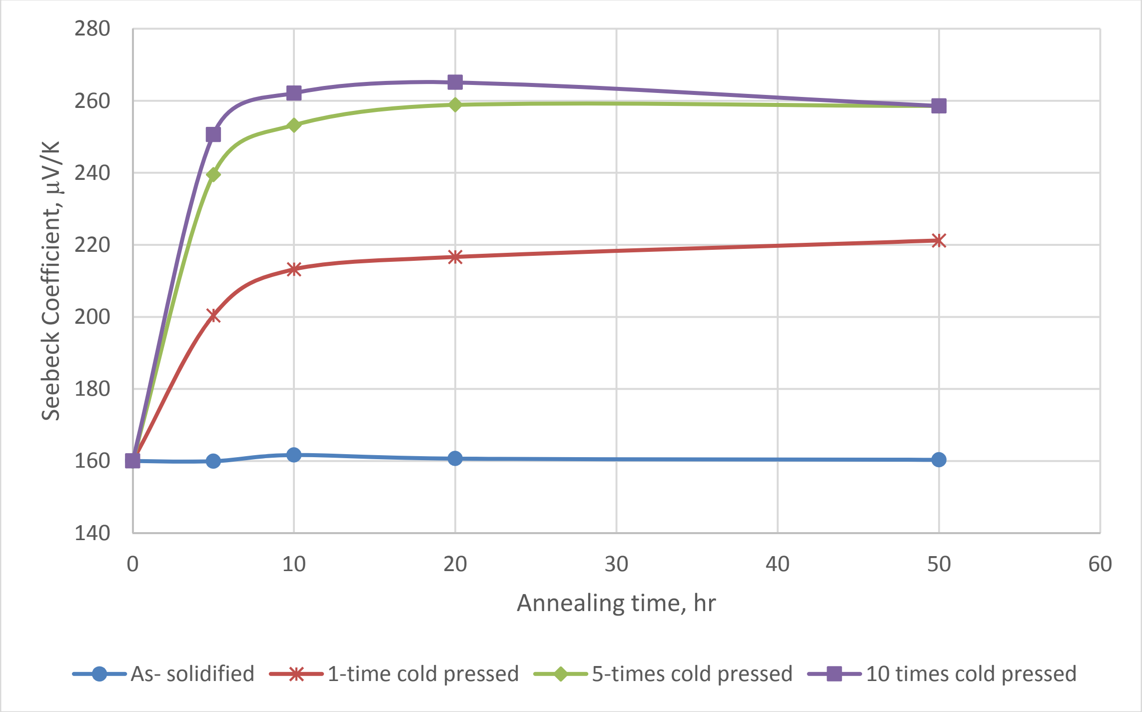

Figure 20 – Effect of Annealing on Seebeck Coefficient (Hyun et al., 2001)

Various other annealing procedures were reported for bismuth telluride. Francombe (1958) reported annealing bismuth telluride at 425°C for four to six days in evacuated sealed vitreous silica. While Jaklovszky et al. reported sintering at 400°C for 20 hours, Ionescu et al. (1975), Jaklovszky et al. (1975) and Navrátil et al. (1996) reported annealing at 530°C for 1 hour. To conclude, researchers have used different sintering temperatures varying from 350°C to 550°C and holding times from 30 minutes to as long as 200 hours. Different sintering temperatures and hold times will be tested as part of this research project.

Hyun et al. (2001) tested the effect of annealing after pre-pressing the sample several times. Samples were cold pressed to 700 MPa, flipped 90 degrees and repressed again up to 11 times. Figure 20 shows Seebeck coefficient increasing with the number of cold presses.

3.2.3 Hot Pressing

Hot pressing is the process of heating samples to a controlled temperature while applying pressure in an inert or vacuum environment. This process has been known to lower the temperature and time needed for the sample to sinter. Hyun et al. (2001) tested different hot pressing temperatures on $(Bi_{0.25}Sb_{0.75})_2Te_3$ samples that were pre-cold pressed with a pressure of 425 MPa. Hot pressing temperatures ranging from 350°C to 550°C were tested. Seebeck coefficient was found to increase with pressing temperature until a temperature between 350°C to 500°C depending on the grain size. Figure of Merit was found to always increase with hot pressing temperature with the highest value achieved from hot pressing at 550°C for 30 min. Figure of Merit combines different thermoelectric properties and is considered a better indicator of material thermoelectric performance.

Similarly, Yang et al. (2006) reported testing various temperatures for hot pressing Bismuth Telluride and reported that Seebeck coefficient achieves a maximum value of 175 μV/K using a temperature of 400°C. Increasing temperature further decreased Seebeck coefficient but increased Figure of Merit until 460°C where it reaches its maximum Figure of Merit value.

Hyun et al. (2001) reported achieving a Seebeck coefficient of 195 μV/K for samples that were cold pressed with 425 MPa then hot pressed at 500°C for 30 min. To study the effect of heavy mechanical deformation, samples were hot pressed after a number of cold presses. Samples were flipped 90 degrees between each cold press. Figure 21 shows experimental results comparing Seebeck coefficient of the sample after hot pressing against the number of pre-cold presses. A general trend can be observed of increasing Seebeck coefficient with number of cold presses. Samples that were cold pressed 11 times reach a Seebeck coefficient of almost 250 μV/K.

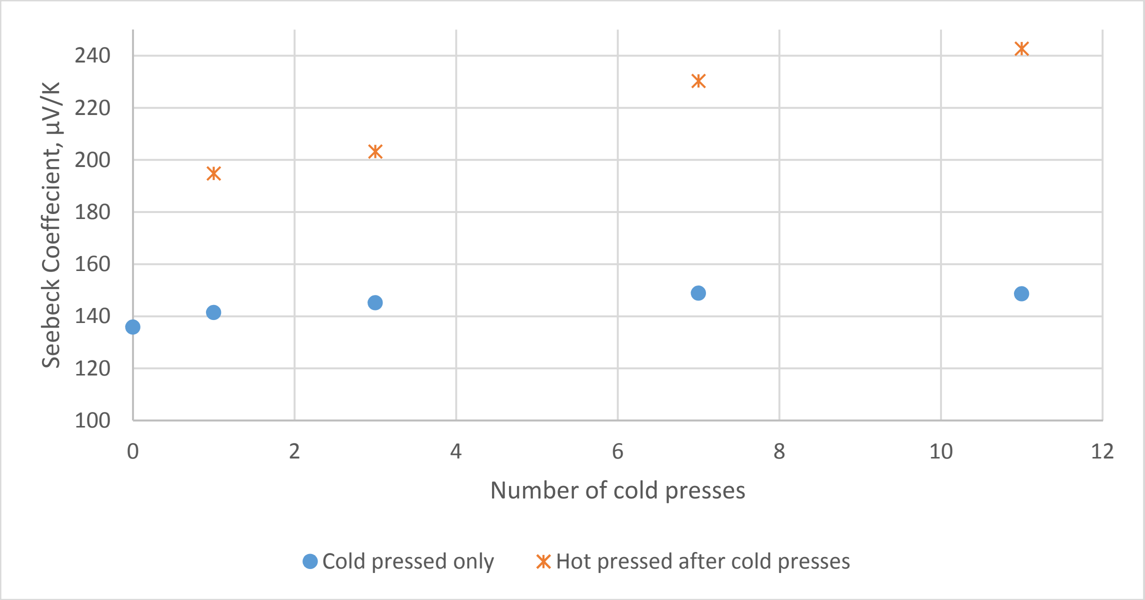

Figure 21 – Comparing the effect of repressing samples, reconstructed from (Hyun et al., 2001)

In conclusion, in cases that samples were only cold pressed once then hot pressed compared to cold pressed then heat treated, hot pressing is reported to improve the thermoelectric properties of prototypes while lowering the needed process time to a great extent (30 min opposed to 2 weeks in some cases). Other benefits includes reducing the needed pressure and temperature for sintering. However, when applying a high mechanical deformation on the sample by pre-cold pressing several time, cold pressing then heat treatment resulted into a prototype with a higher Seebeck coefficient. This process took approximately five days compared to less than an hour using hot pressing method.

3.2.4 Spark Plasma Sintering (SPS)

Spark Plasma sintering is the most recent method of producing thermoelectric materials. The SPS process is the application of intense electric current pulses through the specimen while under pressing pressure in an inert environment. SPS uses joule heating due to passing current to heat the material uniformly. In traditional heating through conduction, convection or radiation, heating starts from the outer surface and propagates inside.

SPS was used to produce a bismuth telluride specimen with a chemical composition of $Bi_2(Se_{0.07}Te_{0.93})_3$ For N-type and $(Bi_{0.2}Sb_{0.8})_2Te_3$ For P-type. Applied pressure of 35 MPa was used, temperature of 400°C for N-type and 375°C for P-type were measured (Böttner et al., 2007). Compared to cold and hot pressing – pressing pressure, sintering temperature and process time are less while achieving better or similar results. Cold pressing and sintering is less initial capital demanding and can be adapted for high volume manufacturing.

Chapter Four: Design and Manufacturing

4. TEG module Design and Manufacturing

Building on the initial novel step by Min & Rowe (2007), the goal of this research is to study, fabricate and test an annular thermoelectric generator module. Min & Rowe experimental results did not achieve targeted performance developed by their analytical model for various reasons and challenges. To overcome some of these challenges, a modified annular TEG module will be discussed starting from initial design and motive behind it to manufacturing procedure as well as module assembly forming the experimental test prototype.

4.1 Module design and geometry

Min & Rowe experimental results did not meet the forecasted performance by their analytical model. Several reasons were provided explaining experimental results which will be addressed later in this chapter. One concern is that there is a heat path flow between the conductor rings inner edges in Min & Rowe's design. Meaning that heat is only flowing through a portion of the material, therefore lowering assembled module performance. A novel design for the p-type ring geometry has been proposed to improve heat path inside the ring which would utilize more of the material of the ring-structured ring into power production, making the geometry more efficient than the ring-structured module produced by Min et al.

Figure 22 shows the proposed geometry for p-type rings. The side edge surface area in contact with the conductor ring has been minimized to lower heat flow to the conductor ring before going through the rest of the ring. P-type rings were manufactured with the mentioned v-shaped ring while n-type rings were kept in a ring-structured shape. Rings were manufactured with an inner diameter of 7.93 mm, an outer diameter of 12.7 mm and thickness averaged around 3.25 mm. N-type and p-type thermoelectric materials have different densities. For these dimensions, our industrial partner recommended using 1.4 grams for p-type and 1.9 grams for the n-type. These mass values were not changed throughout the project for comparison between prototypes. Different values are being investigated in the next phase of the project.

An assembly of 2 p-type V-shaped rings and 2 n-type ring-structured modules was manufactured, tested and compared against an assembly of two ring-structured thermoelectric couples. Test results will be displayed and discussed in the results and discussion chapter.

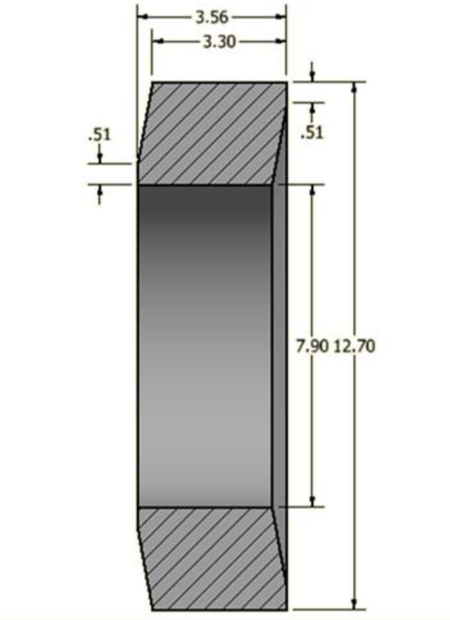

Figure 22 – Proposed V-shaped p-type ring (dimensions in mm)

4.2 Manufacturing Annular TEG Prototypes

Prototypes were manufactured using power metallurgy starting with a mechanically alloyed bismuth telluride powder with the chemical composition ($(Bi_{0.2}Sb_{0.8})_2 Te_3$) for p-type and ($(Bi_{0.95}Sb_{0.05})_2 (Te_{0.95}Se_{0.05})_3$) for n-type. Prototype fabrication process can be summarised in three steps, powder preparation, cold pressing and sintering.

4.2.1 Oxide Reduction Process

First step is to prepare the mechanically alloyed powder for pressing. Stored powder gets contaminated with oxides over time. Therefore prior to any manufacturing process, the powder must be cured from oxide contamination and restored to original composition.

4.2.1.1 Detecting Oxides

The process of oxidation of Bi_2Te_3 was investigated with X-ray photoelectron spectroscopy (XPS). Bando et al. (2000) noticed that over the first 100 hours it was found to be a rapid process where bismuth telluride grains developed an oxide layer 1.25nm thick. Then it was found to be a steady linear relation after that where the oxide layer thickness grew almost 0.5nm every 1000 hours.

Early manufacturing trials, dimension growth during sintering process was observed. Suspecting the powder to be contaminated with oxides, X-ray diffraction on two powders was performed. Powder A, stored in air, suspected to be contaminated with oxides and powder B, stored in Argon, expected to be oxide free. P & N-type samples were tested for each of powder A & B. Results in Figure 23 to Figure 26 show that oxygen has been detected in one sample of the four. Oxide was detected in the P-type powder A sample in the form of Sb_2O_3.

It was expected to detect tellurium oxides and bismuth oxides in the form of Bi_2O_3 and TeO_3 in powder A, but XRD did not detect them. XRD resolution for the facility used is around 40 nm but bismuth and tellurium oxide layer thickness can be as small as 1.5 nm around powder grains (Bando et al., 2000). This test was determined inconclusive to quantify existence of oxides in bismuth telluride unless a higher resolution was used.

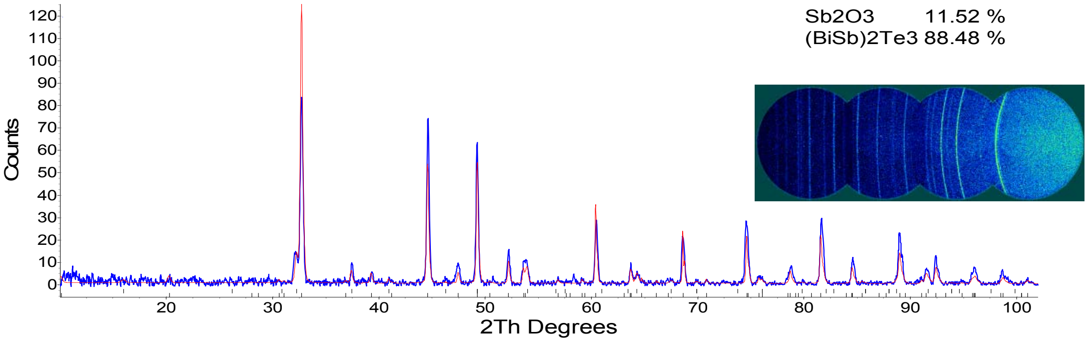

Figure 23 - XRD results for P-type ring made from Powder A

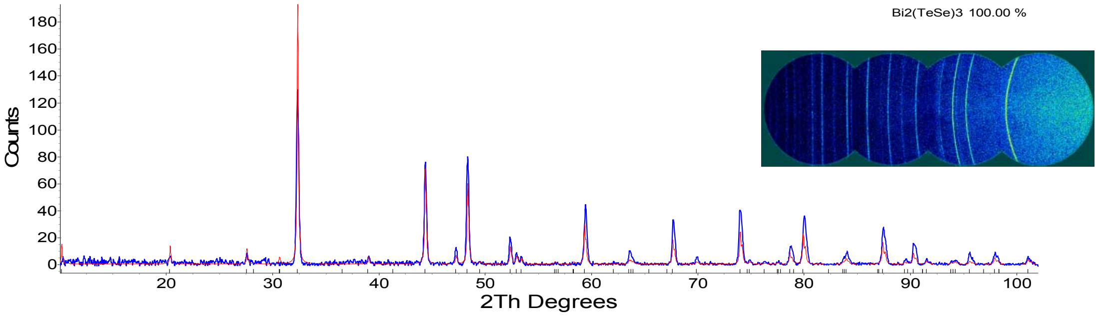

Figure 24- XRD results for N-type ring made from Powder A

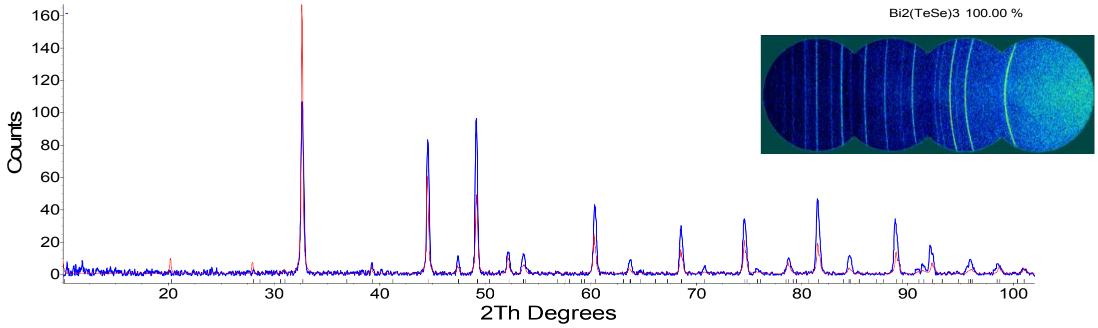

Figure 25 - XRD results for P-type ring made from Powder B

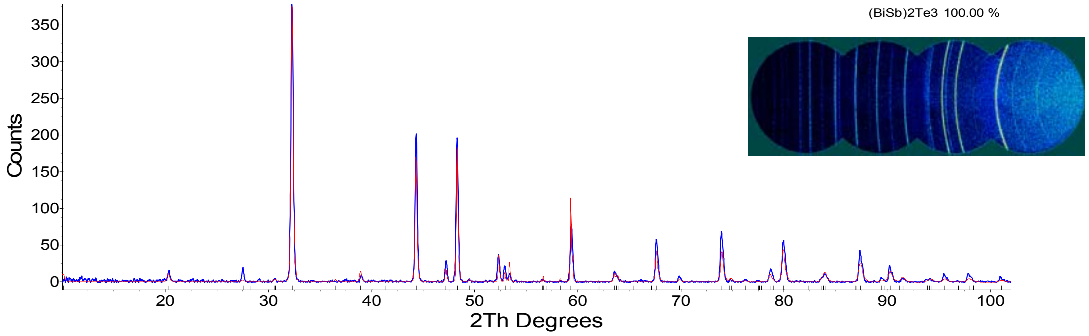

Figure 26 - XRD results for N-type ring made from Powder B

As XRD was suspected not to be enough indication of oxide contamination, a different test was performed on samples made from a powder suspected to be oxide contaminated and a powder that had undergone a dry oxide reduction process (will be discussed later in this section). Samples were pressed from both powders, then heated up to 430ºC under XRD to compare behaviour during elevation of temperature. Samples from the oxidised powder has been found to grow in size excessively during sintering process. Results shown in Figure 27 and Figure 28 and summarized in Figure 29, clearly indicates that oxide reduction process has impacted material behaviour, meaning that the powder was contaminated with oxides. Samples that was manufactured from oxide contaminated powder experienced more expansion during temperature elevation and suffered from five times more permanent size growth after the sample was cooled to room temperature.

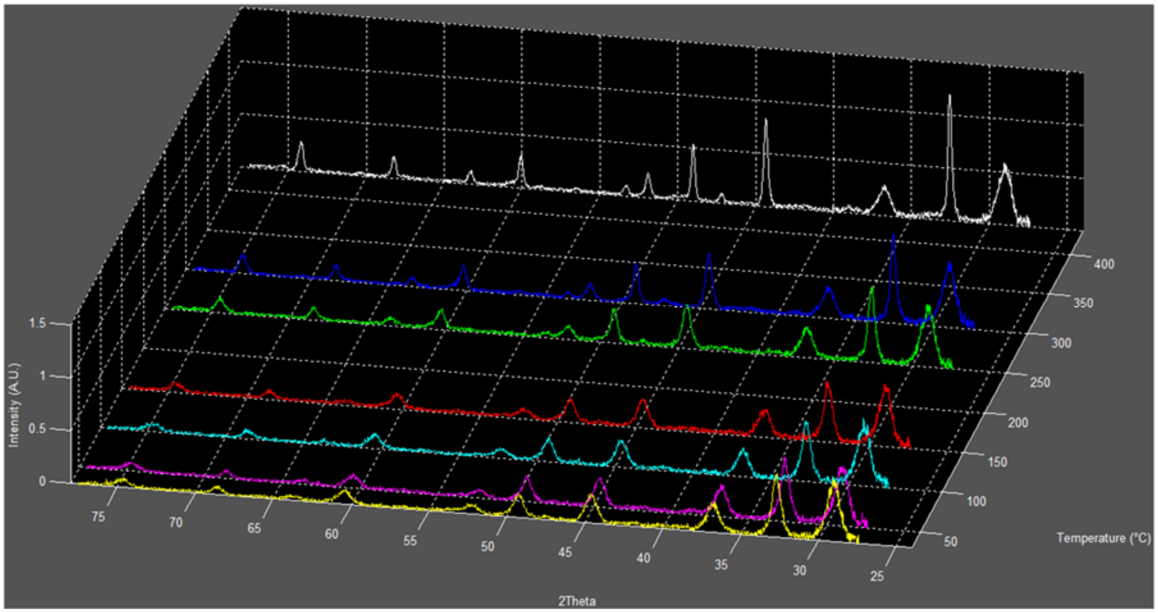

Figure 27 – Oxidized sample pattern vs temperature (Cino, 2015)

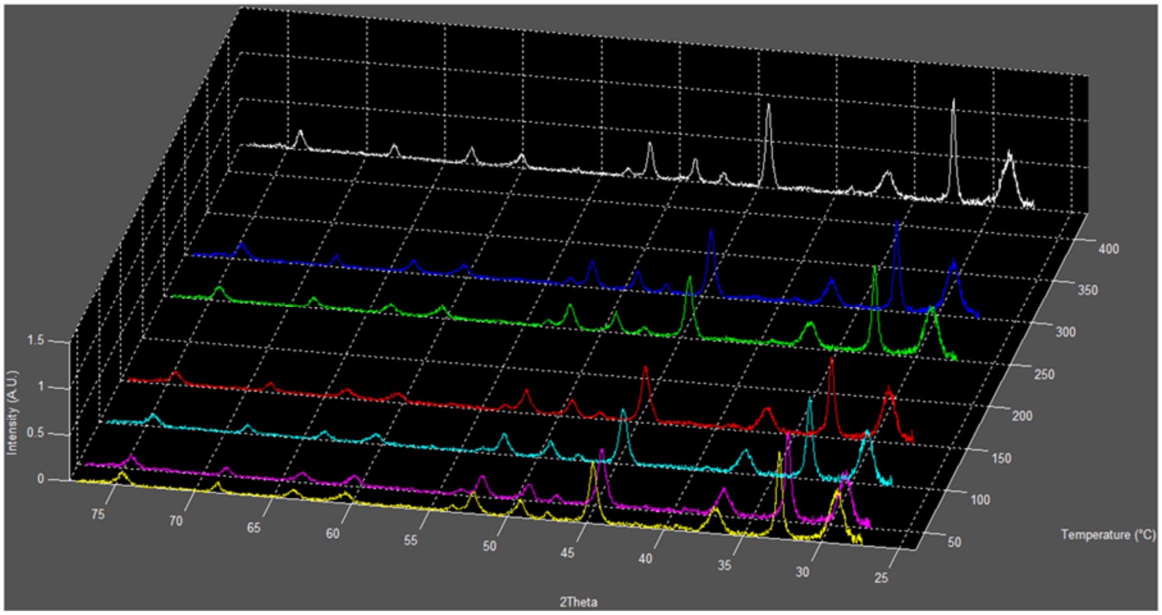

Figure 28 – Reduced sample pattern vs temperature (Cino, 2015)

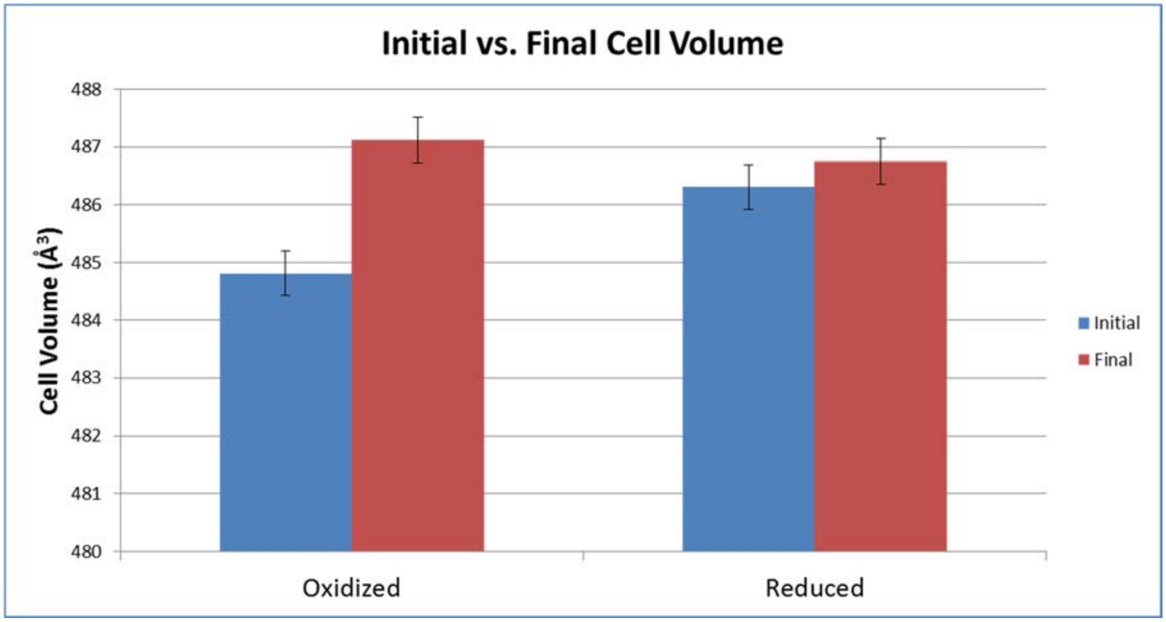

Figure 29 – Comparing initial and final cell size for oxidized and reduced samples test under XRD (Cino, 2015)

4.2.1.2 Reducing Oxides in Bismuth Telluride

To remove oxides, either wet etching using solutions or dry oxide reduction through flowing gases can be used. Wet etching has been tried, a 3:1 Nitric acid to deionized water was used to clean the bismuth telluride powder. The mix was places in a strainer and then cleaned using acetone. Few challenges was found in the process. Etching time was a variant that could be determined and residual powder appeared to be wet. The process could not take place in an inert environment glove box due to resultant NOx fumes produced during the process. For mentioned reasons, wet etching was not used and a dry oxygen reduction method was adopted.

Bismuth telluride powder was exposed for flowing stream of hydrogen while in a tube heater with temperature elevated to 350^{o}C for six hours. Once the oxide reduction process was completed, the powder was sealed in a glove box that has a preserved argon inert environment. Raising the temperature more than that during the oxygen reduction process caused the powder to start sintering which would lower its porosity, therefore lower gas penetration during the process.

Extra measures were taken afterwards to ensure the powder would not be exposed to oxygen during the manufacturing process. The powder was pre-pressed inside a glove box, then moved outside the glove box while still inside the die to be pressed on a more powerful press to the target pressure. After pressing the sample it was moved back to the glove box where it was put in a Pyrex vial.

Capped Pyrex vials filled with argon from the glove box are then moved to where they are vacuumed, filled with argon and sealed.

Samples in the early phase of the project did not go through an oxide reduction process prior to manufacturing. Effect of oxygen contamination was tested, compared with oxide reduced samples and will be discussed in the results and discussion chapter.

4.2.2 Cold pressing process

Once the oxide in the bismuth telluride is reduced, it can be processed to produce the end product geometry. This process can happen with or without temperature elevation. With no heat addition it is called cold pressing, with heat addition it is named after the method of heating. For example an external heat source around the sample while pressing is called a hot pressing process, while an internal joule heating of the sample by a passing current while pressing is called spark plasma sintering (SPS).The focus of this research project was only cold pressing with no concurrent heat addition.

Cold pressing is the process of applying pressure on a powder that has been pre-mounted into a die with no addition of heat. The die contained an inner shaft to produce the desired ring shaped sample. Used pressures reported in literature ranged from 5 MPa (Kosalathip et al., 2008) to 1470 MPa (Arreguin-Zavala, Vasilevskiy, Turenne, & Masut, 2013). Most common pressures used for bismuth telluride falls into the 400MPa range.

Powder used to produce samples has been found to limit the used pressure during pressing. Same powder composition from two different sources (different suppliers) has been used over the course of the project, one of them allowed for pressure up to 230 MPa, but always cracked if a higher pressure was used. Powder from a second supplier allowed only for pressure up to 130 MPa before it would produce cracked samples. Example of cracked samples is shown in Figure 30. The difference in allowed pressure between powder samples is due to remaining oxides in the material, difference in grain sizes or the pressing die tolerances. Trials to exceed the mentioned pressure and reach the targeted pressure of 400 MPa were not successful. Thus at this stage in the process development, powder samples A & B were tested at their maximum pressures respectively. Further refinement of cold press pressure optimization is planned once a fabrication process is established.

Figure 30 – Cracked sample during pressing process

4.2.3 Sintering Process

Annealing is the process of heat treating the sample after cold pressing to improve thermoelectric and mechanical properties. Sintering is when material grains forms the crystal structure without melting. The process is done by placing the sample in an elevated temperature furnace while in an inert environment to avoid oxidation. One of the most crucial steps of manufacturing thermoelectric generators is sintering the sample once it is pressed.

After pressing samples, they were arranged inside a slightly wider Pyrex tube with plastic ring spacer in between. Tubes were vacuumed, filled with inert gas and then sealed. Sealed vials were put into a programmable Klin (furnace) that controls rate of ramping up and down temperatures, hold temperature and hold time. These factors are not the only factors affecting sample processing. Furnace model, age, and internal dimension, sample location inside the furnace, sample orientation, existence of a radiation shield around the sample and location of furnace (draft hood, ventilation, etc…) are all factors that were found to affect the rate of heat transfer, sample temperature and the end product. For consistency sealed samples always should be sintered using the same exact furnace, samples to be put in the same location and using the same radiation shield.

Figure 31 - Effect of location and orientation inside the furnace, left: deep inside the furnace, middle: in a horizontal orientation, right: outer half of the furnace – near door

Figure 31 shows three samples that were sintered using same furnace and temperature but only changing location and orientation inside the furnace. The sample on the far right was sintered in the outer half of the furnace while the sample on the far left was sintered deep inside the oven, both in a vertical orientation. The sample sintered deep inside the oven shows exposure to higher temperatures. A third sample (Figure 31 – middle) was sintered in a horizontal orientation where it grew downwards into the direction of gravity creating a non-uniform shape. Therefore all sample throughout this research project were always kept in a vertical preference during sintering process.

Samples were produced with different sintering temperatures and hold times and were tested to compare performance of each parameter. Results for different tests are displayed in the result and discussion section. Temperature elevation and cool down rates were always set to less than 50 degrees per hour to avoid quenching.

Few papers recommended sintering bismuth telluride at 500ºC and 550ºC for one hour (George et al. 1959; Ionescu et al., 1975; Schultz et al., 1962). Following their lead and after few tries, it was found that sintering at any temperature higher that 430ºC causes samples to grow in size (Figure 32 & Figure 33). Such growth make it out of shape and unfit for testing, as well as expected severe deterioration in properties as for the deterioration of density. Since grown samples were pressing against the Pyrex inner perimeter, it was more challenging to extract samples from the containing vials. It was observed that growth in oxide contaminated samples is excessive compared to a sample manufactured from a powder that has undergone an oxide reduction, which is the same result the XRD with elevated temperatures test has quantified (discussed earlier in this chapter).

Figure 32- Samples sintered at 500°C – extensive growth

Figure 33 - Samples sintered at 550°C – extensive growth

4.3 Assembly of prototype in test section

Prototypes were fabricated using powder metallurgy starting with a mechanically alloyed bismuth telluride powder with the chemical composition ($(Bi_{0.2}Sb_{0.8})_2 Te_3$) for P-Type and ($(Bi_{0.95}Sb_{0.05})_2 (Te_{0.95}Se_{0.05})_3$) for N-Type. Each module prototype had 2 couples of TEG rings. In each experimental test total of 2 P-type and 2-N-type rings were mechanically assembled alternately on a chilled water tube. In between the thermoelectric rings, aluminum rings were inserted as a conductor forming hot and cold Junctions.

Figure 34 and Figure 35 show the test section assembly. Rings were manufactured with an inner diameter of $7.93mm^{+0.12}$, outer diameter of $12.7mm^{\pm 0.03}$ and an average thickness of $3.25mm^{\pm 0.03}$. Each n & p types rings is 1.9 grams and 1.4 grams respectively. Test performed using a ring-structured module similar to the one (Min & Rowe, 2007) manufactured for comparison and the proposed V-shaped design.

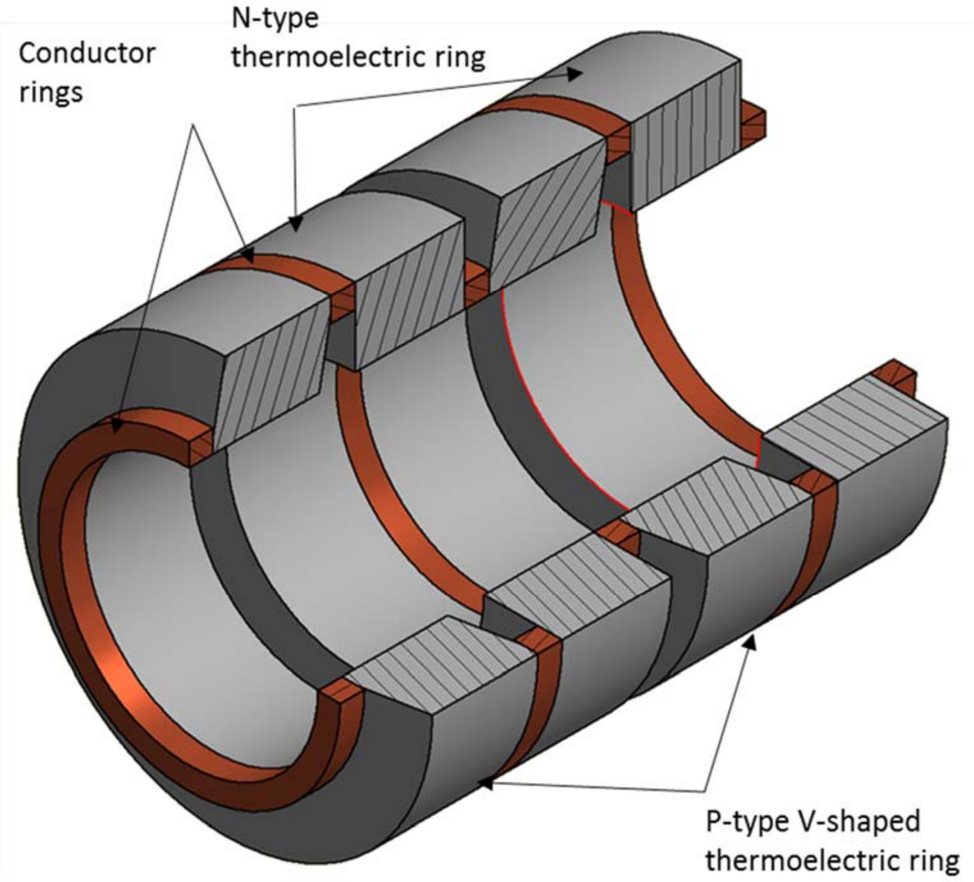

Figure 34 – TEG test section assembly using V-shaped P-type Rings

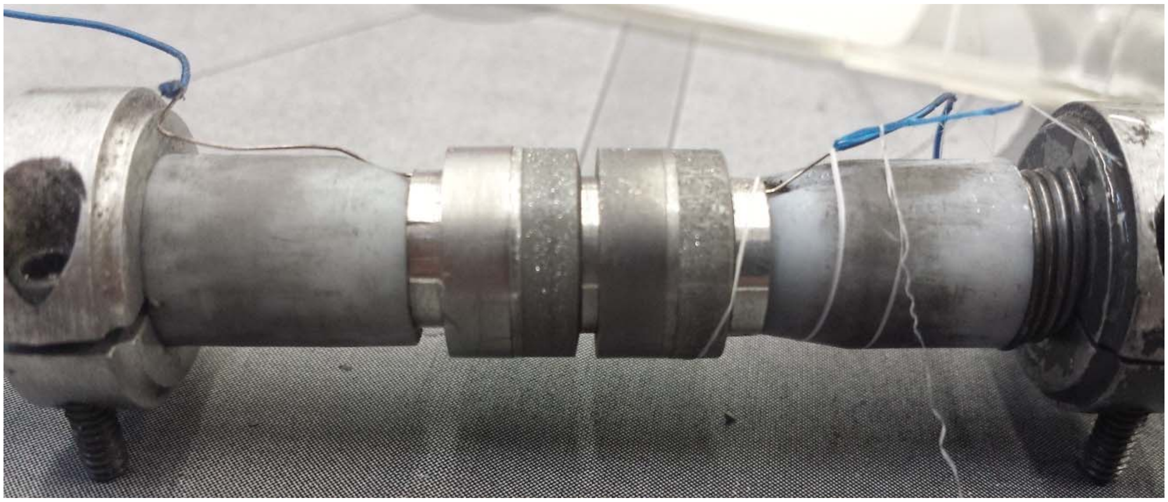

Figure 35 – TEG test section assembly showing TEG Rings, Aluminum Rings and the spring used to exert constant axial clamping force

To assemble this TEG module on the chilled water pipe, first an electric insulation layer needs to be applied on the surface of the pipe. A layer of aluminum nitrite paste is used as electric insulation. After applying the electric insulative layer, p-type and n-type rings are installed. The inner diameter of the ring has to be in a clearance fit with the pipe surface not to scratch the electric insulation layer. Clearance fit creates an air gap between the ring and the pipe increasing the contact resistance on the cold side of the TEG module. In between thermoelectric rings, conductor rings are installed to connect the inner and outer surface alternately as shown in Figure 34. Additional conductor rings are fitted on both ends of the module with a wire mechanically attached to the ring for voltage measurement. To attach the half millimetre wire to the aluminum ring, a hole was drilled through the ring in the axial direction, the wire was inserted, and then using a mechanical punch the hole was pressed holding the wire inside.

The prototype test section assembly were mechanically held together using a spring, electric current measurements were excluded from results as the test section is only mechanically assembled not bonded which led to a significant electric contact resistance.

Chapter five: Experimental Test Facility

5. Experimental Test Facility

A novel experimental test facility was developed to characterize thermal and electrical performance of annular thermoelectric generator (TEG) modules for different thermal and electric loads. Measurement of output electric power, voltage, current, and thermal conductance can be made simultaneously as a function of load resistance and surface temperatures.

The purpose of the facility is to simulate a range of controllable conditions and precise accurate measurement of different affecting and resultant parameters. A typical application for a power generating thermoelectric module would have a hot side or heat source and a cold side or a heat sink. Both heat flowing from the heat source and to the heat sink needs to be controlled and measured to simulate targeted conditions. The heat flowing through the thermoelectric material will cause the TEG module to produce electricity. This electricity produced is measured under different electric conditions to fully characterize its performance under a certain thermal condition. In Figure 36, a schematic diagram of the annular TEG module tester shows the cold side of the test facility controlled by a chiller, the hot side controlled by a DC electric heater and the electric performance of the TEG module characterized using a DC electronic load.

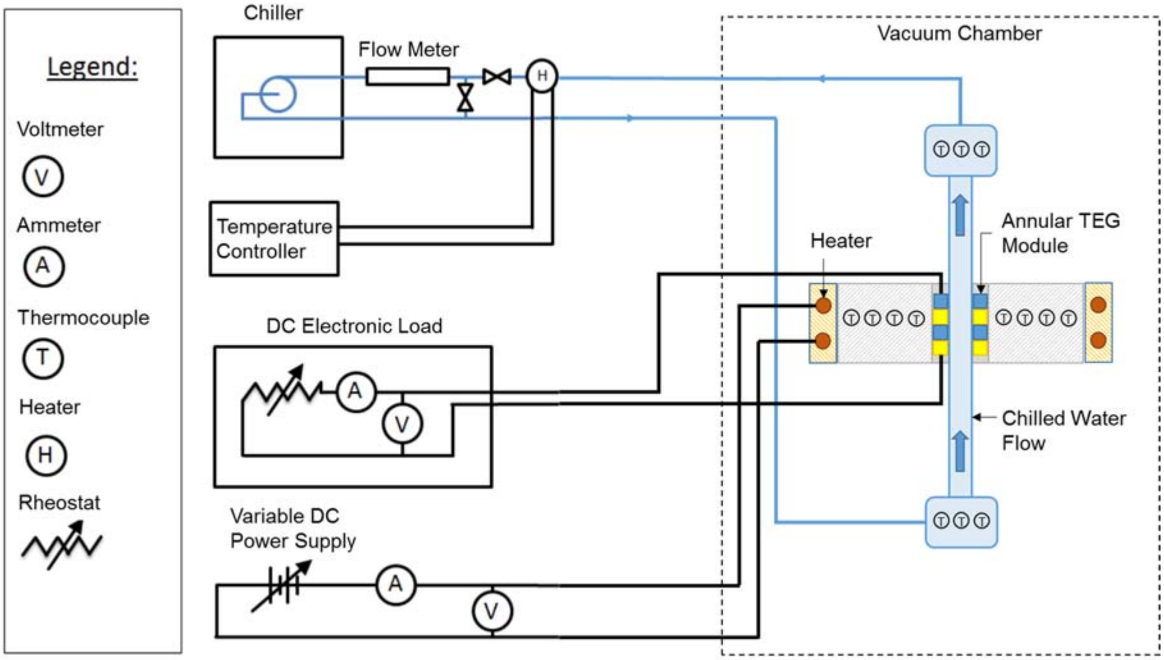

Figure 36 – Schematic diagram of the annular TEG module tester

Figure 37 shows how energy flows to and from the test section. Input to the test section is the thermal energy conducted on the hot side of the TEG module. A portion of the heat flowing through the thermoelectric material is used to produce electrical energy and the remainder of the thermal energy goes through the module to the chilled water stream. This facility provides a mean to measure the energy balance of the system between measured input and output energy to and from the TEG module.

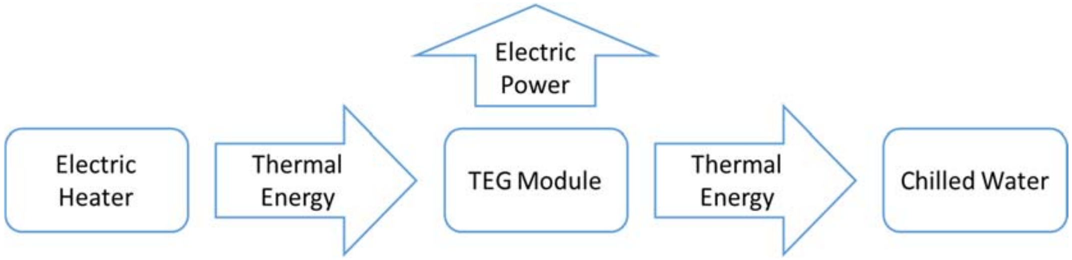

Figure 37 – Energy balance of the annular TEG module tester

5.1 Hot Side

The hot side of the experiment facility was designed to control the amount of heat flowing into the test section and therefore controlling the hot surface temperature. The heat source of the hot side consist of two electric heaters powered by an HP 6655 DC power supply. The inside of the electric heater is electrically insulated. Figure 38 shows the heat flux on the outer circumference of the cylindrical hot block. Different components of the cylindrical hot block is shown in Figure 40. The first layer on the inner side of the electric heater is a copper cylinder to help create a constant heat flux boundary condition around the test section. On the inner surface of the copper block is a stationary stainless steel cylinder tapered on the inside. Three inversely tapered stainless steel blocks forming a cylindrical shape slides on the inner stationary tapered block forming three jaws. The outside of the blocks are inversely tapered and slide vertically to apply contact forces on the TEG assembly. As jaws slide downwards under its weight, it applies contact forces on the outside of the annular TEG assembly minimizing contact resistance between the assembly and heat source.

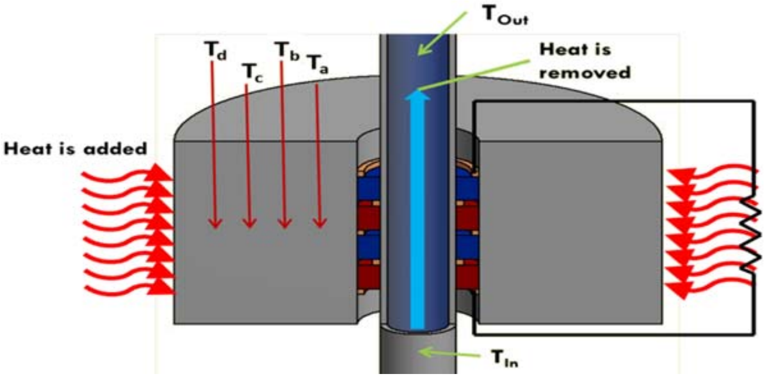

Figure 38-Section showing the annular TEG assembly, Heat added through an electric heater and heat removed by an inside water stream.

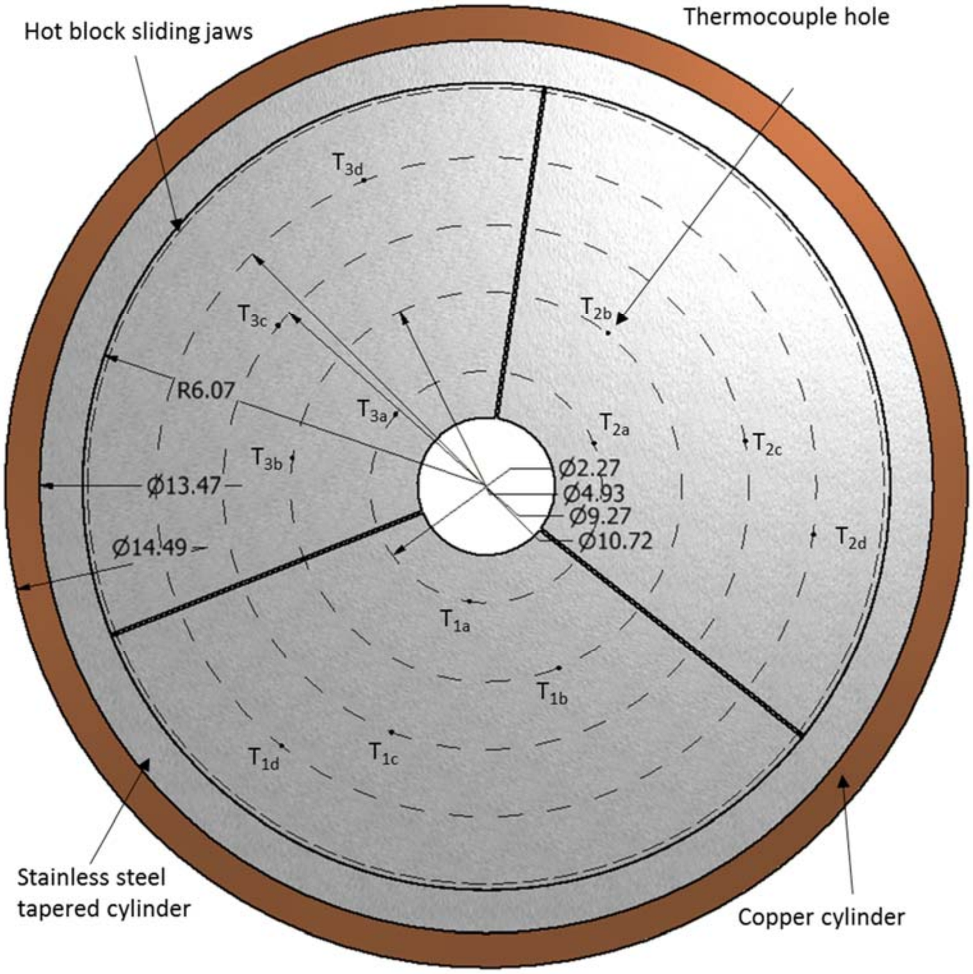

Figure 39 - Hot side stainless steel blocks with thermocouple locations, dimensions in cm - elevation

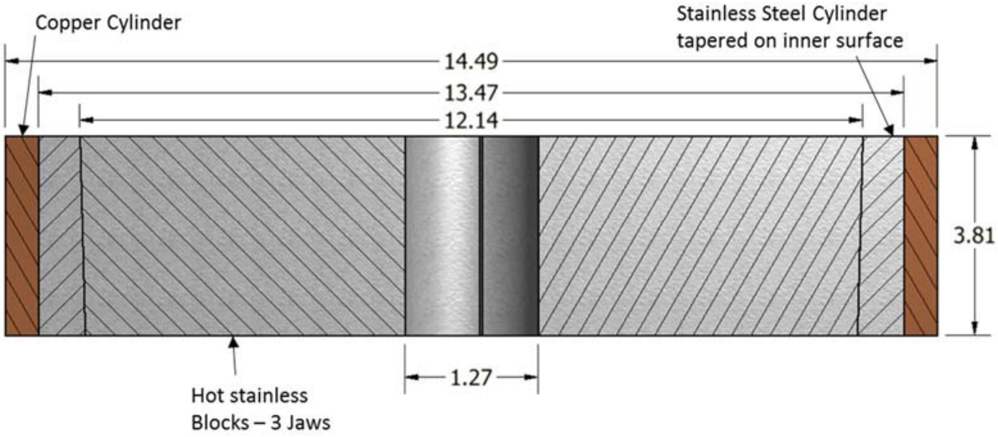

Figure 40 – Hot side stainless steel blocks with thermocouple locations, dimensions in cm - section

The three stainless steel blocks have twelve Type T thermocouples spread over different positions in the radial and angular directions as shown in Figure 39. From the reading of the twelve thermocouples, the hot surface temperature of outer surface of the TEG module can be extrapolated and the heat flow through the hot block can be calculated. The amount of heat added by the heater can be controlled by controlling the voltage and current input. When steady state is achieved, the heat flowing through the three jaws is assumed to be flowing radially through the test section to the chilled water stream. A leakage passage has been observed through the heater assembly holding blocks, Figure 41. Therefore energy input to the test section is the conduction heat flow through the hot block calculated from the thermocouples readings not the electrical power input to the heater.

The stainless steel hot block jaws have a thermal conductivity of 16.2 $Wm^{-1}K^{-1}$, height (t) of 38.2mm, outer diameter of 121.4mm and an inner diameter of 12mm to 13.5mm which would match the outer diameter of the tested TEG module under its weight sliding on the outer taper. The hot block is divided in three jaws. Each jaw has four thermocouple on a defined radius but spread along the circumferences (i.e. not in one line). The first three thermocouples (one in each jaw) are on a radius of 1.137 cm, second, third and fourth set of thermocouples (three each) are on a radius of 2.467 cm, 4.636 cm and 5.359 cm respectively.

The capacity of the heater is limited by the power supply used to a maximum of 260 W. For experiments performed throughout this project, maximum power used on a steady state condition was approximately 110 W. The limitation was the maximum temperature achievable by the test facility not to overheat parts manufactured from Teflon for thermal insulation. Teflon melt point is 327^{o}C and the maximum temperature achieved on the hot block was 240^{o}C.

The outer surface of the TEG module was wrapped with Teflon tape to electrically insulate the block and the TEG test section module. Electrical insulation was verified by current measurement after test section assembly and prior to the experiment to confirm no electric short circuit exists between the TEG module and the hot block.

5.2 Cold Side

The cold side of the thermoelectric generator is a stream of chilled water supplied by a Lytron RC011G03BB2M001 chiller. The assembly of annular TEG rings is fitted on the chilled water pipe. Water flow can be operated at a mass flow rate between 0.2 Kg/min and 4 Kg/min provided by the chiller. The inlet and outlet temperatures are measured through 6 thermocouples, a set of three thermocouples for the water inlet and another set of three for the outlet. Thermocouples are embedded in a pre and post mixing chambers before and after the test section. Each thermocouple set readings are averaged to represent the temperature of the water. Figure 41 shows chilled water path into and from the test section as well as both the premixing and post mixing chambers.

Initially the test section chilled water pipe was a stainless steel tube. To lower thermal stresses exerted on the TEG module from thermal expansion of the pipe, it was switched to an Invar tube. The change reduced thermal expansion coefficient of the chilled water pipe from $16x10^{-6}$ m/(m.K) to $1.2x10^{-6}$ m/(m.K), which reduced thermal expansion of the pipe by 92.5%. Invar is a steel-nickel alloy that is 36% nickel and 73% steel. Invar has almost the same thermal conductivity as stainless steel, therefore would not increase the pipe conductance heat resistance.

The water path is designed to flow upwards to free the system from any air bubbles. Operating temperatures for the chiller range between 9^{o}C to 22^{o}C. In cases where different range of temperatures is needed, an inline heater can be added to the water path to raise the water temperature to the desired value. Changing the flow inside the test section can be controlled using a bypass valve which affects the heat transfer coefficient inside the pipe. Achievable heat transfer coefficient values for the test facility ranges from 400 W/(m^2K) to 12,000 W/(m^2K). A layer of aluminium nitrite is applied on the outer surface of the pipe to electrically insulate it between the TEG module and the pipe.

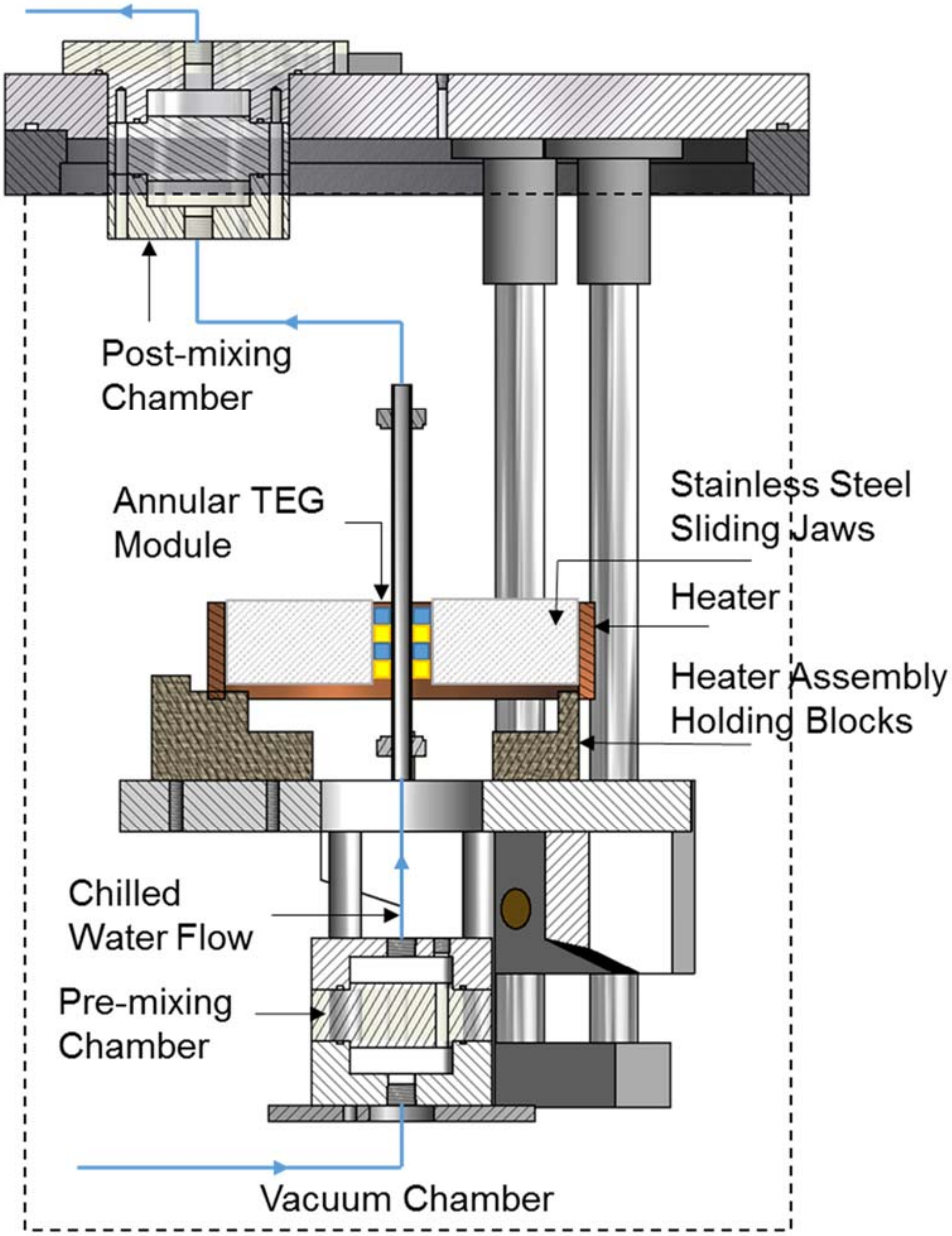

Figure 41 - Water passage inside the facility including the pre-chamber, post chamber and TEG assembly

To install TEG rings on the chilled water pipe, rings had to be made into a clearance fit to slide without scratching the applied insulation layer. An air gap of 0.02 mm to 0.07 mm between the rings and the pipe would typically exist to allow the assembly process. When the test facility is under vacuum, the resistance of this air gap grows creating a significant temperature difference between the pipe surface and the TEG module cold surface. An extra thermocouple was initially mounted on the pipe surface to measure the cold surface temperature of the TEG assembly. Temperature measured by the thermocouple was found not to represent the TEG module cold surface temperature but rather the pipe surface temperature or in between both. A thermal conductive paste was not applied as it was found to leak between the rings assembly creating an electrically insulative layer in between assembly components and a thermal bridge over the surface of the ring. The TEG cold side temperature was estimated through a different method which will be discussed in a later part of this chapter.

Having measurements of the water flow rate as well as the temperature before and after the annular TEGs test section, the amount of heat absorbed by the water can be calculated representing one leg of the energy balance equation. Each of the inlet and outlet temperatures is an average of three thermocouples to improve accuracy. The average of both inlet and out temperatures is named as $T_{\text{water average}}$.

5.3 Electrical Performance

The electrical output of the annular TEG assembly is measured through wires connected to the end aluminum rings of the test section. After obtaining steady state, open circuit voltage and short circuit current are measured. Then using a variable resistor model, voltage and current are obtained over different resistance values to characterize the electrical behavior of the annular TEG assembly. Voltage and current measurement were obtained using an Agilent U1253B Multimeter.

At current stage of the project, and since TEG modules are only mechanically assembly not chemically bonded, current measurement are not taken due to the significant electrical contact resistance between the rings P&N junction modules. Once the TEG module is chemically bonded in the next phase of the project, electric current can be measured and compared between different prototypes as an indicator for the TEG module performance.

5.4 Vacuum Chamber

The entire Test facility is placed into a vacuum chamber to minimize convection heat losses. The test facility is designed in a way to put insulative materials with a very low thermal conductivity (less than 0.08 W m^{-1} K^{-1}) segregating between hot and cold sides of the test facility. Only radiation losses are to be accounted for, which within the range of operation of the test facility (a maximum of 250^{o}C) is low compared to the heat flowing in the system.

5.5 Data Reduction

Data captured during the experiment is analyzed to characterize the thermoelectric generator module thermal performance and effective Seebeck coefficient. Parameters gathered are summarized in the following table

Parameter Symbol	Description	Device used to capture Data
T_{1a}	Hot block 1, 1st thermocouple from the TEG test section	OMEGA Type T thermocouple. 0.021 in Dia
T_{1b}	Hot block 1, 2nd thermocouple from the TEG test section	
T_{1c}	Hot block 1, 3rd thermocouple from the TEG test section	
T_{1d}	Hot block 1, 4th thermocouple from the TEG test section	
T_{2a}	Hot block 2, 1st thermocouple from the TEG test section	
T_{2b}	Hot block 2, 2nd thermocouple from the TEG test section	
T_{2c}	Hot block 2, 3rd thermocouple from the TEG test section	
T_{2d}	Hot block 2, 4th thermocouple from the TEG test section	
T_{3a}	Hot block 3, 1st thermocouple from the TEG test section	
T_{3b}	Hot block 3, 2nd thermocouple from the TEG test section	
T_{3c}	Hot block 3, 3rd thermocouple from the TEG test section	
T_{3d}	Hot block 3, 4th thermocouple from the TEG test section	
$T_{water\ in\ 1}$	Cold water temperature at inlet mixing chamber	OMEGA Type T thermocouple, 0.065 in Dia
$T_{water\ in\ 2}$	Cold water temperature at inlet mixing chamber	
$T_{water\ in\ 3}$	Cold water temperature at inlet mixing chamber	
$T_{water\ out\ 1}$	Cold water temperature at outlet mixing chamber	
$T_{water\ out\ 2}$	Cold water temperature at outlet mixing chamber	
$T_{water\ out\ 3}$	Cold water temperature at outlet mixing chamber	
V_{output}	Output Voltage of TEG module	Agilent U1253B
V_{OC}	Open Circuit Voltage output of TEG module	
I_{output}	Output Current of TEG module	
$R_{external}$	External Resistance added to the circuit	
R_{TEG}	Internal Resistance of the TEG module	
$V_{input\ heater}$	Input Voltage of both heaters combined	HP 6655A DC Power Supply
$I_{input\ heater}$	Input Current of both heater combined	
V'_{water}	Volumetric Flow Rate of water	Endress+Hauser PROMASS 80

Table 1 – Measured parameters and used measurement tools

Controlling both the chilled water stream temperature and mass flow rate, and input thermal energy through the heater DC power supply, a desired temperature on the hot side of the TEG module can be achieved. The experiment was considered to be in a steady state condition when the hot side temperature rate of change is lower than ± 0.03% per minute. At steady state for a certain desired condition, a minute of measured data is captured and averaged over the minute.

For the hot side, twelve type T thermocouples readings from the hot block 3 jaws around the test section are captured (shown in Figure 39). Each three thermocouples on the same radius was averaged to reduce uncertainty. (T_{1a}, T_{2a}, T_{3a}) are averaged to get T_a and same done to get T_b, T_c and T_d. T_a, T_b, T_c and T_d are the average temperature on the hot block at a radius of 1.137 cm, 2.467 cm, 4.636 cm and 5.359 cm respectively. Average temperatures was plotted against natural logarithm of the radius (an Example of the plot is shown in Figure 42). The slope ($dT/d(\ln r)$) is then obtained from the plot and used to estimate the heat flow through the hot block in the radial direction. Extrapolation of average temperatures is used to estimate the temperature of the hot side of the TEG module

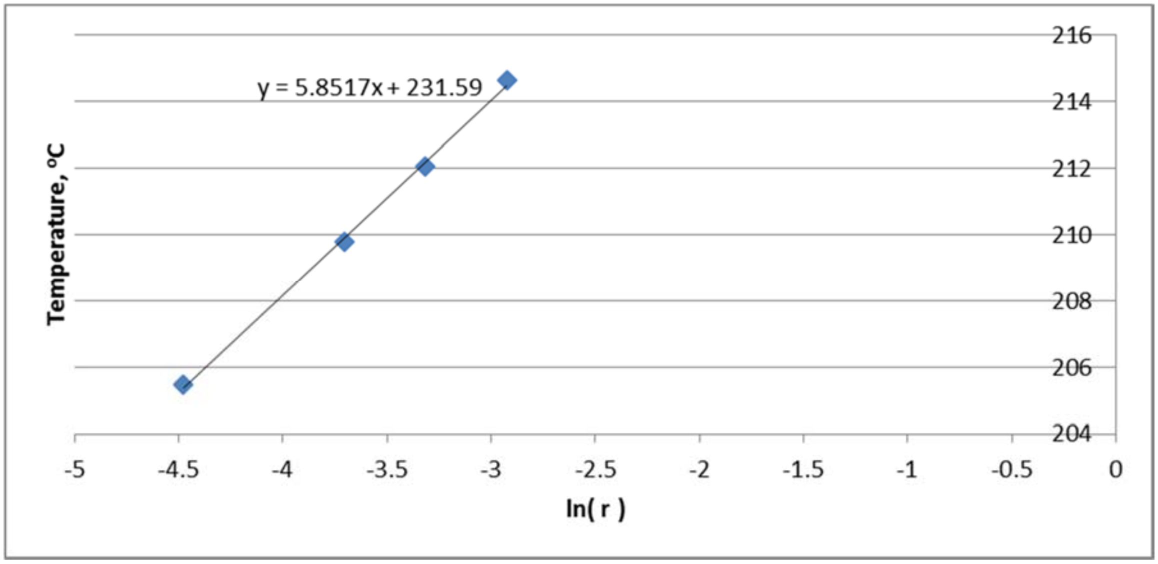

Figure 42-Example of plotting temperature against ln (r) for the Heat block

For the cold side, at steady state for a certain desired condition, a minute of temperatures data is captured and averaged over the minute. $T_{water\ in\ 1}$, $T_{water\ in\ 2}$, $T_{water\ in\ 3}$ are averaged to get $T_{water\ in}$ and $T_{water\ out\ 1}$, $T_{water\ out\ 2}$, $T_{water\ out\ 3}$ are averaged to get $T_{water\ out}$.

The conductive heat transfer flow inside the hot block (Q_{Hot}) can be calculated using,

$$Q_{Hot} = -kA\frac{dT}{dr} = 2k\pi t\frac{(T_{S1}-T_{S2})}{ln(r_{S2}/r_{S1})} \quad \text{Eq. 5. 1}$$

where,

k=16.2 W/(m.K), thermal conductivity of the hot block

t= 38.19 mm

$\frac{(T_{S1}-T_{S2})}{ln(r_{S2}/r_{S1})}$ *is the slope of* T_a, T_b, T_c *and* T_d *plotted against* $ln(r_a)$, $ln(r_b)$, $ln(r_c)$ *and* $ln(r_d)$ *as shown in* Figure 42

The electrical energy supplied to the heater (P_{Heater}),

$$P_{Heater} = V_{input\ heater} I_{input\ heater} \quad \text{Eq. 5. 2}$$

The heat absorbed by the water by convection (Q_{water}),

$$Q_{water} = V' \rho_{water} C_{water} (T_{water\ out} - T_{water\ in}) \quad \text{Eq. 5. 3}$$

where,

ρ_{water} *: Water density*

C_{water} *: Water heat capacity*

The hot side temperature of the TEG module T_{Hot} can be extrapolated from the slope of T_a, T_b, T_c and T_d plotted against $\ln(r_a)$, $\ln(r_b)$, $\ln(r_c)$ and $\ln(r_d)$. Since the hot block in constantly in contact with TEG modules under its weight, the contact resistance is consider to very low compared to the air gap resistance between the TEG module and the pipe (clearance fit air gap) or the convective heat resistance. Therefore, the outer contact resistance between the hot block and the hot side of the TEG module will neglected and extrapolated temperature from the block will be considered to be T_{Hot} of the TEG.

The cold side temperature T_{Cold} can be calculated from the conductive heat transfer inside the TEG module which equals the heat transfer inside the hot block at steady state. Assuming the manufactured thermoelectric material thermal conductivity is equivalent to the reported value in literature for the same composition, T_{Cold} can be calculated from,

$$T_{Cold} = T_{Hot} - Q_{Hot} \frac{ln(r_{outer\ TEG}/r_{inner\ TEG})}{2\pi k_{TEG} t_{TEG}} \quad \text{Eq. 5. 4}$$

where,

$r_{outer\ TEG}$*= 6.35 mm , outer radius of TEG module*

$r_{inner\ TEG}$*= 3.98 mm , inner radius of TEG module*

k_{TEG}*= 1.358* W m^{-1} K^{-1}*, reported thermal conductivity of TEG module material* (Keshavarz Khorasgani, 2014) *and manufacturer data*

t_{TEG}*= 13 mm, height of two TEG couples*

From T_{Hot} and T_{Cold}, differential temperature difference across the TEG module can be calculated,

$$\Delta T_{TEG} = T_H - T_C \qquad \text{Eq. 5. 5}$$

Effective Seebeck Coefficient can be calculated from the measure open circuit voltage V_{OC},

$$\alpha_{eff} = \frac{V_{OC}}{\Delta T_{TEG} * N} \qquad \text{Eq. 5. 6}$$

Where,

N = number of thermoelectric legs

Resistance for heat flow between cold side of the TEG module T_{Cold} and the water can be calculated as follows, this resistance is considered to be the sum of convective heat resistance from the pipe to the water, conductive heat resistance through the pipe wall and conductive heat resistance through the air gap (contact resistance) between the TEG module and the outer surface of the pipe.

$$R_{contact\ resistance+convective+pipe} = \frac{T_{Cold} - T_{water\ average}}{Q_{Hot}} \qquad \text{Eq. 5. 7}$$

5.6 Energy Balance

Through testing different manufacturing parameters and geometries, more than a hundred data points were collected. Forty five of these data points were captured during experiment using a low chilled water flow (0.2 Kg/min or lower) to provide opportunity for an energy balance. Other characterization experiments were carried on using a high flow rate (ranging 2 to 5 Kg/min) to minimize the thermal resistance of the cold side by lowering the convective heat transfer resistance. Experiments in the high flow ate range resulted in the difference of temperature between the water inlet and water outlet (ΔT_{water}) drop down to be as low as 0.03°C creating a near isothermal condition at the TEG cold side surface. This makes calculations of heat transferred to the water in these cases invalid since the uncertainty of water measurement is ± 0.17°C (average of three thermocouples).

Plotted in Figure 43 is the energy balance (Q_{water} against Q_{Hot}) for the experiments that were carried out for the low flow rate range of chilled water. Although the flow was relatively low, the uncertainty of Q_{water} is still high (± 3.54W) as the temperature difference was only within the range of 0.7°C to 1.4°C. While the solid line represents a 45 degrees line of equal Q_{water} and Q_{Hot}, dashed lines represent ± 15% of that. The energy balance shows 70% of data points falling within ± 10%.

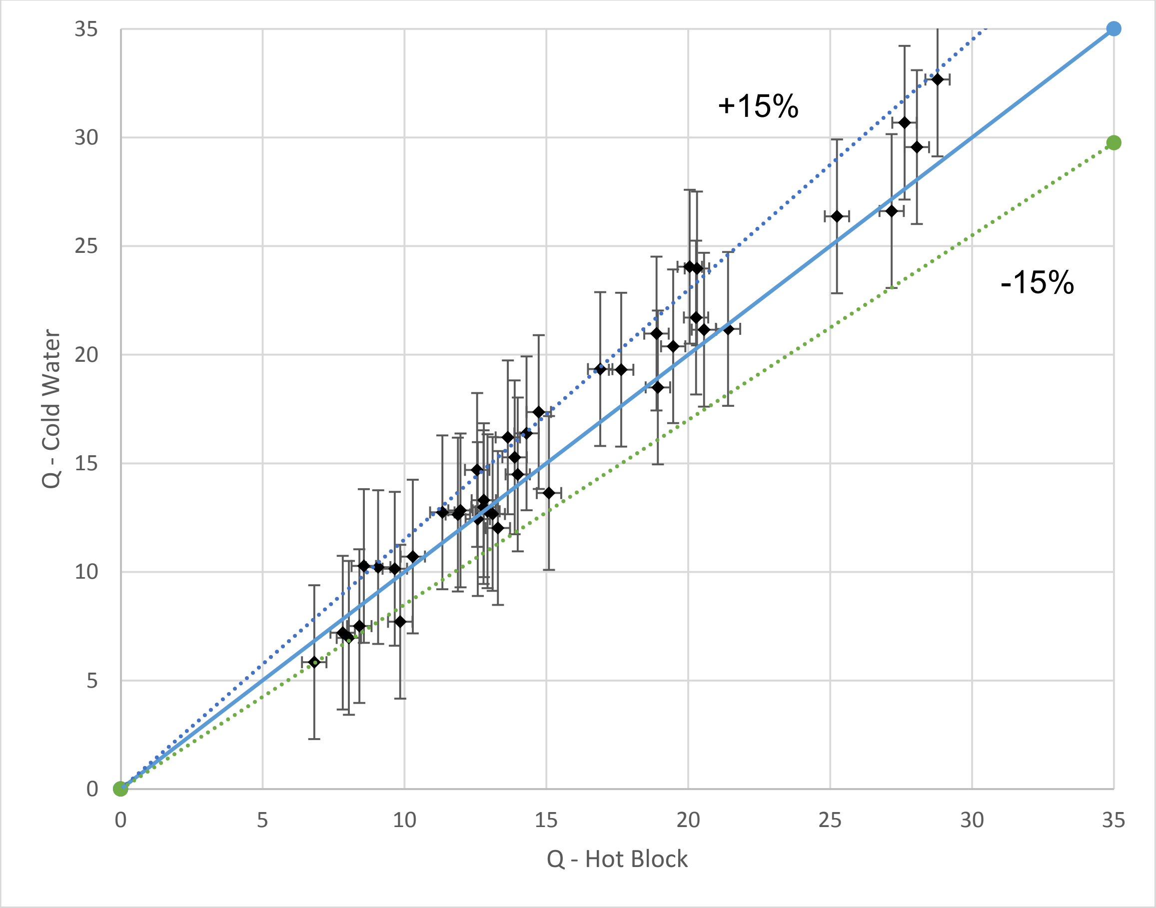

Figure 43 - Energy Balance of experimental data points

5.7 Uncertainty analyses

The Table below summaries the uncertainties of different parameters that were measured or calculated from measured data. Uncertainty was calculated in accordance with Kline & McClintock (1953). Temperature uncertainty was obtained from calibration curves. For both the hot and cold side each three thermocouples are in the same position and are averaged. Further details can be found in Appendix A.

Parameter Symbol	Units	Description	Applicable Range of T_{Hot}	Absolute Uncertainty	Relative Uncertainty
$\delta T_{1a}, \delta T_{2a}$,......	°C	Single thermocouple measurement	60°C to 125°C	± 0.30	
			125°C to 175°C	± 0.42	
			>175°C	± 0.52	
$\delta T_a, \delta T_b, \delta T_c$	°C	Average of three thermocouple measurements	60°C to 125°C	± 0.17	
			125°C to 175°C	± 0.24	
			>175°C	± 0.30	
δQ_w – see note 1	W	Heat transfer to the chilled water	60°C to 240°C	± 3.54	
$\delta Q_H/Q_H$	W	Heat transfer through the Hot block	60°C to 125°C		± 4.44%
			125°C to 175°C		± 4.28%
			>175°C		± 3.80%
δT_{Hot}	°C	Temperature of TEG hot side	60°C to 125°C	± 0.17	
			125°C to 175°C	± 0.24	
			>175°C	± 0.30	
δT_{Cold}	°C	Temperature of TEG cold side	60°C to 125°C	± 2.35	
			125°C to 175°C	± 2.31	
			>175°C	± 2.17	
$\delta \Delta T_{TEG}$	°C	Differential temperature over TEG module	60°C to 125°C	± 2.37	
			125°C to 175°C	± 2.35	
			>175°C	± 2.23	
$\delta T_{TEG\ avg}$	°C	Average temperature	60°C to 125°C	± 1.19	

		over the TEG module	125°C to 175°C	± 1.17	
			>175°C	± 1.12	
δα/α	μV/K	Seebeck Coefficient	60°C to 125°C		± 6.66%
			125°C to 175°C		± 4.30%
			>175°C		± 2.60%
δV	mV	Output measurement	60°C to 240°C		± 0.05%
δV ‘	l/min	Water volumetric flow rate	60°C to 240°C		± 0.15%
Δk	W/(m.K)	Bismuth Telluride Thermal Conductivity	60°C to 240°C	± 0.05	

Table 2 - Uncertainty values for different parameters

Note 1: Heat transfer to chilled water was only calculated for mass flow rate of 0.2 Kg/min and less. Other experiments performed using a high flow rate (ranging 2 to 5 Kg/min), the difference of temperature between the water inlet and water outlet (ΔT_{water}) dropped down to be as low as 0.03°C while uncertainty of water measurement is + 0.17°C (average of three thermocouples). Therefore, heat transfer to chilled water at higher flow rate was not calculated.

Chapter Six: Results and Discussion

6. Results and Discussion

Experiments were performed on the (Min & Rowe, 2007) annular design and the proposed annular V-shaped variation using the TEG tester to study and characterize 2-couple modules. Samples were manufactured using cold pressing then sintering process, assembled into prototypes and characterized for comparison. Key manufacturing parameters were changed systematically to develop the prototype fabrication process. Parameters changed were sintering temperature, pressing pressure, oxide reduction and geometry. Parameter investigation tests will be discussed as it helped to develop the recommended fabrication process. The key performance indicator measured were the thermal performance and effective Seebeck coefficient.

TEG modules prototypes were named according to their fabrication method used, TEG-R-420-1-30-A+31 for example. Table 3 illustrates different syllables of the prototype naming system. A list of all prototypes represented in this document is available in Appendix C.

TEG	R	420	1	30	A+31
	Geometry	Sintering temperature ^{o}C	Sintering hold time hr	Pressing pressure MPa	Oxidation status of the powder
	R: ring-structured	Number: 390 to 430	Number: 1 to 48	Number: 30 to 230	**O:** Oxidized
	V: V-shaped				**OR:** Oxide reduced
					OF: Oxide free
					A+#: Aged after oxide reduction process+ # of days

Table 3 – TEG prototype naming system

Experimental investigation of different key manufacturing parameters targeted development of annular TEG prototype fabrication process, shown chronologically in Figure 44. The fabrication process was updated after each experiment to constantly improve the prototype.

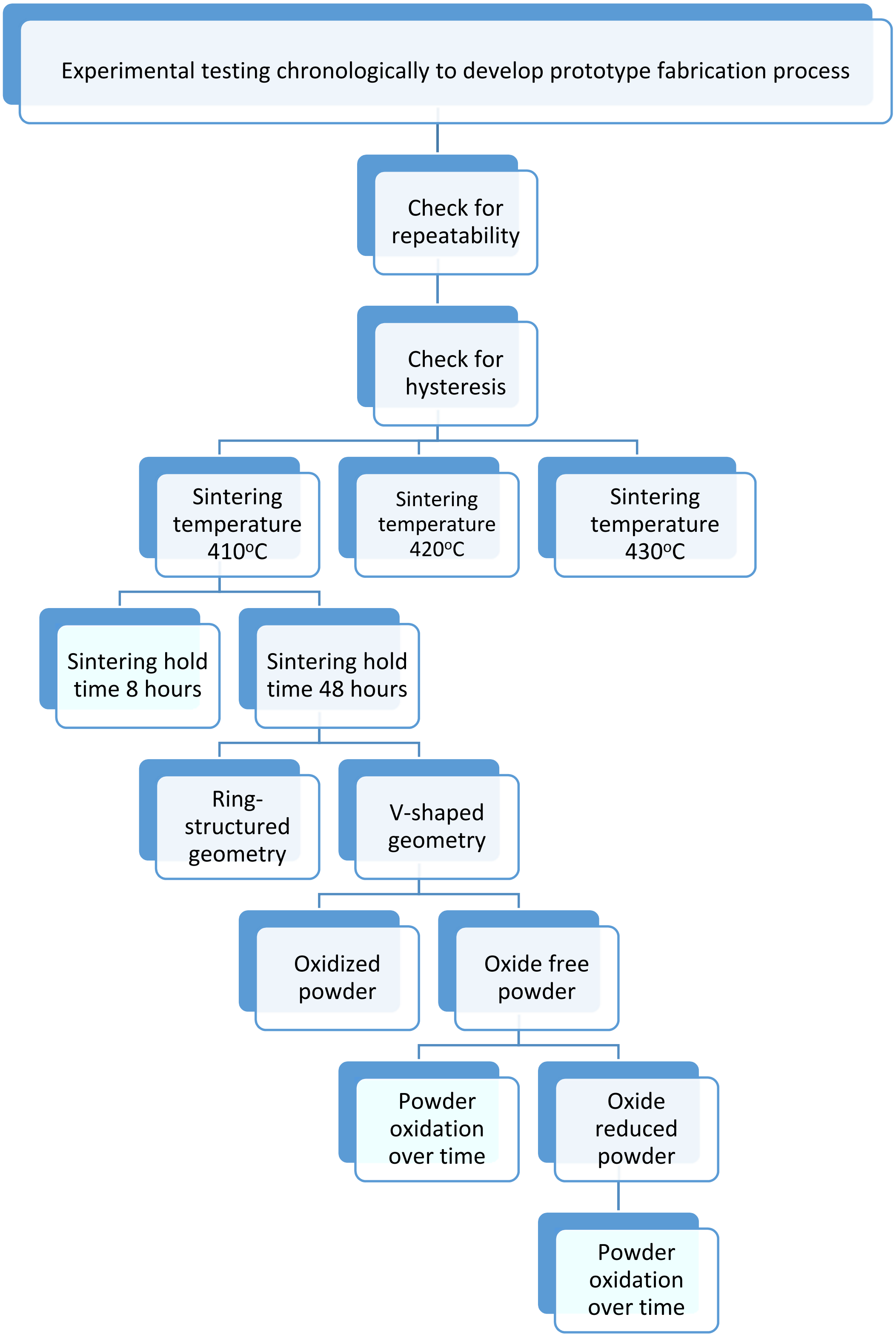

Figure 44 - Experimental testing chronologically

6.1 Test Repeatability

To verify the repeatability of the test procedure, TEG-R-420-1-30-O was tested twice with same setup and assembly to check if same results would be achieved, Figure 48. To check for hysteresis of the facility, date points were captured during ramping up and down of the temperature, Figure 49.

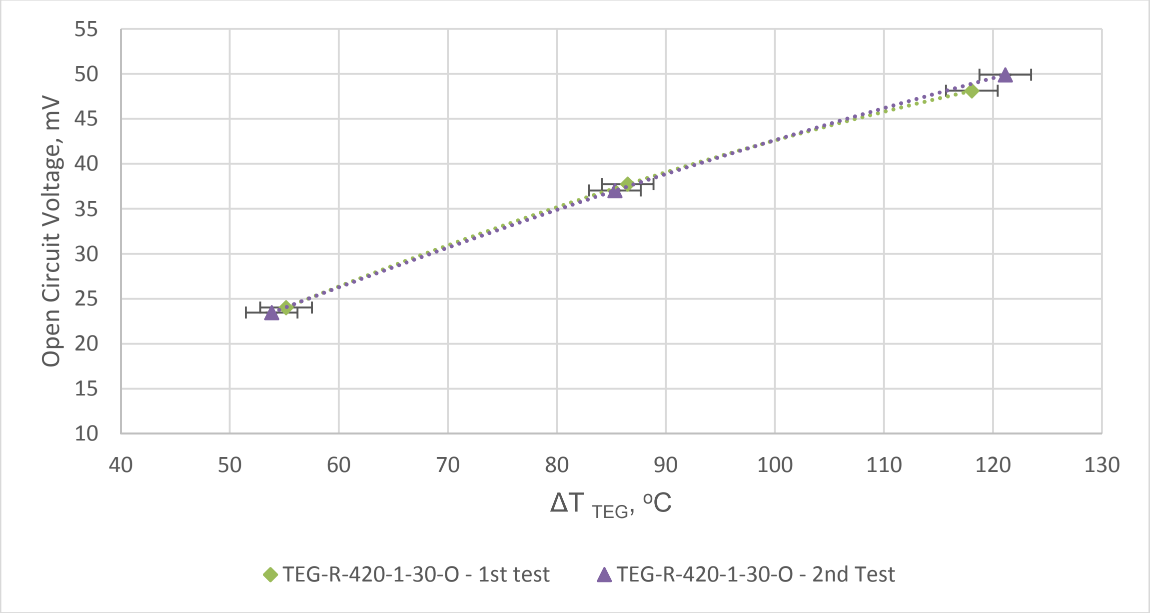

Figure 45 – TEG-R-420-1-30-O- Result showing experiment repeatability

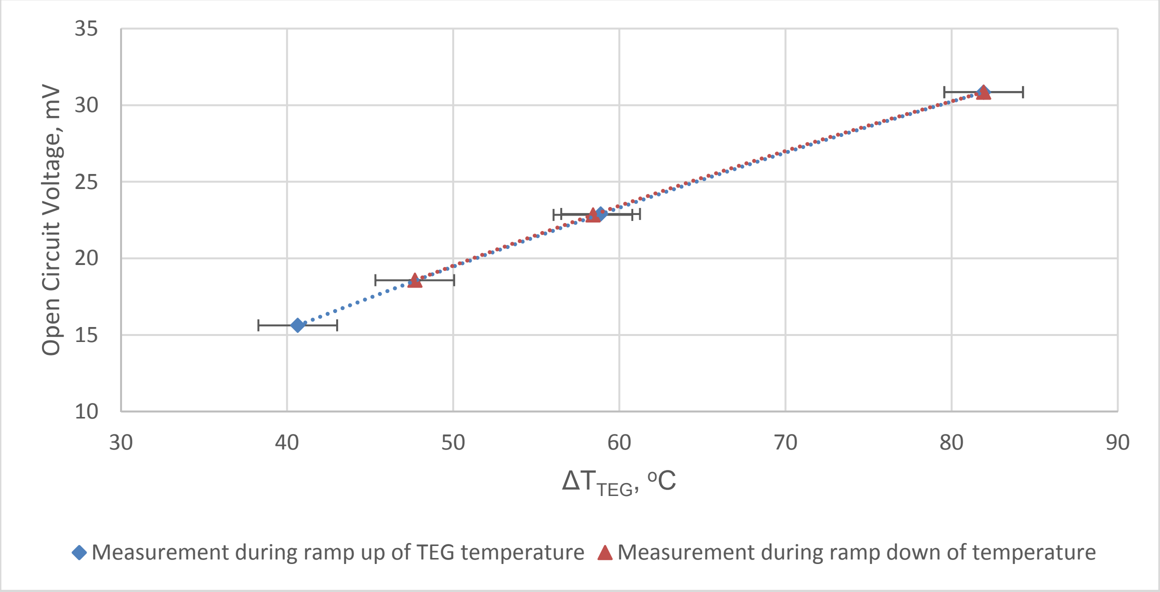

Figure 46 – TEG-R-430-1-30-O - Testing for hysteresis capturing data points during ramping up temperature vs ramping down

Figure 45 shows repeatability test for prototype TEG-R-420-1-30-O with an error of less than 3.5% on higher temperatures. Note that experiment was cooled down and shut off between both experiments and tests were carried on different days. Similarly, Figure 46 shows experiment results to check for hysteresis for prototype TEG-R-430-1-30-O. Data captured during temperature ramp up or down had less than 0.5% difference. That indicates that either approaches for the experiment will not affect the measured results.

6.2 Pressing Pressure

Cold pressing is the process of applying pressure on a powder that has been pre-mounted into a die with no addition of heat. The die contained an inner shaft to produce the desired ring shaped sample. Used pressures reported in literature ranged from 5 MPa (Kosalathip et al., 2008) to 1470 MPa (Arreguin-Zavala et al., 2013). Most common pressures used for bismuth telluride falls into the 400MPa range.

Powder used to produce samples has been found to limit the maximum used pressure during pressing. Same powder composition from two different sources (different suppliers) has been used over the course of the project, one of them allowed for pressure up to 230 MPa, but always cracked if a higher pressure was used. Powder from a second supplier allowed only for pressure up to 130 MPa before it would produce cracked samples.

In early stages of the project, a pressure of 30 MPa was used to press prototypes. Pressing pressure was increased to 230 MPa and 130 MPa for powders from different suppliers (maximum achievable pressure for each). Trials to exceed the mentioned pressure and reach the targeted pressure of 400 MPa were not successful.

6.3 Sintering Process

One of the most crucial steps of manufacturing thermoelectric generators is sintering the sample once it is pressed. After pressing samples, they were arranged inside a slightly wider Pyrex tube with plastic ring spacers. Tubes were then vacuumed, filled with argon and then sealed. Sealed samples are then put into a programmable Klin (furnace) with a controllable rate of ramping up and down temperature, hold temperature and hold time. Temperature elevation and cool down rates are always set to less than $50^{o}C/hr$ to avoid quenching. Quenching bismuth telluride lowers its Seebeck coefficient and increases electric resistivity (Schultz et al., 1962). An example of a sample sintering schedule is shown in Figure 47.

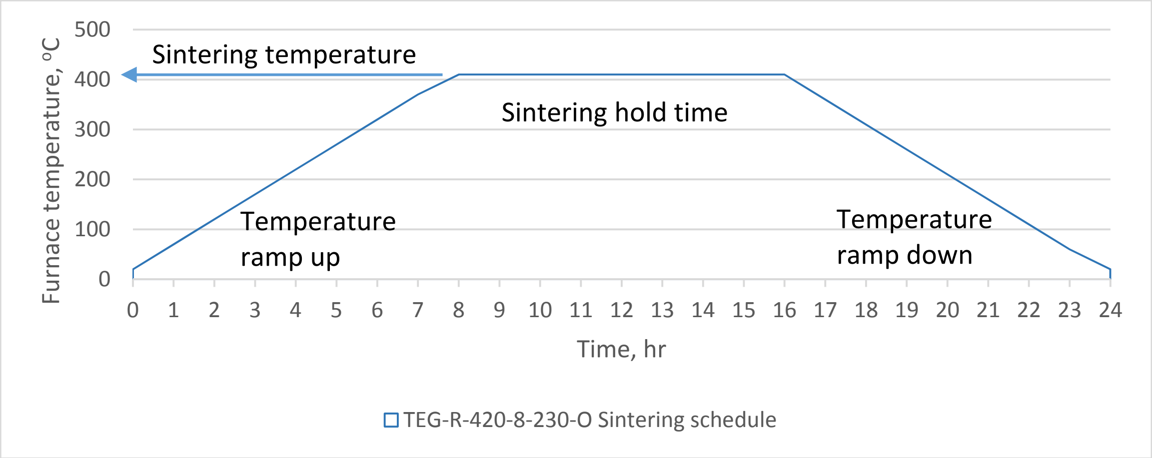

Figure 47 – An example of a sintering schedule

Performance of TEG modules will be compared based on open circuit voltage (V_{oc}) produced by the module against the differential temperature across the TEG module (ΔT_{TEG}). Open circuit voltage produced is dependent on the effective Seebeck coefficient of the sample, which indicates both the material property of the produced material and the heat and electricity flow patterns inside the TEG module. Electric current measurements were excluded from results as the test section is only mechanically assembled not chemically bonded which led to a significant electrical contact resistance between thermoelectric rings.

6.3.1 Comparing Samples Sintered at 410°C vs 420°C vs 430°C

Samples were manufactured and tested to compare the effect of different sintering temperatures on the performance of the TEG module. Prototype samples were pressed and sintered at 410°C, 420°C and 430°C degrees, then experimentally tested for performance comparison. Samples sintered at temperatures higher than 430°C grew over 5%in size which made them out of shape. Samples sintered at temperatures lower than 410°C did not show visual change as the temperature is not high enough to sinter the material. Samples that were sintered at 420°C and 430°C for 1 hour showed a sintered visual structure that is different that of a pressed powder appearance pre sintering. Samples sintered at 410°C had to be sintered for at least 8 hours to show similar sintered visual appearance. All rings tested had a ring-structured geometry similar to the ones (Min & Rowe, 2007) tested.

Test results plotted in Figure 48 show a higher open circuit voltage for TEG modules sintered at 420°C produced at a certain ΔT_{TEG}. Suggesting that there is an optimum temperature for sintering. Although samples sintered at 420°C performed better than the ones sintered at 410°C, it showed growth in size after sintering of more than 2% which is unacceptable for a final product dimension. Therefore future comparison tests were carried using a sintering temperature of 410°C.

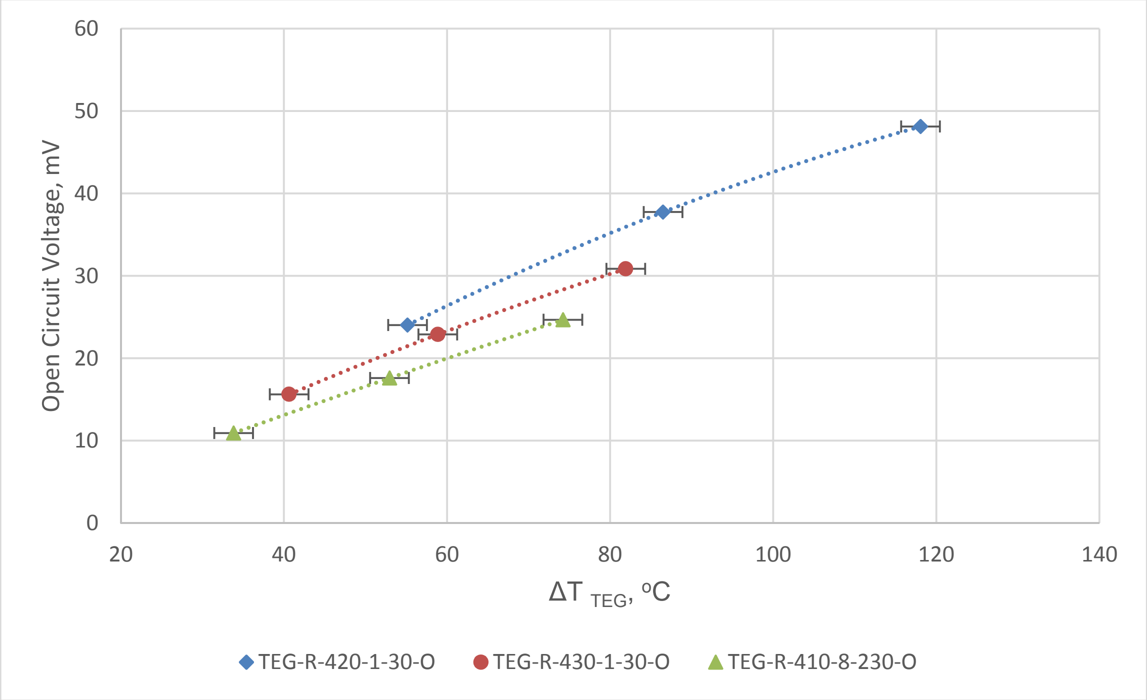

Figure 48 – Comparison of open circuit voltage for prototypes sintered at 410°C, 420°C and 430°C

Prototype	*TEG-R-410-8-230-O*	*TEG-R-420-1-30-O*	*TEG-R-430-1-30-O*
Sintering Temp	410°C	420°C	430°C
Sintering hold time	8 hr	1 hr	1 hr
Pressing Pressure	230 MPa	30 MPa	30MPa
Geometry	Ring-structured	Ring-structured	Ring-structured
Furnace used	Paragon Sc-2		

Table 4 - Prototypes represented in Figure 48, sintered at 410°C, 420°C and 430°C

6.3.2 Comparing samples Sintered for 8 hours vs 48 hours

Literature suggested (Francombe, 1958; Hyun et al., 2001) sintering bismuth telluride samples for more than 48 hours improved Seebeck coefficient. Longer sintering hold time at elevated temperature should allow Seebeck coefficient to increase and anneal the sample improving mechanical properties. Plotted in Figure 49 are results of testing two samples, TEG-R-410-8-230-O was sintered for 8 hours, while TEG-R-410-48-230-O was sintered for 48 hours. All other factors were kept constant. It has been found that longer sintering time produce samples with slightly higher Seebeck coefficient and therefore slightly better performance (open circuit voltage).

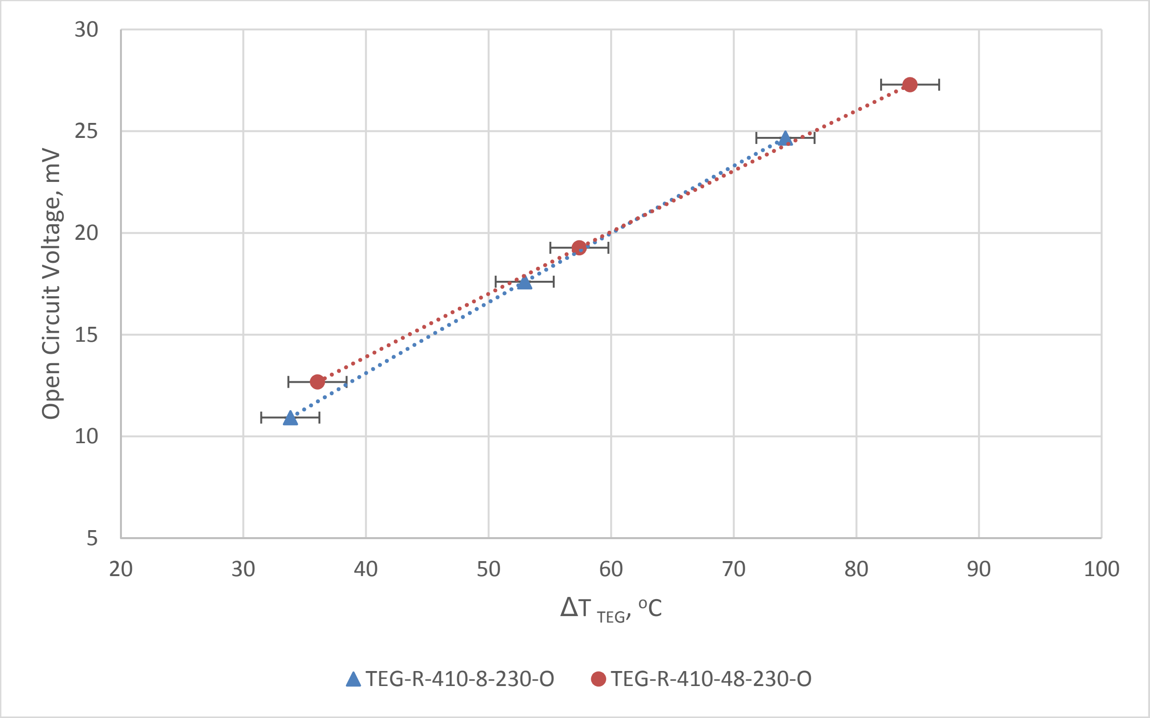

Figure 49 – Comparison of open circuit voltage for prototypes sintered for 8 hours and 48 hours

Prototype	*TEG-R-410-8-230-O*	*TEG-R-410-48-230-O*
Sintering Temp	410^{o}C	410^{o}C
Sintering hold time	8 hr	48 hr
Pressing Pressure	230 MPa	230 MPa
Geometry	Ring-structured	Ring-structured
Furnace used	Paragon Sc-2	

Table 5 – Prototypes represented in Figure 49, sintered for 8 hours and 48 hours

6.3.3 Comparing Sintering P&N-types at different temperatures

It was suggested by literature that sintering P-type modules at 200ºC would increase its Seebeck coefficient (Schultz et al., 1962). So TEG-V-410/200-48-230-O was assembled using a P-type ring sintered at 200ºC and combined with N-type ring that has been sintered at 410 degrees. This annular TEG module was tested and results are plotted in Figure 50 against TEG-V-410-48-230-O that has both P & N sintered at 410 degrees. The comparison shows that for the samples considered the suggested effect of low P-type sintering temperature was not observed.

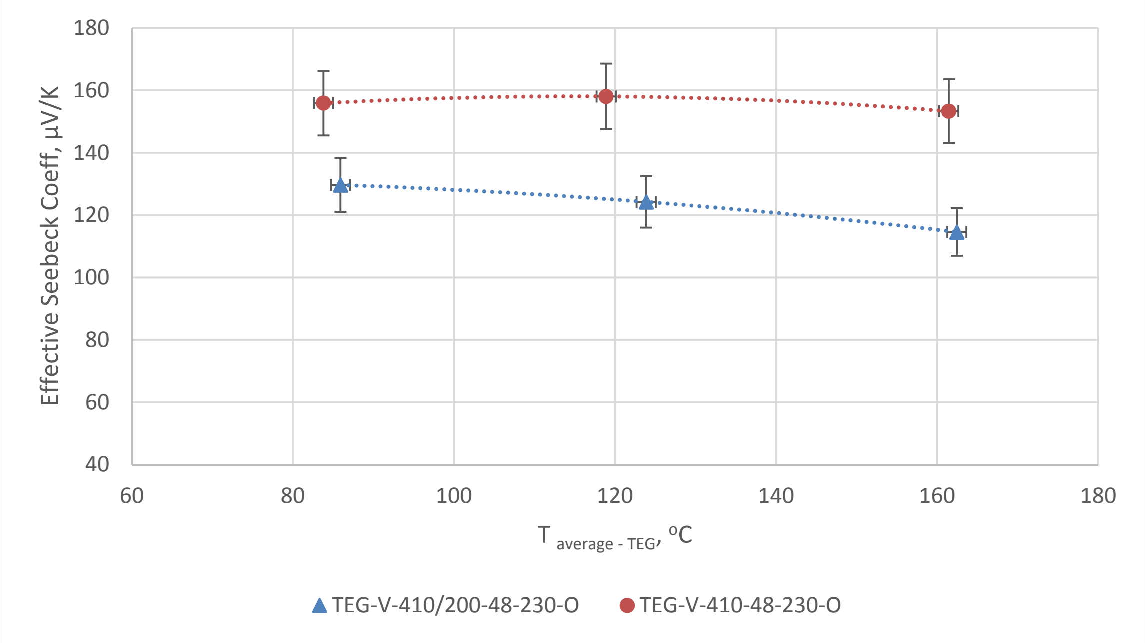

Figure 50 – Comparison of Seebeck coefficient for prototype manufactured at 200ºC and 410ºC degrees vs prototype with both ring manufactured at 410ºC

Prototype	*TEG-V-410/ 200-48-230-O*	*TEG-V-410- 410-48-230-O*
Sintering Temp	P-type 200ºC, N-type 410ºC	P-type 410ºC, N-type 410ºC
Sintering hold time	48 hr	48 hr
Pressing Pressure	230 MPa	230 MPa
Geometry	V-Shaped Ring	V-Shaped Ring
Furnace used	Paragon Sc-2	

Table 6 - Prototypes represented in Figure 50, prototype manufactured at 200ºC and 410ºC degrees vs prototype with both ring manufactured at 410ºC

6.4 Investigating a Novel Ring Shaped Geometry

Min & Rowe (2007) experimental results for ring-structured thermoelectric generators did not meet the forecasted performance by their analytical model. One concern is that there is a heat path flow between the conductor rings inner edges in Min & Rowe's design. The concern is that due to the metal rings heat is only flowing through a portion of the annular ring material, therefore lowering produced electric power. A novel design for the p-type ring geometry has been proposed to improve heat path inside the ring which would utilize more of the material into power production, making the geometry more efficient than the ring-structured module.

A module assembly (TEG-V-410-48-230-O) of 2 P-type V-shaped rings and 2 N-type ring-structured elements was manufactured, tested and compared against an assembly (TEG-R-410-48-230-O) of two thermocouples with all four rings manufactured into ring-structured elements. Results for testing both prototypes are plotted in Figure 51 which shows V-Shaped TEG module with a higher performance compared to ring-structured modules. The hypothesis is that better material utilization through improved heat flow patterns is the reason behind the higher effective Seebeck coefficient achieved and therefore a higher open circuit voltage was produced. This hypothesis is assessed further through a numerical study in the following section. Plotted on Figure 51, additional to both fabricated prototypes, is theoretical value of open circuit voltage (calculated based on material property, maximum achievable) and Min & Rowe (2007) prototype results for comparison. Both prototypes tested were fabricated from oxidized powder, therefore the ring-structured prototype produced less open circuit voltage than Min & Rowe's reported prototype. The trend of improvement moving from ring-structured to V-shaped is consistent and verified using numerical simulation. The percentage of improvement was not quantified using this test due to oxidation of the powder.

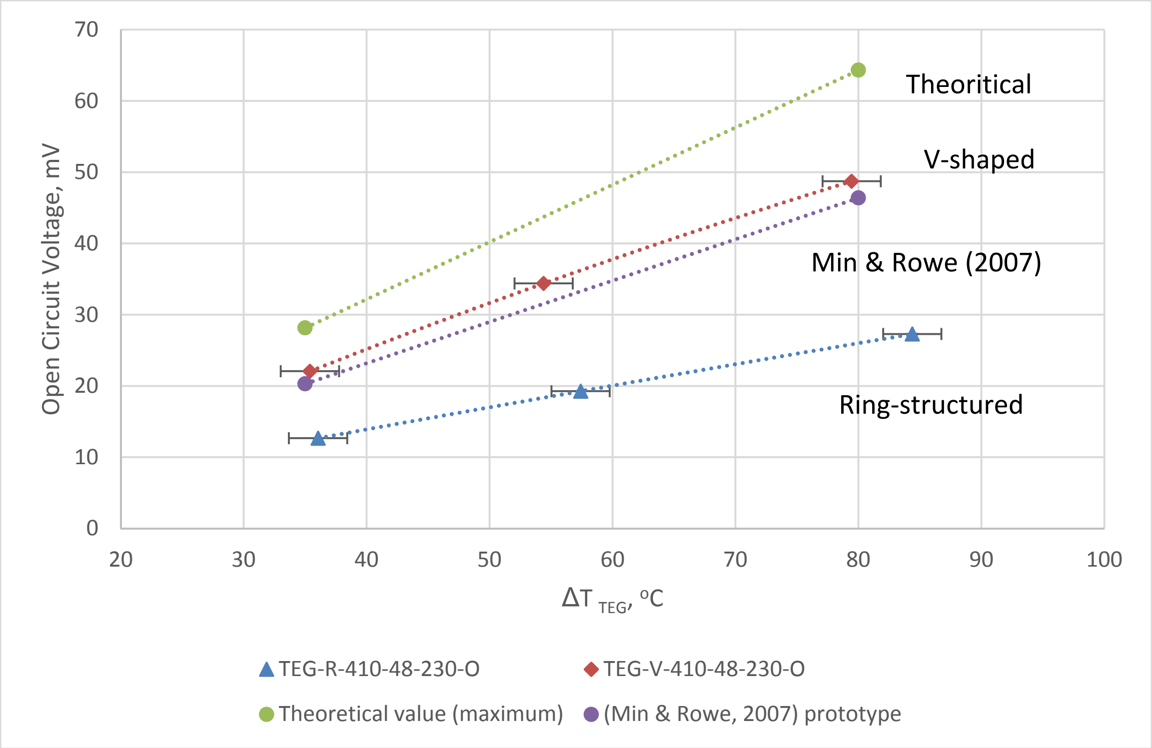

Figure 51 - Comparing effect of geometry on open circuit voltage, V-shaped TEG module vs ring-structured module

Prototype	*TEG-R-410-48-230-O*	*TEG-V-410-48-230-O*
Sintering Temp	410°C	410°C
Sintering hold time	48 hr	48 hr
Pressing Pressure	230 MPa	230 MPa
Geometry	Ring-structured	V-Shaped Ring
Furnace used	Paragon Sc-2	

Table 7 - Prototypes represented in Figure 51, V-shaped TEG module vs regular ring shaped module

6.5 Powder Oxidation

6.5.1 Detecting Oxides

Early manufacturing trials, dimension growth during sintering process was observed. Suspecting the powder to be contaminated with oxides, X-ray diffraction on two powders was performed. Powder A, stored in air, suspected to be contaminated with oxides and Powder B, stored in Argon, expected to be oxide free. P & N-type samples were tested for each of powder A & B. Results show that oxygen has been detected in one sample of the four. Oxide was detected in the P-type powder A sample in the form of Sb_2O_3.

It was expected to detect tellurium oxides and bismuth oxides in the form of Bi_2O_3 and TeO_3 in powder A, but XRD did not detect them. XRD resolution for the facility used is around 40 nm but bismuth and tellurium oxide layer thickness can be as small as 1.5 nm around powder grains (Bando et al., 2000). This test was determined inconclusive to quantify existence of oxides in bismuth telluride unless a higher resolution was used.

A different test was performed on samples made from a powder suspected to be oxide contaminated and a powder that had undergone a dry oxide reduction process. Samples were pressed from both powders, then heated up to 430^{o}C under XRD to compare behaviour during elevation of temperature. Samples from the oxidised Powder A has been found to grow in size excessively during sintering process. Results indicate that oxide reduction process has impacted material behaviour, meaning that the powder was indeed contaminated with oxides. Samples that was manufactured from oxide contaminated powder experienced more expansion during temperature elevation and suffered from five times more permanent size growth after sample cool down.

6.5.2 Testing New Powder

Suspecting that the mechanical alloyed powder used is oxidized, a different powder batch was brought from manufacturer (same chemical composition) in an argon sealed container. Samples from both oxidized powder and the powder from the argon sealed container (believed to be oxide free) were manufactured and experimentally tested. Results plotted in Figure 52 shows that Prototype made from the oxide free powder B (TEG-V-410-48-130-OF) performed better than oxide contaminated powder A (TEG-V-410-48-230-O). Both powders were pressed at their maximum pressure. Comparing the effective measured Seebeck coefficient of both samples (Figure 53) showed more than 15% improvement in samples manufactured from a manufacturer argon sealed container.

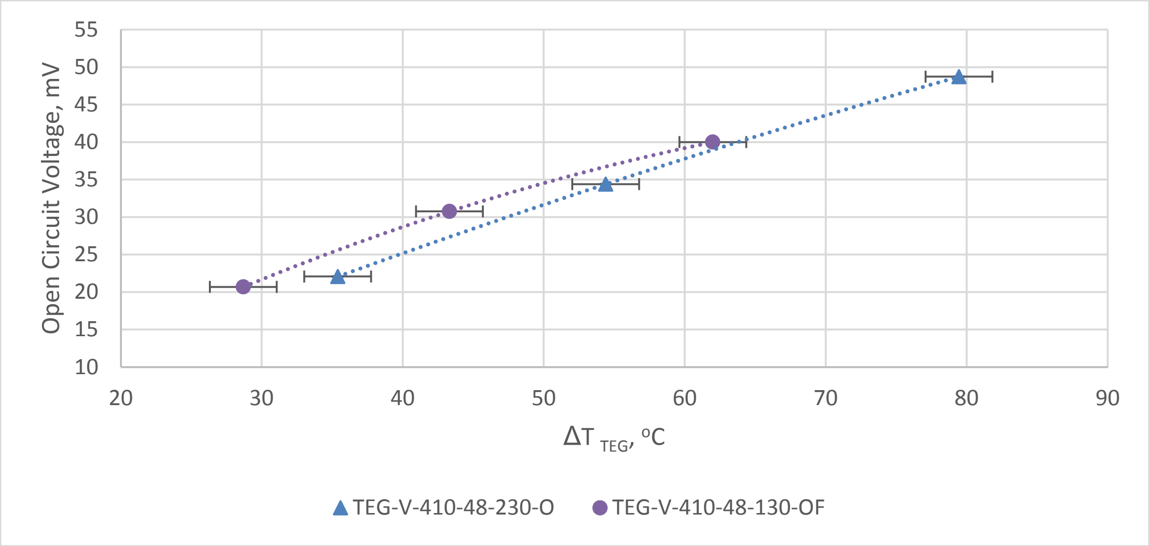

Figure 52 – Comparison of open circuit voltage for prototypes manufactured from oxidized and oxide free powders

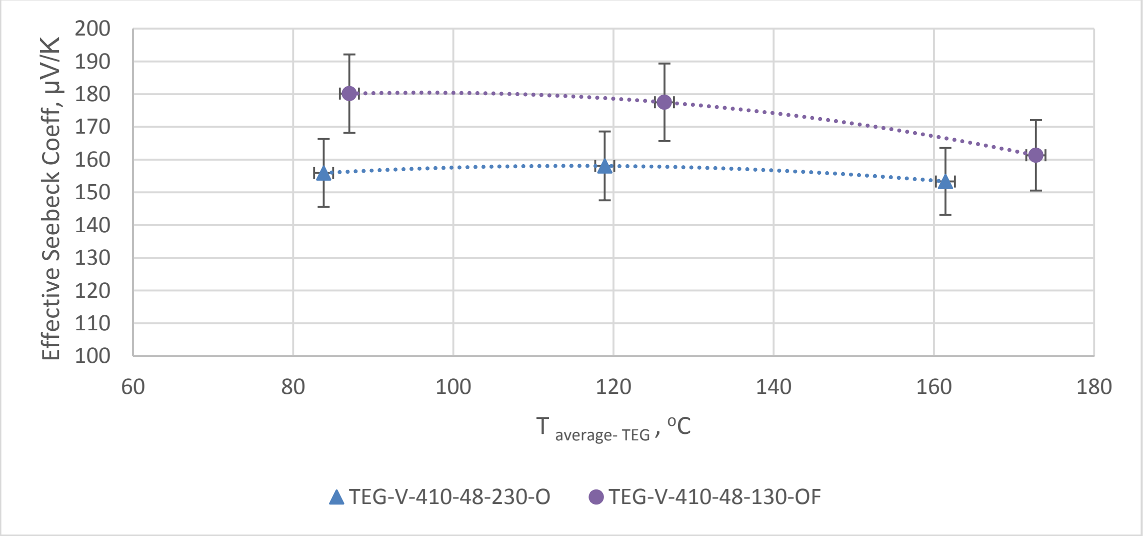

Figure 53 – Comparison of effective Seebeck coefficient for prototypes manufactured from oxidized and oxide free powders

Prototype	*TEG-V-410-48-230-O*	*TEG-V-410-48-130-OF*
Sintering Temp	410°C	410°C
Sintering hold time	48 hr	48 hr
Pressing Pressure	230 MPa	130 MPa
Geometry	V-Shaped Ring	V-Shaped Ring
Furnace used	Paragon Sc-2	

Table 8 - Prototypes represented in Figure 52 & Figure 53, prototypes manufactured from oxidized and oxide free powders

6.5.3 Deterioration of performance over time

As discussed in the previous section, suspecting that the mechanical alloyed powder used to be oxidized, a different powder batch was brought from manufacturer (same chemical composition) in an argon sealed container. Fifty-four days after the manufacturer vacuum sealed containers were opened and exposed to air, TEG-V-410-48-130-A+54 was fabricated from the powder that is suspected to be oxide contaminated. Results for the prototype were plotted against the oxide free prototype fabricated from the argon sealed container (TEG-V-410-48-130-OF). Results in Figure 54 and Figure 55 showed 20% deterioration in performance due to oxide contamination due to air exposure for 54 days.

6.5.4 Reducing Oxides in Bismuth Telluride

To summarize, a comparison of effective Seebeck coefficient and open circuit voltage between prototypes made from an oxide contaminated powder and an oxide free powder showed superior performance to the new powder. Within 54 days of air exposure the powder got contaminated and performance dropped by 20%. Therefore means of oxygen reduction was carried on the powder. The whole manufacturing process was modified to eliminate or minimize powder exposure to oxygen.

To remove oxides, bismuth telluride powder was exposed for flowing stream of hydrogen while in a tube heater with temperature elevated to 350^{o}C for six hours. Once the oxide reduction process was completed, the powder was sealed in a glove box that has a preserved argon inert environment.

Extra measures were taken afterwards to ensure the powder would not be exposed to oxygen during the manufacturing process. The powder was pre-pressed inside a glove box, then moved outside the glove box while still inside the die to be pressed on a more powerful press to the target pressure. After pressing the sample it was moved back to the glove box where it was put in a Pyrex vial. Capped Pyrex vials filled with argon from the glove box are then moved to where they are vacuumed, filled with argon and sealed.

TEG-V-430-48-130-OR was assembled from the oxide reduced samples, tested and compared to the prototype that was oxide contaminated. Figure 56 shows that the oxide reduced prototype successfully restored its original performance before contamination. Comparing the effective measured Seebeck coefficient of both samples (Figure 57) showed more than 26% improvement due to oxide reduction process in addition to 20% less permanent growth experienced due to temperature elevation (quantified using XRD test).

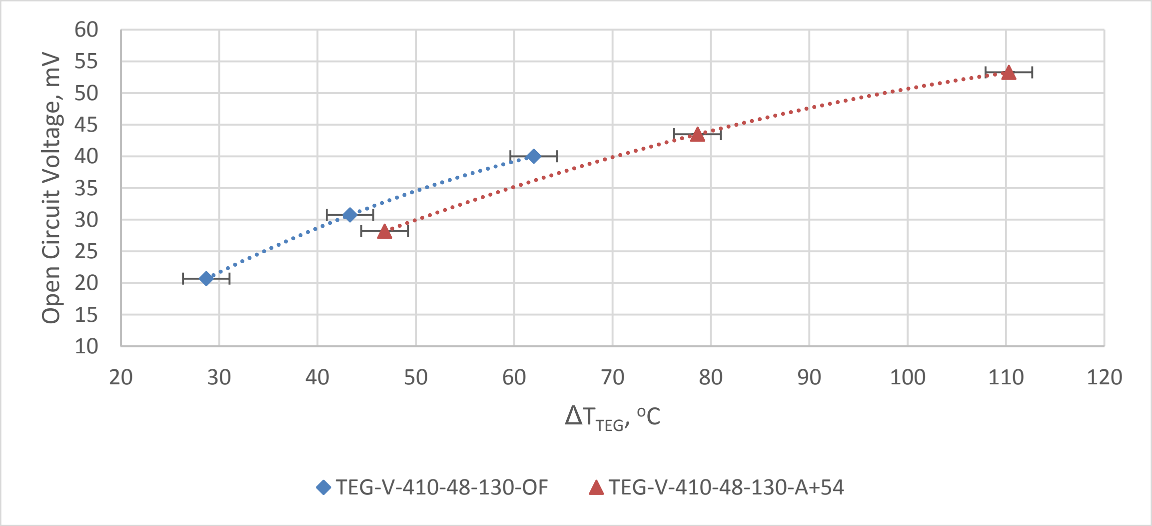

Figure 54 – Comparison of open circuit voltage for prototypes made from an oxide free powder vs a powder after 54 days of air exposure

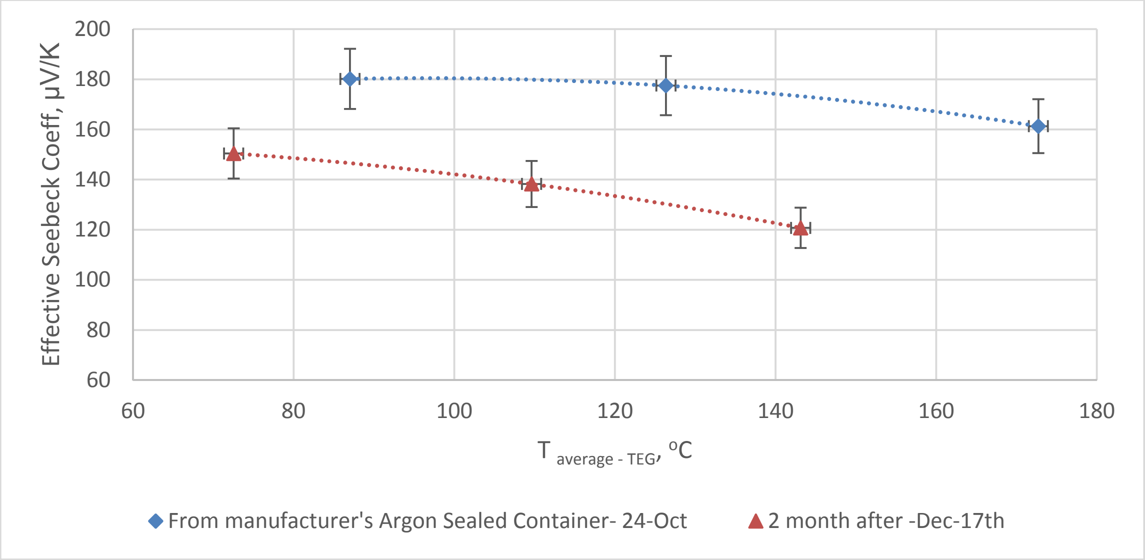

Figure 55 – Comparison of effective Seebeck coefficient for prototypes made from an oxide free powder vs a powder after 54 days of air exposure

Prototype	*TEG-V-410-48-130-OF*	*TEG-V-410-48-140-A+54*
Sintering Temp	410°C	410°C
Sintering hold time	48 hr	48 hr
Pressing Pressure	130 MPa	130 MPa
Geometry	V-Shaped Ring	V-Shaped Ring
Furnace used	Paragon Sc-2	

Table 9 – Prototypes represented in Figure 54 and Figure 55, made from an oxide free powder vs a powder after 54 days of air exposure

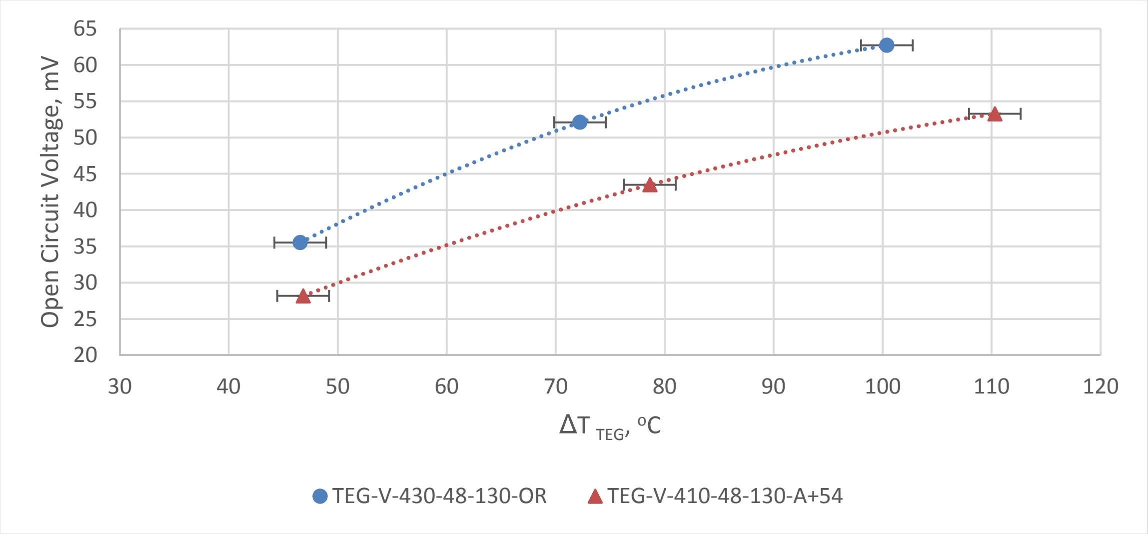

Figure 56 – Comparison of open circuit voltage for prototypes fabricated from a powder before and after oxide reduction process

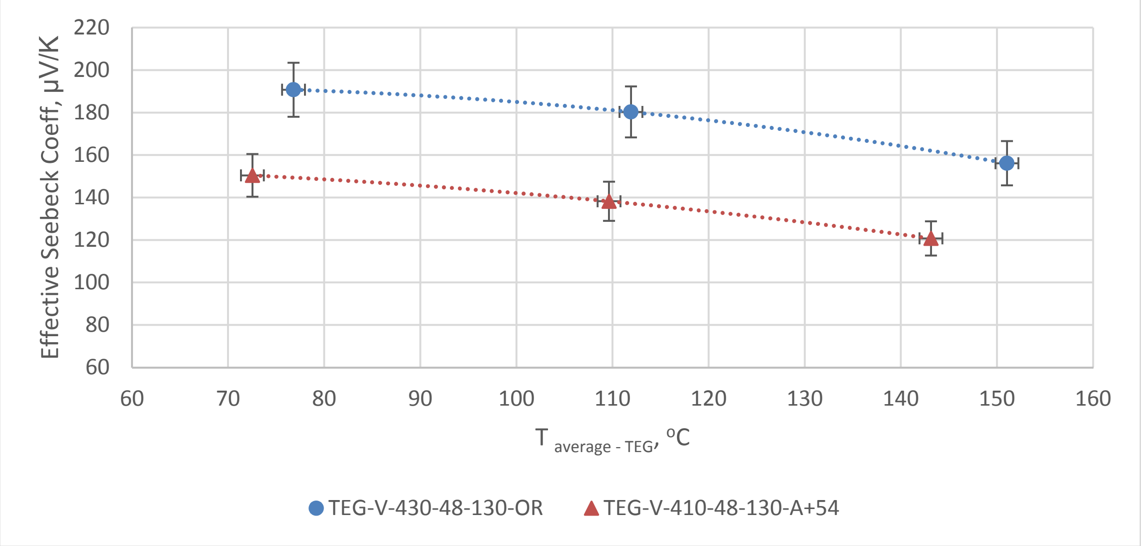

Figure 57 – Comparison of effective Seebeck coefficient for prototypes fabricated from a powder before and after oxide reduction process

Prototype	*TEG-V-430-48-130-OR*	*TEG-V-410-48-130-A+54*
Sintering Temp	430°C	410°C
Sintering hold time	48 hr	48 hr
Pressing Pressure	130 MPa	130 MPa
Geometry	V-Shaped Ring	V-Shaped Ring
Furnace used	Barnstead thermolyne 1500	Paragon Sc-2

Table 10 – prototypes represented in Figure 56 and Figure 57, fabricated from a powder before and after oxide reduction process

TEG-V-430-48-130-OR and TEG-V-410-48-130-A+54 were sintered using different furnaces in different locations. The temperature of the sample during sintering is not precisely the set temperature of the furnace, the actual exposure temperature depends on the furnace model, age, internal dimensions and location. TEG-V-430-48-130-OR was sintered in the furnace (Barnstead thermolyne 1500) that is located inside a draft hood. The moving air inside the draft hood is suspected to increase infiltration inside the furnace and therefore lower the actual temperature of the sample. An equivalent sintering temperature had to be found for the different furnace. A 430^{o}C set temperature in the furnace (Barnstead thermolyne 1500) located in a draft hood was found to be equivalent to a 410^{o}C set temperature in the furnace Paragon Sc-2 (not in a draft hood).

Although the oxygen-reduced powder was kept inside a glove box with an inert environment, it has been observed that performance of fabricated samples from the powder is deteriorating over time. Prototype fabricated 84 days and 103 days after the oxide reduction process (TEG-V-390-48-130-A+84 & TEG-V-390-48-130-A+103) were tested and compared against the prototype fabricated on the day of the oxide reduction process (TEG-V-430-48-130-OR) as shown in Figure 58 and Figure 59.

Note that due to another change of furnace model and location, an equivalent set temperature was found. Where a 430^{o}C set temperature in the furnace (Barnstead thermolyne 1500) located in a draft hood was equivalent to a 390^{o}C set temperature in the furnace Paragon Sc-2 (b).

Results indicates that means of oxide reduction has to be performed on the powder just before the pressing process to obtain maximum repeatable performance. Storing the powder in a glove box that is believed to be kept oxygen free slows down the oxidation process but the powder does oxidize over time. This is likely due to a combination of infiltration of air into the glove box, contamination and oxidation of the container walls used to store the powder. Same observation was confirmed through a private conversation with an expert in this field (Kauzlarich, Susan, Department of Chemistry, University of California, 2015).

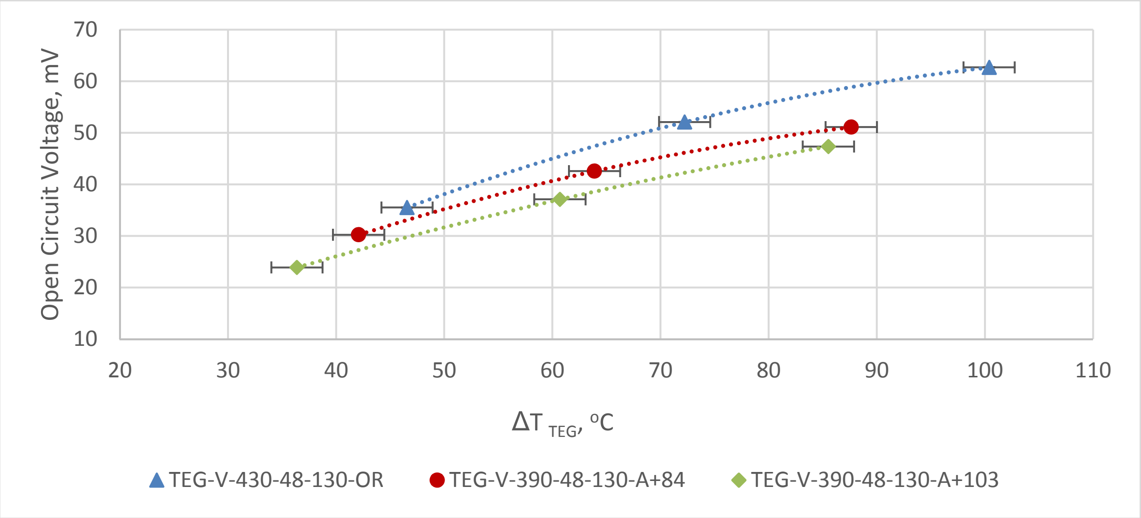

Figure 58 - Deterioration in open circuit voltage of prototypes due to oxidation

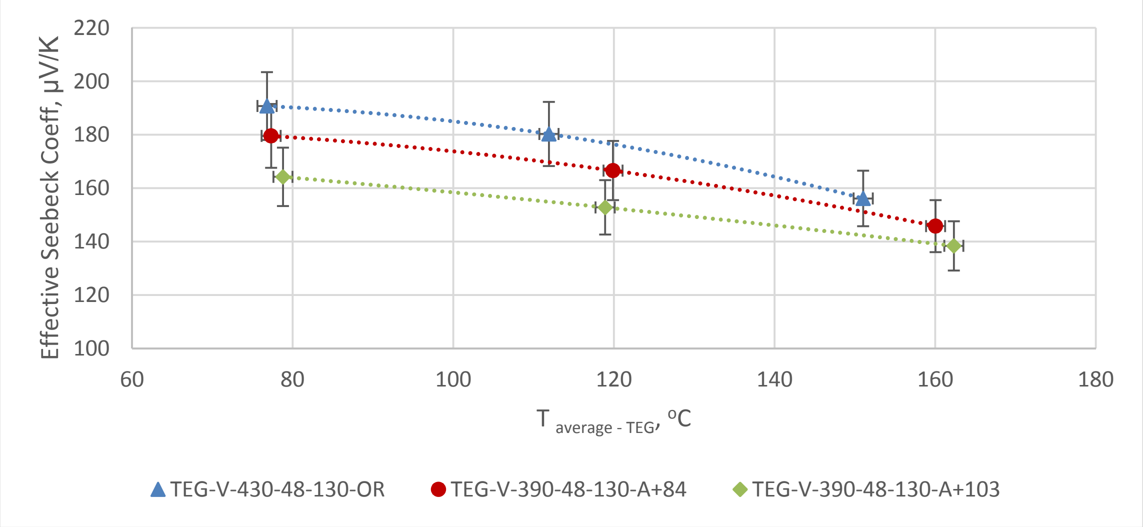

Figure 59 – Deterioration in effective Seebeck coefficient of prototypes due to oxidation

Prototype	*TEG-V-430-48-130-OR*	*TEG-V-390-48-130-A+84*	*TEG-V-390-48-130-A+103*
Sintering Temp	430°C	390°C	390°C
Sintering hold time	48 hr	48 hr	48 hr
Pressing Pressure	130 MPa	130 MPa	130MPa
Geometry	V-Shaped Ring	V-Shaped Ring	V-Shaped Ring
Furnace used	Barnstead thermolyne 1500	Paragon Sc-2 (b)	

Table 11 - Prototypes represented in Figure 58 and Figure 59, Deterioration in performance due to powder oxidation

6.6 Effect of changing chilled water parameters

Heat transfer to the flowing chilled water on the cold side of the TEG prototype is forced convection. The targeted heat transfer coefficient can be estimated analytically through the following equations,

Reynolds number (Re_D) for flow in a circular tube is defined as,

$$Re_D = \frac{u_m D}{\nu} \qquad \text{Eq. 6. 1}$$

where,

u_m *: The mean velocity over the tube cross section*

D : Tube diameter in a fully developed flow

v : Kinematic viscosity of chilled water

In case of laminar flow ($Re_D < 2300$) (Bergman & Incropera, 2011)

Nusselt number (Nu_D) for a constant heat flux can be calculated by,

$$Nu_D = \frac{hD}{k} = 4.36 \qquad \text{Eq. 6. 2}$$

where,

h : Heat transfer coefficient

k : Thermal conductivity of chilled water

Developing: $3000 < Re_D < 10,000$ Gnielinski correlation was used (Gnielinski, 1976),

$$Nu_D = \frac{(f/8)(Re_D - 1000)Pr}{1 + 12.7(f/8)^{1/2}\left(Pr^{2/3} - 1\right)} = \frac{hD}{k} \qquad \text{Eq. 6. 3}$$

where,

f : friction factor, obtained from $\mathrm{f} = (0.790 \ln Re_D - 1.64)^{-2}$

Pr : Prandtl number for chilled water

For $Re_D > 10,000$ Dittus-Boelter correlation was used [17]

$$Nu_D = 0.023\, Re_D^{4/5} Pr^n \qquad \text{Eq. 6. 4}$$

where,

n : for heating of internal flow, n =0.4

The range of convective heat transfer coefficients that the test facility is able to achieve is plotted based on Eq 6.2 – 6.4 in Figure 60.

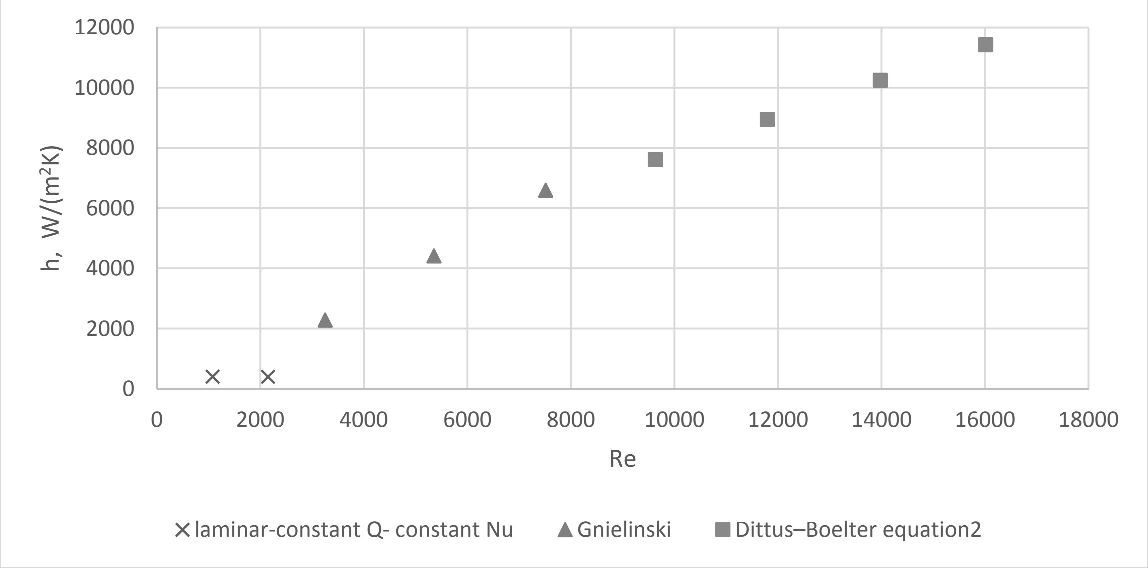

Figure 60 - Convective Heat transfer coefficient for the test section according to correlations

Experiments were performed to study the effect of changing chilled water parameters on the TEG module performance. Parameters tested includes changing the water mass flow rate and temperature.

6.6.1 Changing Water Flow

As chilled water flow is increased, convective heat transfer coefficient increases and convection resistance decreases. Therefore as observed in Figure 61 total heat transfer resistance decreases. Total resistance calculated from experimental data includes TEG inner surface contact resistance, pipe thickness conduction resistance and convection resistance. It is observed that mass flow rate increase up to 1.5 g/min reduced total resistance by around 5% as fluid is transitioning to a turbulent flow. Total resistance does not change significantly for flows over 3 Kg/min as convection resistance becomes less dominant compared to TEG rings resistance and inner contact resistance (clearance air gap between TEG rings and pipe).

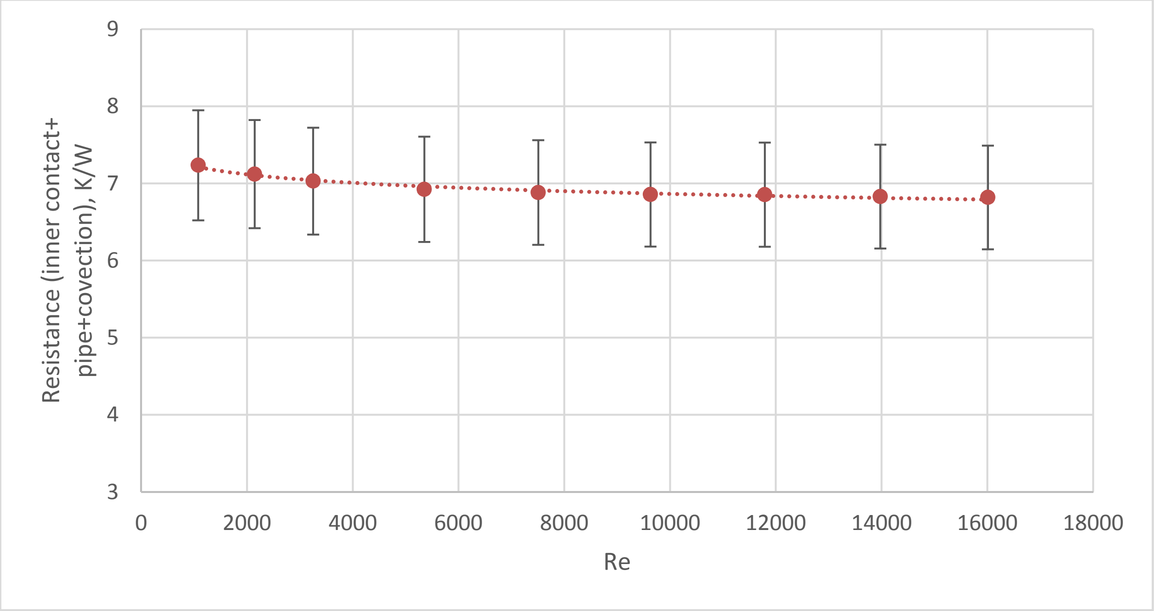

Figure 61 - Effect of changing flow rate on total heat resistance on the cold side

When chilled water flow is increased, convection heat transfer coefficient increase, water convective heat resistance decrease and the cold side temperature of the TEG module decreases. This leads to the increase of differential temperature across the TEG module as measured and plotted in Figure 62 (TEG-V-410-48-130-A+25 at $T_{TEG - Hot}$ of 99.3^{o}C).

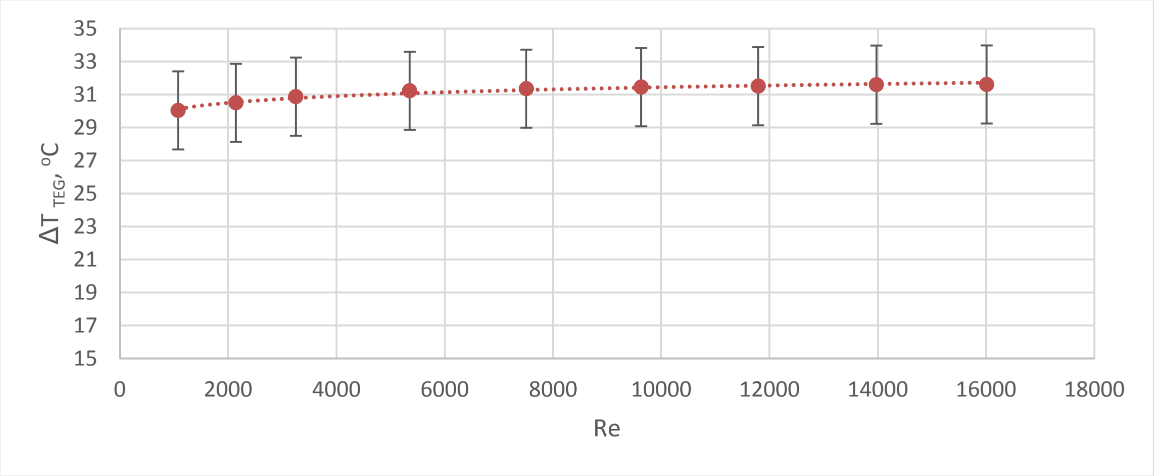

Figure 62 - Effect of changing flow rate on ΔT TEG

6.6.2 Changing chilled water temperature

In a constant mass flow rate experiment, chilled water temperature was changed to monitor its effect on the test section. It has been observed that as T water- average decreases, cold side of the TEG module temperature decreases. Therefore, the temperature difference across the TEG module increases. However, changing the average water temperature by 8 degrees has only changed the cold side temperature by less than two degrees as observed in Figure 63 (TEG-V-410-48-130-A+25 at $T_{TEG-HOT}$ of 98°C to 98°C) . The change water temperature gets distributed over the test section including the stainless steel cylindrical blocks conduction resistance, TEG module conduction resistance, TEG module cold side contact resistance, pipe conduction resistance and water convective resistance.

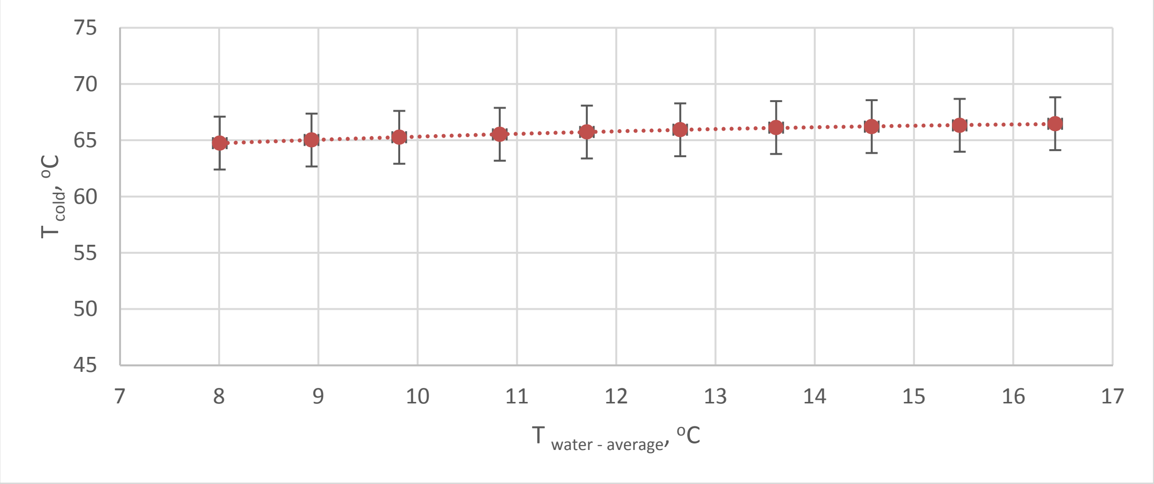

Figure 63 – Effect of changing chilled water temperature on cold side temperature of TEG-V-410-48-130-A+25

6.7 Summary

Performance measured for the prototype manufactured just after reducing oxides (TEG-V-390-48-130-OR) reached an effective Seebeck coefficient of 190 μV/K compared to a Seebeck coefficient of 145 μV/K measured by Min & Rowe (2007) for their prototype as plotted in Figure 64. Min & Rowe provided one measurement of theoretical and effective Seebeck coefficient for their module, therefore their data are shown as a straight line. Tested prototype effective Seebeck coefficient change with average temperature of the TEG module. Plotted in the graph as well is the theoretical value calculated from material properties (maximum achievable). Figure 65 shows the fabrication process performed to produce the prototype. The developed process is to be considered as the base line in the next phase of the project. Each parameter will be tested using different values and optimized. Parameters to be optimized are (but not limited to), geometry dimensions, masses, oxide reduction hold time, sintering temperature and pressing pressure.

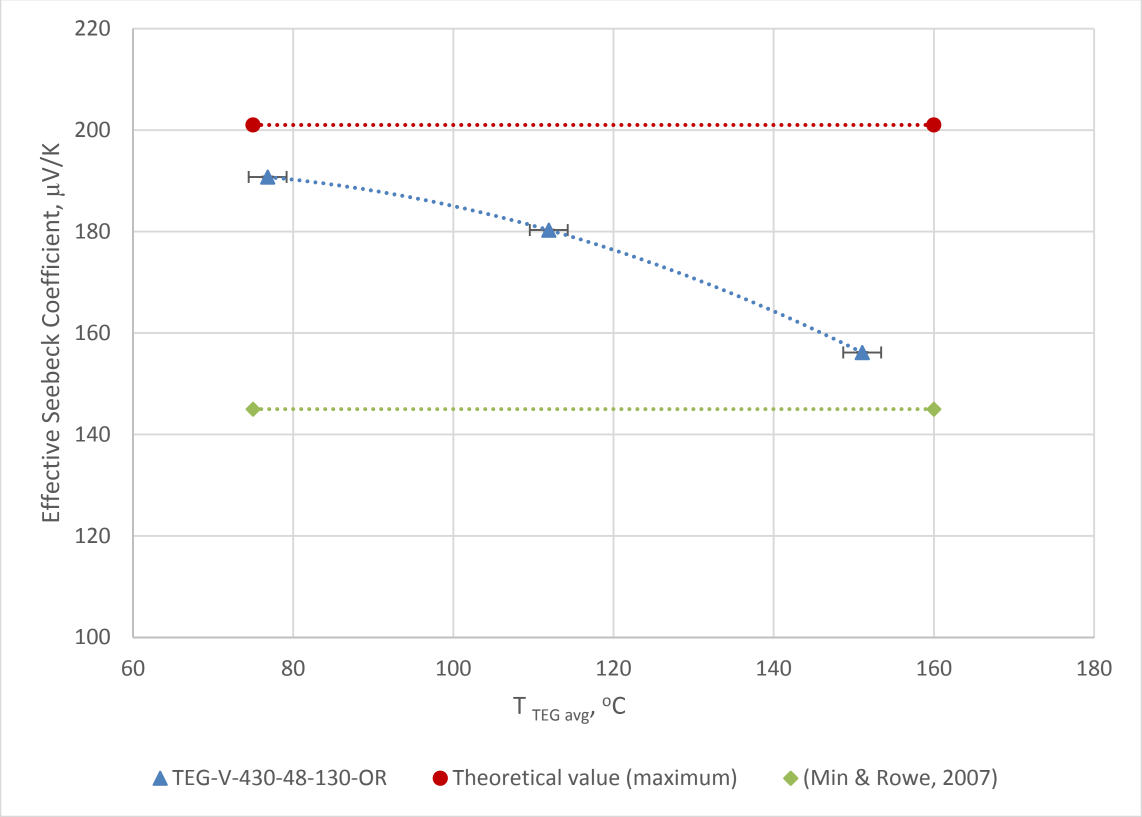

Figure 64 – Comparison of effective Seebeck coefficient for proposed V-shaped prototype vs (Min & Rowe, 2007)

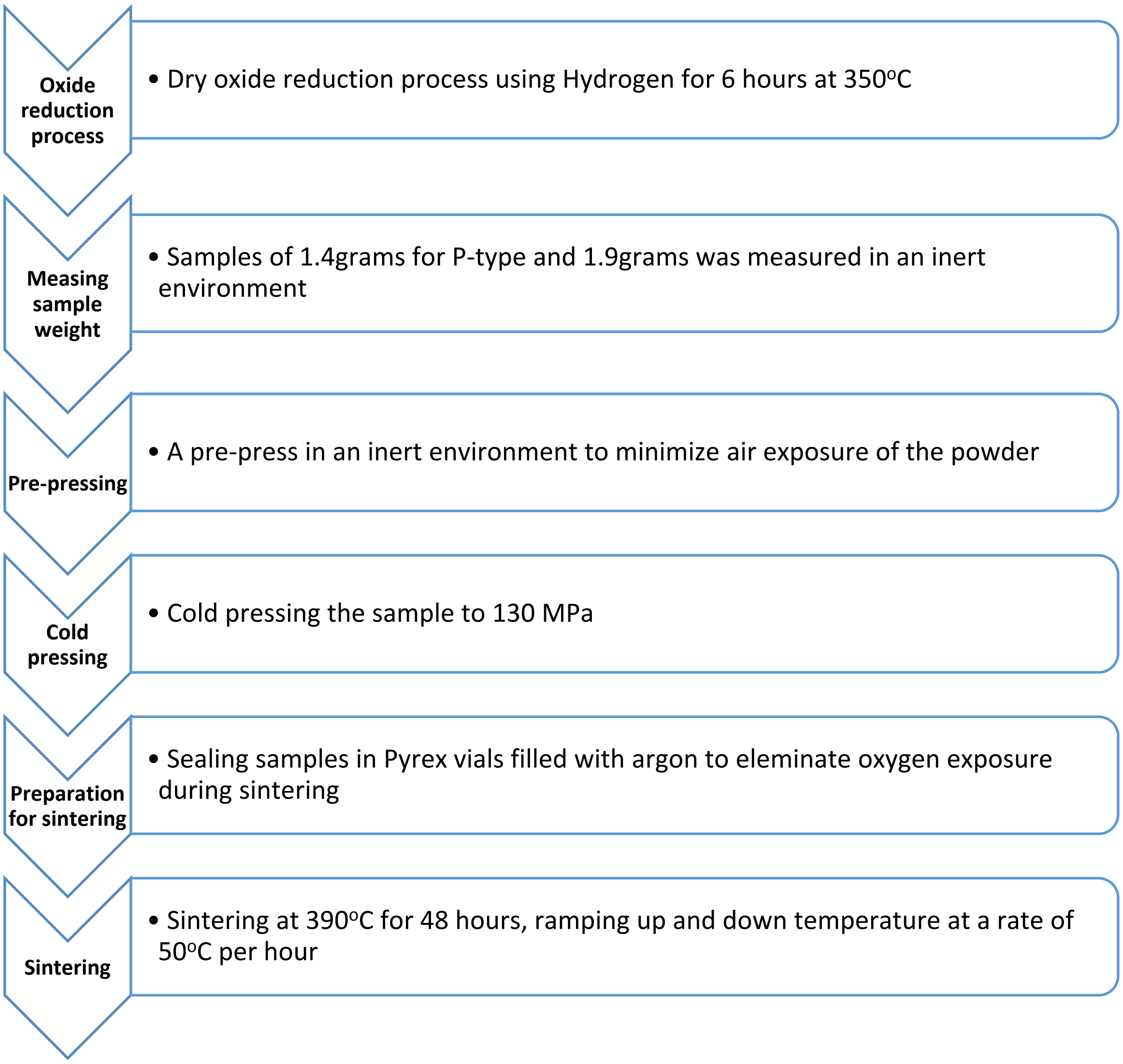
Oxide reduction process

- Dry oxide reduction process using Hydrogen for 6 hours at 350^{o}C

Measing sample weight

- Samples of 1.4grams for P-type and 1.9grams was measured in an inert environment

Pre-pressing

- A pre-press in an inert environment to minimize air exposure of the powder

Cold pressing

- Cold pressing the sample to 130 MPa

Preparation for sintering

- Sealing samples in Pyrex vials filled with argon to eleminate oxygen exposure during sintering

Sintering

- Sintering at 390^{o}C for 48 hours, ramping up and down temperature at a rate of 50^{o}C per hour

Figure 65 - Prototype fabrication process

Chapter Seven: Modeling and Simulation

7. Modeling and Simulation

To study TEG geometries further, an ANSYS Workbench® model was created to compare annular TEG modules. (Min & Rowe, 2007) ring-structured design and the proposed V-shaped design were modeled under similar conditions for comparison. This numerical study aimed to understand the reason behind the improvement in performance that was observed in experimental testing for the V-shaped design over the ring-structured design.

7.1 Geometry Design

A model was created with a boundary condition of a constant heat flux source or a constant temperature on the outside as the hot side and a constant heat transfer coefficient and water temperature on the cold side. Two geometries were modeled and compared. First geometry was a ring-structured module similar to the one created by Min & Rowe (2007). Second geometry was the proposed V-shaped design.

Min & Rowe (2007) proposed a design that would be the base of a tube shaped thermoelectric module that consists of a large number of coaxial rings. The design consists of ring-structured modules arranged with alternating P & N elements. Between thermoelectric rings, a copper washer acted as the conductor on the inner or the outer edge alternately creating hot and cold junctions as shown in Figure 66. The dimensions were an inner radius of 8.03mm, an outer radius of 12.7mm and an average thickness of 3.40mm for thermoelectric rings. Copper conductors rings in between had an inner diameter of 11.18mm, an outer diameter of 12.7mm for the outer copper ring- and an inner diameter of 8.03mm, an inner diameter of 9.55mm for the inner copper ring. Thickness for both copper rings was 0.76mm.

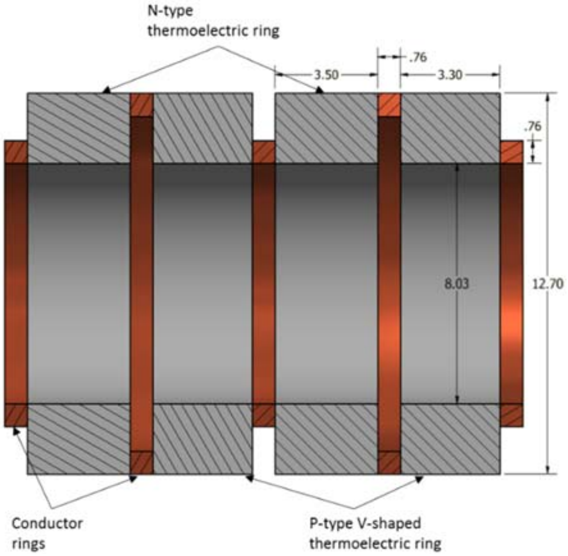

Figure 66 – Ring-structured TEG module design, dimensions in mm

The geometry of the V-shaped design for the p-type ring geometry is presented in Figure 67. The proposed design arranges V-shaped p-type and ring-structured n-type thermoelectric elements to be alternately. Similar to Min and Rowe, copper washers were used as conductors on the inner or the outer edge creating hot and cold junctions.

The N-type ring was constructed with an inner radius of 8.03mm, an outer radius of 12.7mm and a thickness of 3.50mm. V-shaped P-rings were made with the same inner diameter, outer diameter, edge thickness and therefore same volume as the ring-structured design for fair comparison. P-type V-shaped ring was constructed with an inner radius of 8.03mm, an outer radius of 12.7mm and an edge thickness of 3.30mm and a total thickness of 3.50mm. Copper conductors rings in between had an inner diameter of 11.18mm, an outer diameter of 12.7mm for the outer copper ring- and an inner diameter of 8.03mm, an inner diameter of 9.55mm for the inner copper ring. Thickness for both copper rings was 0.76mm.

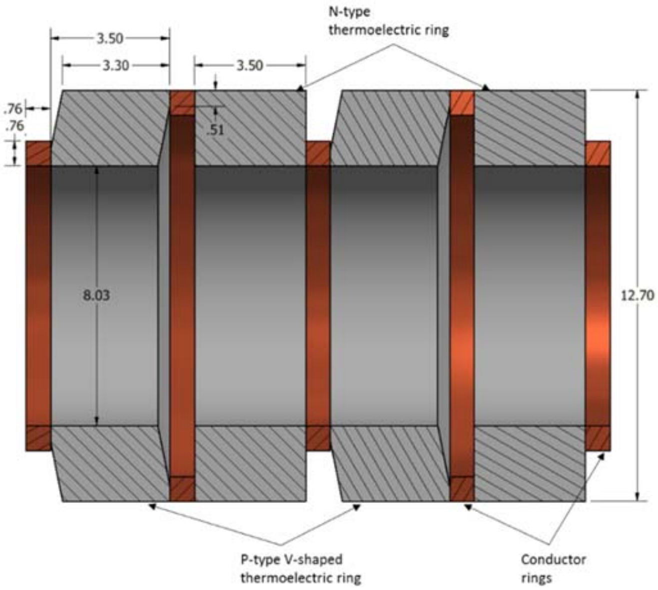

Figure 67 – Proposed V-shaped TEG module design, dimensions in mm

7.2 Modeling

Exploring two different annular thermoelectric geometries, an ANSYS Workbench® model was created to study the thermal and electrical behaviour. Two TEG modules with deferent geometries were modeled under similar boundary conditions for a fair comparison. Same parameters were measured in each model and compared.

To simulate the hot side, a 121.41 mm diameter stainless steel cylindrical hollow block is wrapping the outer surface of the TEG module (Figure 68) to allow equally distributed heat flow to the module, lower end effects and create a uniform heat source that can work for each TEG module without giving any of them an advantage.

To simulate the cold side, a chilled water pipe was introduce on the inside of the TEG module to act as a heat sink. A boundary condition of a constant convective heat coefficient and water temperature was imposed on the inner surface of the pipe. A contact resistance between the cold side of the TEG module and the outer surface of the pipe was incorporated in the model as an insulation layer (simulating an air gap).

To compare between TEG modules, two different scenarios were imposed on the model. The first one was a constant convective heat coefficient and water temperature boundary condition on the inside surface of the pipe (simulating water flow) and a constant heat flow on the outside surface of the stainless steel cylindrical block.

Second scenario is a constant temperature boundary condition imposed on the outer surface of the stainless steel block and a constant convective heat coefficient and water temperature boundary condition on the inside surface of the pipe (simulating water flow). These conditions was imposed on the module to study heat flow pattern, temperature gradient and electrical performance.

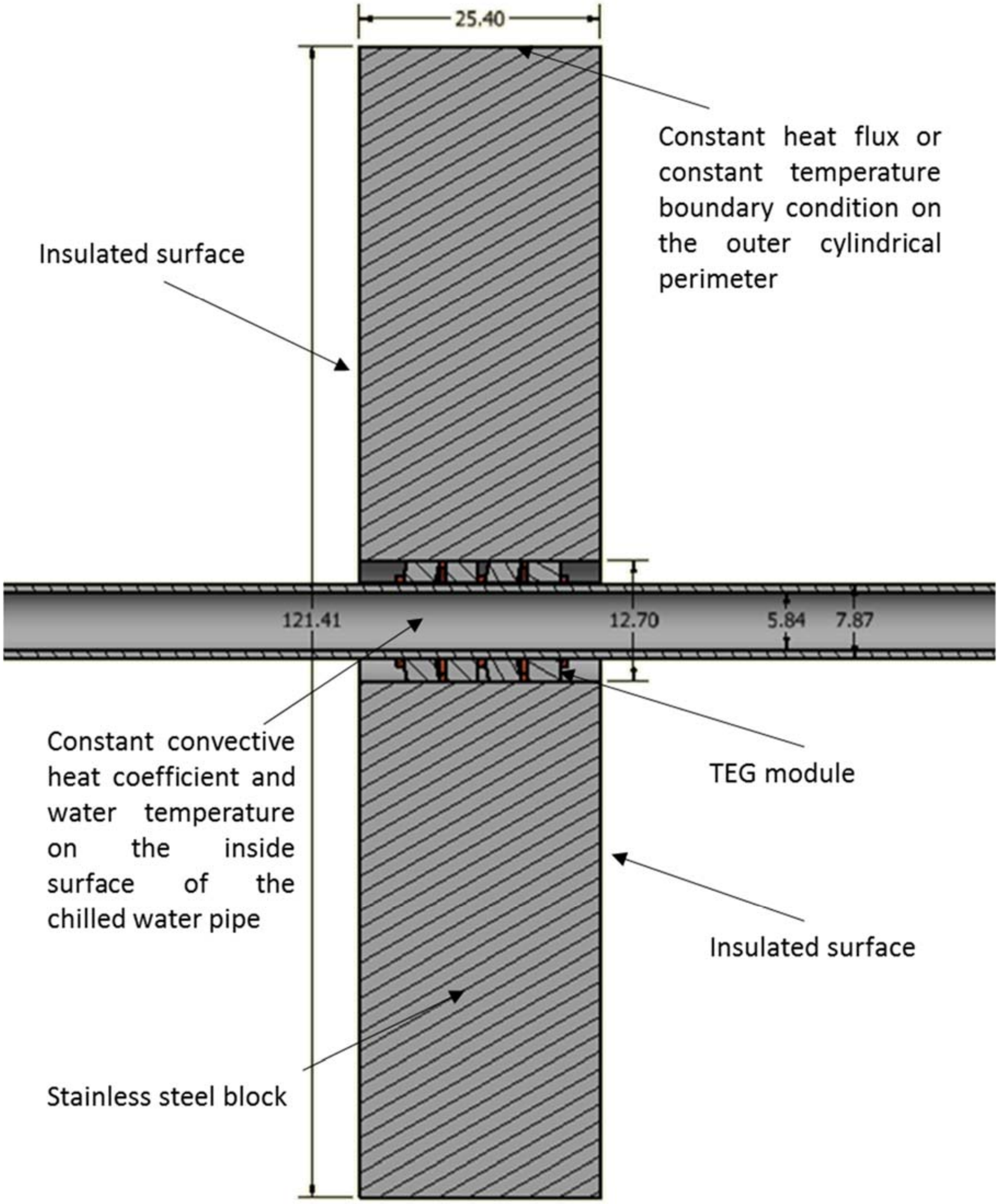

Figure 68 - Modeling arrangement with a stainless steel block for the hot side and chilled water pipe for the cold side, dimensions in mm

Material properties for each component are presented in Table 12. The hot block cylinder acting as the heat source was chosen to be stainless steel to allow temperature variations on the hot side of the TEG module to allow modules with larger hot side surface area to perform better. The chilled water pipe was chosen to be aluminum to minimize radial heat flow resistance between chilled water and the TEG module.

Component	Material	Key properties	Value	Reference
Thermoelectric ring	Bismuth telluride	Thermal conductivity	1.36 $Wm^{-1}K^{-1}$	(Keshavarz Khorasgani, 2014)
		Seebeck coefficient	201 μVK^{-1}	(Min & Rowe, 2007)
		Electric resistivity	1.09 E-05 ohm m	
Conductor ring	Copper	Thermal conductivity	401 to 379 $Wm^{-1}K^{-1}$	(Callister & Rethwisch, 2007; Çengel et al., 2008; Douglas, 1989)
		Seebeck coefficient	1.5 E-06 VK^{-1}	
		Electric resistivity	1.7 E-08 to 5.19 E-08 ohm.m	
Hot Block cylinder	Stainless steel	Thermal conductivity	15 to 17 $Wm^{-1}K^{-1}$	
Chilled water pipe	Aluminum	Thermal conductivity	144 to 175 $Wm^{-1}K^{-1}$	
Insulation layer	-estimated value-	Thermal conductivity	0.08 $Wm^{-1}K^{-1}$	-

Table 12 - Material properties of different components

Grid was uniform throughout the whole domain, and it was denser in the regions where there is expected higher gradient as at the internal chilled water pipe surface with inflation of growth rate of 1.2. Grid independence analysis was done and is shown in Figure 69. Resultant open circuit voltage was found to converge using around 1,500,000 grid elements. Resultant open circuit voltage was found to change by only 0.03% at 2,560,000 grid elements relative to 2,000,000 grid elements. Therefore, simulation in this chapter were performed using over 2,000,000 grid and 3,477,142 nodes for the sake of computational efficiency.

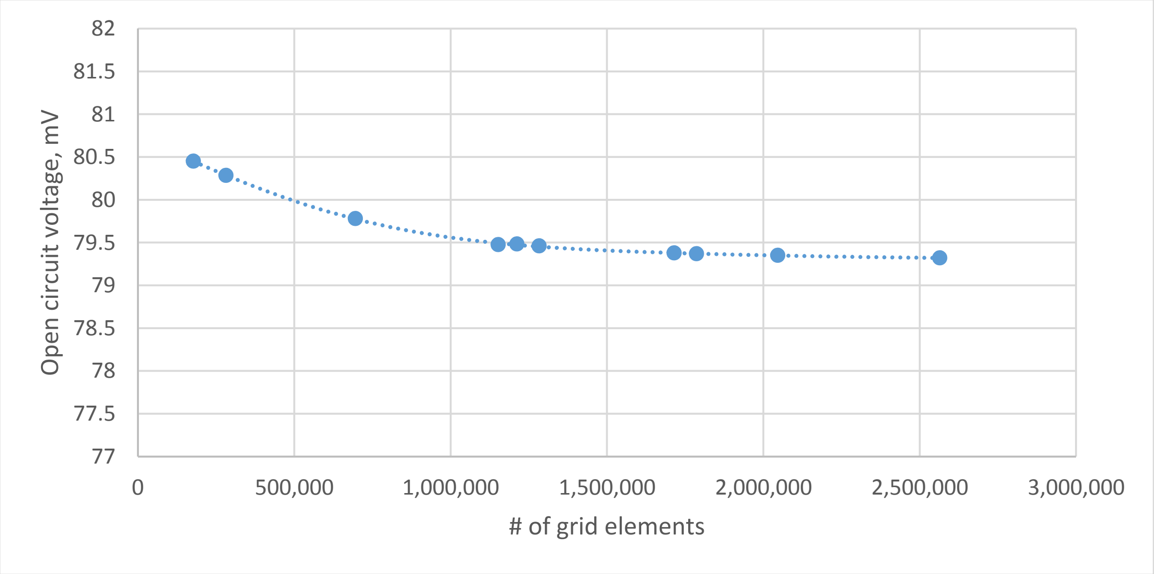

Figure 69 – Number of grid elements plotted vs resultant open circuit voltage

The numerical model studies both electrical and thermal behaviour of the TEG module. To assess the electrical performance, a voltage probe was used on one end of the TEG module while the other end is grounded. Open circuit voltage measurement between end copper rings shows both the Seebeck coefficient for the material and heat flow pattern through the module. Heat passage through the material is what cause it to produce electricity. Therefore, heat flux and temperature gradient patterns were compared to explain the electrical performance. More details concerning the simulation model are available in Appendix D.

7.3 Simulation results

Figure 70 shows simulation result for a sectional view temperature distribution under a hot side constant temperature condition.

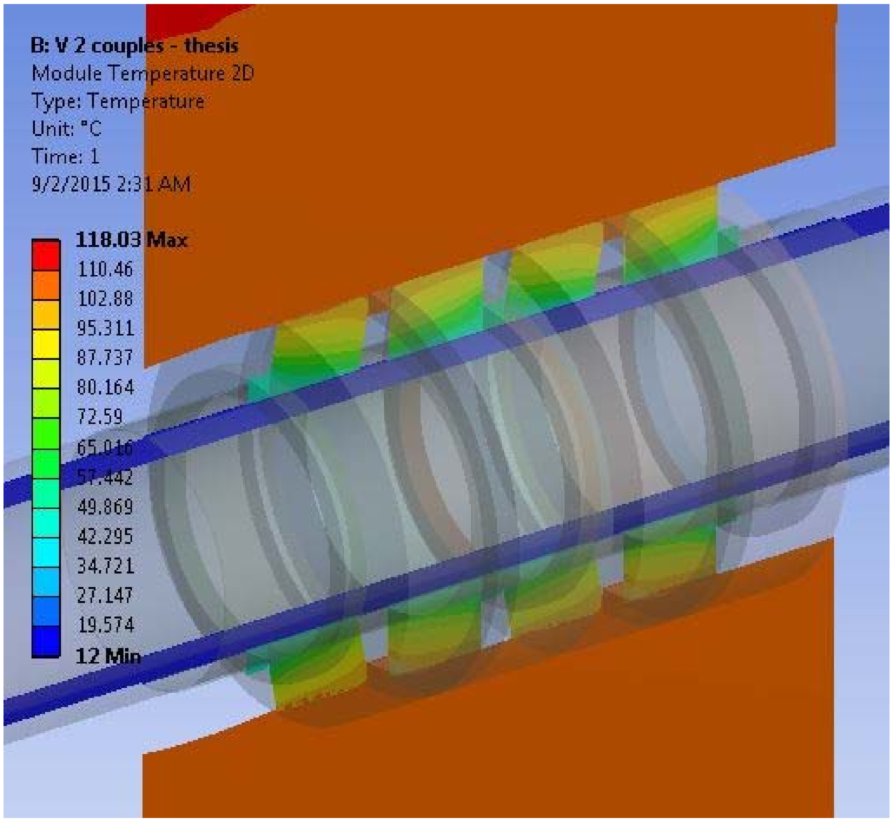

Figure 70 - Simulation result showing a sectional view of a 3-D temperature distribution model

7.3.1 Constant Heat Boundary Condition

A constant heat flow of 15 W was exerted on the outer side of the stainless steel block. On the inner surface of the pipe, a convection boundary condition was imposed to simulate a chilled water flow. Convection heat transfer coefficient was set to 10,000 W/(m^2K), estimating a chilled water flow of about 4.8 Kg/min. Water temperature was set to be constant at 12^{o}C.

7.3.1.1 Temperature Distribution

The simulation was performed under a constant heat transfer boundary condition for both models, ring-structured and V-shaped TEG modules. Temperature distribution across the model was calculated including the hot side stainless steel block and the chilled water pipe. A sectional view in the 3D model was taken to show temperature gradient across different components. Figure 70 shows temperature distribution over V-shaped TEG module and other model components under a constant heat flow boundary condition.

Figure 71 and Figure 72 show temperature gradient with the module under a 15 kW heat flow for the ring-structured and V-shaped TEG modules respectively. Temperature gradient for the ring-structured TEG module shows areas of constant temperatures around conductor rings. That changed the direction of the temperature gradient to be more between the conductor rings rather than between the thermoelectric ring extrados and intrados. This gradient agrees with our earlier hypothesis that heat would be flowing diagonally between the inner edges of the conductor rings, therefore not flowing through a portion of the thermoelectric material. In the V-shaped TEG module, an improved behaviour can be observed where the gradient is perpendicular to the thermoelectric ring sides.

The higher the temperature difference achieved across the module, the higher voltage produced, therefore the more power produced from the same thermoelectric ring. Under a constant heat flow boundary condition, differential temperatures of 57.14^{o}C and 62.19^{o}C were achieved across the TEG module for ring-structured and V-shaped designs respectively. A 9% improvement was achieved moving from a ring-structured design to a V-shaped design.

The hot side temperature of the TEG module was 103.60^{o}C and 105.17^{o}C, cold side temperature was 46.46^{o}C and 42.98^{o}C for the ring-structured and V-shaped designs respectively. Comparing the ring-structured and V-shaped confirms the before noticed improvement for V-shaped over ring-structured modules within the same temperature range.

For 100% of the heat to flow through the thermoelectric material, heat should flow radially between the thermoelectric ring extrados and intrados for the ring-structured and V-shaped designs. Directional heat flux in the axial direction near the conductor ring edge was observed in the ring-structured design. That indicates that portion of the heat flows to the conductor ring at this location and does not go through the rest of the material, i.e. lower material utilization in electric power production.

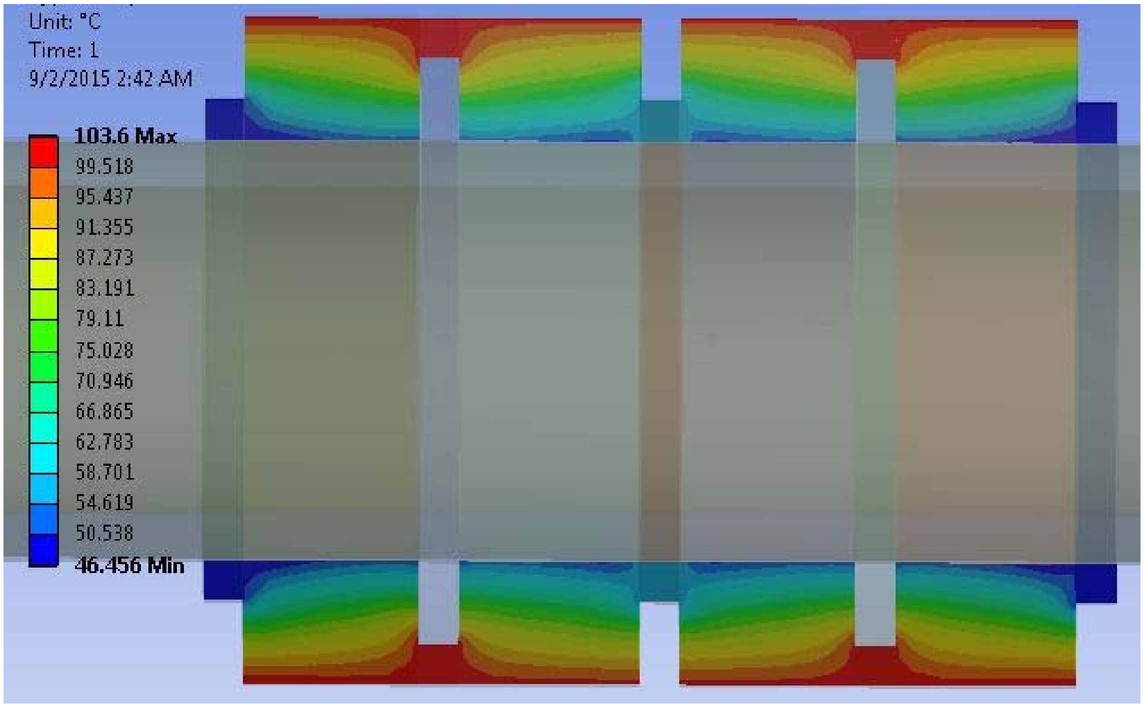

Figure 71- Temperature gradient across ring-structured TEG module under constant heat flow condition

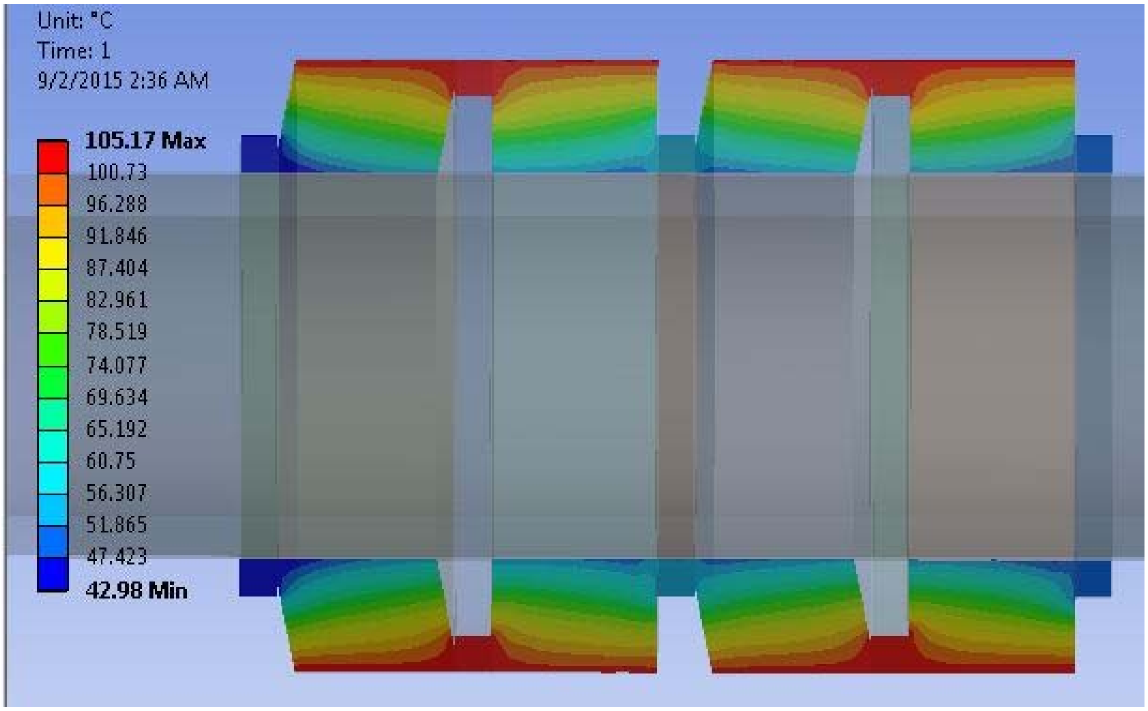

Figure 72 - Temperature gradient across V-shaped TEG module under constant heat flow condition

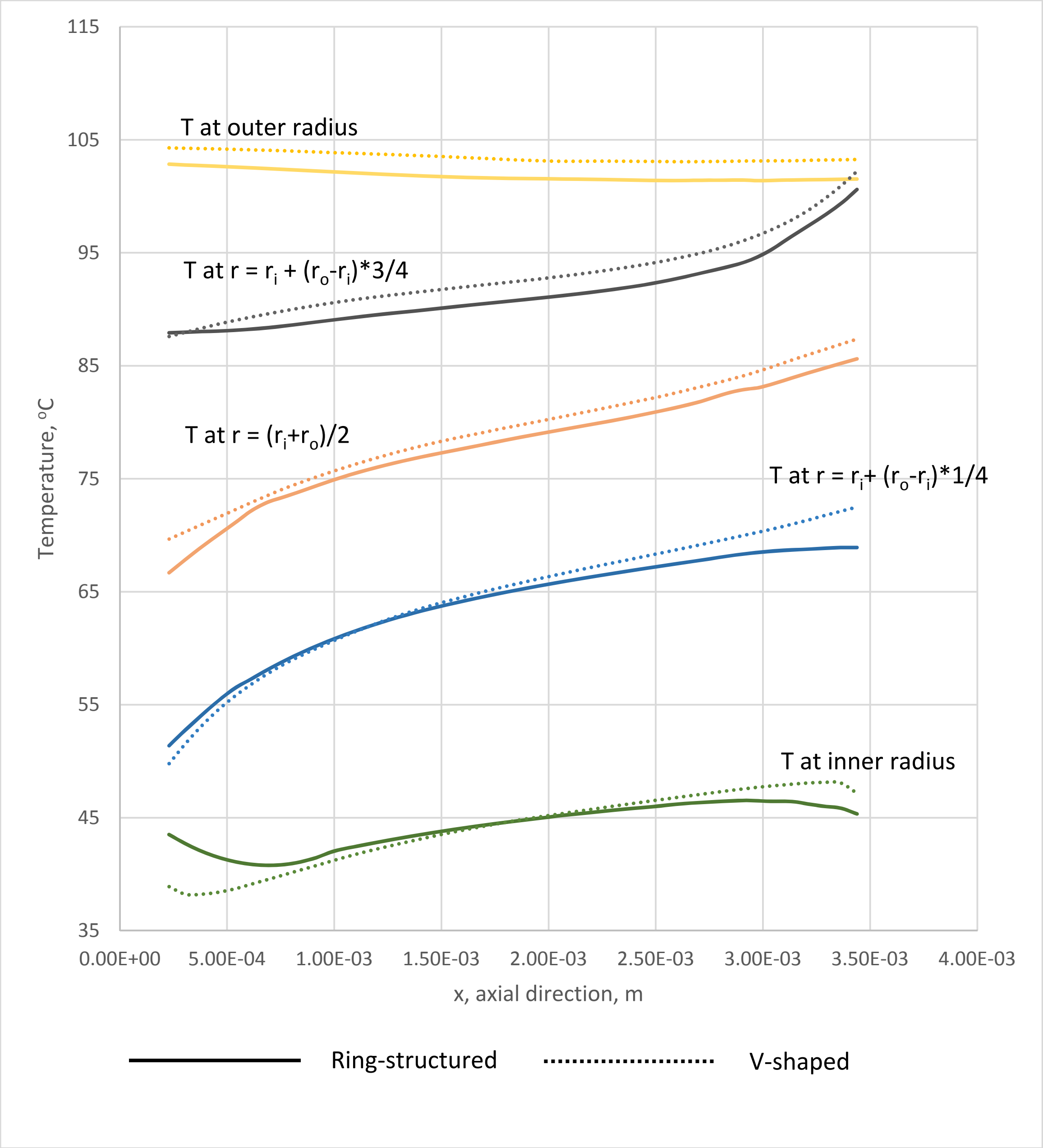

Figure 73 - Temperature profiles in the axial direction from modeling at a constant heat flux boundary condition for ring-structured vs V-shaped designs

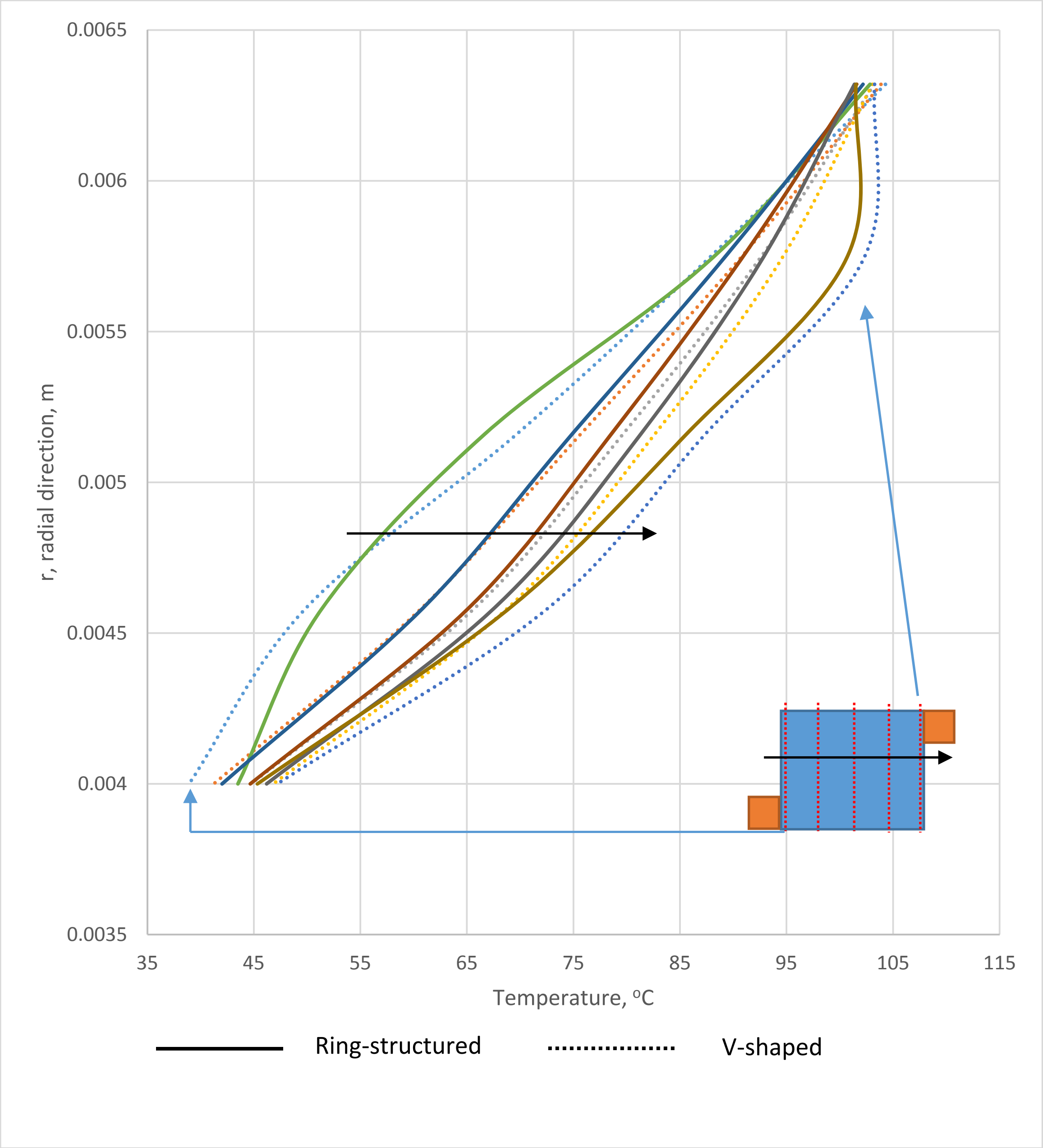

Figure 74 - Temperature profiles in the radial direction from modeling at a constant heat flux boundary condition for ring-structured vs V-shaped designs

Plotted in Figure 73 are temperature profiles at different radiuses for both ring-structured and V-shaped models and plotted in Figure 74 are temperature profiles at different axial values. For the ring-structured design, smaller temperature gradient can be observed near contact areas with metal conductor rings. X value (axial direction) for V-shaped design has been corrected to allow comparison with the ring-structured design at the equivalent location.

7.3.1.2 Open Circuit Voltage

A voltage probe on one end of the TEG module was used while the other end is grounded. Open circuit voltage was measured in the simulation to compare the electrical performance of different modules. Electrical performance is dependent on the thermal behaviour, therefore electrical results can be roughly forecasted from earlier temperature gradient and material utilization behaviour. Open circuit voltage under a constant heat flow of 15W across the module measured 37.71 mV and 40.92mV for the ring-structured and V-shaped designs respectively.

V-shaped TEG module outperformed the ring-structured design similar to (Min & Rowe, 2007) design by 9%. Performance improvement was found consistent with differential temperature and heat flow pattern behaviour for both designs.

7.3.2 Constant Temperature Boundary Condition

A constant hot side temperature of 125^{o}C was imposed on the outer side of the stainless steel block. On the inner surface of the pipe, a convection boundary condition was imposed to simulate a chilled water flow. Convection heat transfer coefficient was set to 10,000 W/(m^{2}K), estimating a chilled water flow of about 4.8 Kg/min. Water temperature was set to be constant at 12^{o}C.

7.3.2.1 Temperature Distribution

Figure 75 and Figure 76 show temperature gradient for ring-structured and V-shaped TEG module respectively. Temperature gradient for the ring-structured TEG module shows areas of constant temperatures around conductor rings. That changed the direction of the temperature gradient to be more between the conductor rings rather than between the thermoelectric ring extrados and intrados. This gradient agrees with earlier hypothesis that heat would be flowing diagonally between the inner edges of the conductor rings, therefore not flowing through a portion of the thermoelectric material. In the V-shaped TEG module, an improved behaviour can be observed where the gradient is perpendicular to the thermoelectric ring sides.

The higher the temperature difference achieved across the module, the higher voltage produced, therefore the more power produced from the same thermoelectric ring. Under a constant hot side temperature boundary condition, differential temperatures of 61.88^{o}C and 66.31^{o}C were achieved across the TEG module for ring-structured and V-shaped designs. A 7% improvement was achieved moving from a ring-structured to a V-shaped design.

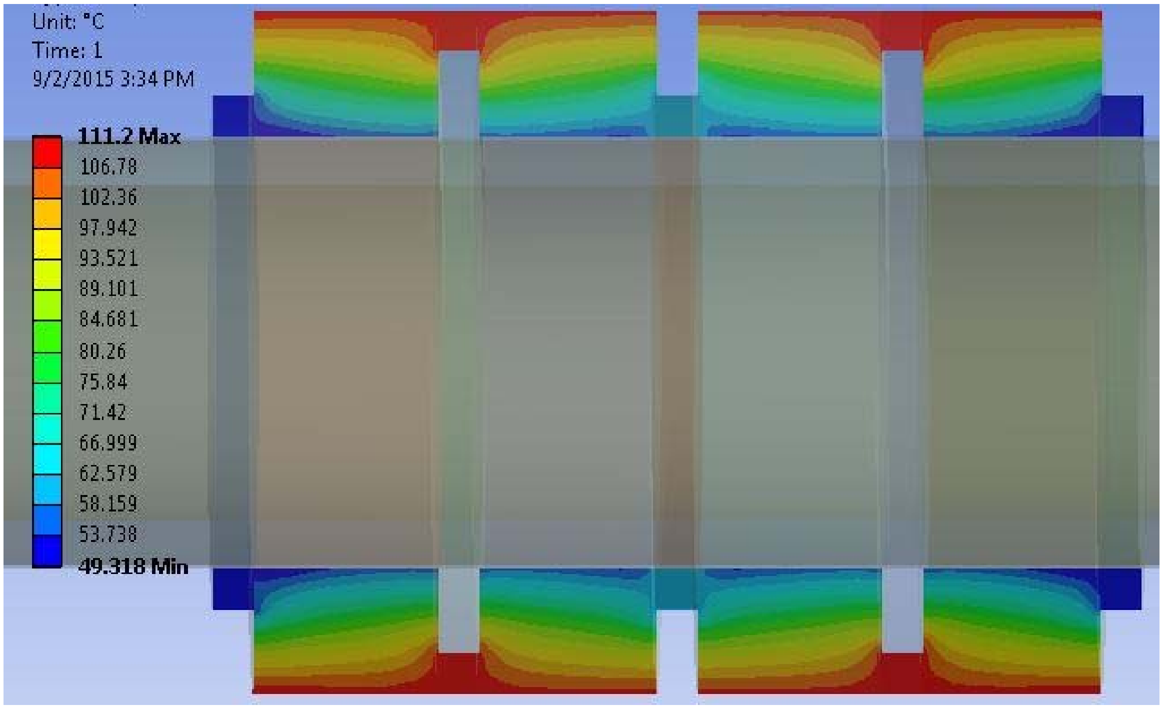

Figure 75 - Temperature gradient across ring-structured TEG module under constant hot side temperature condition

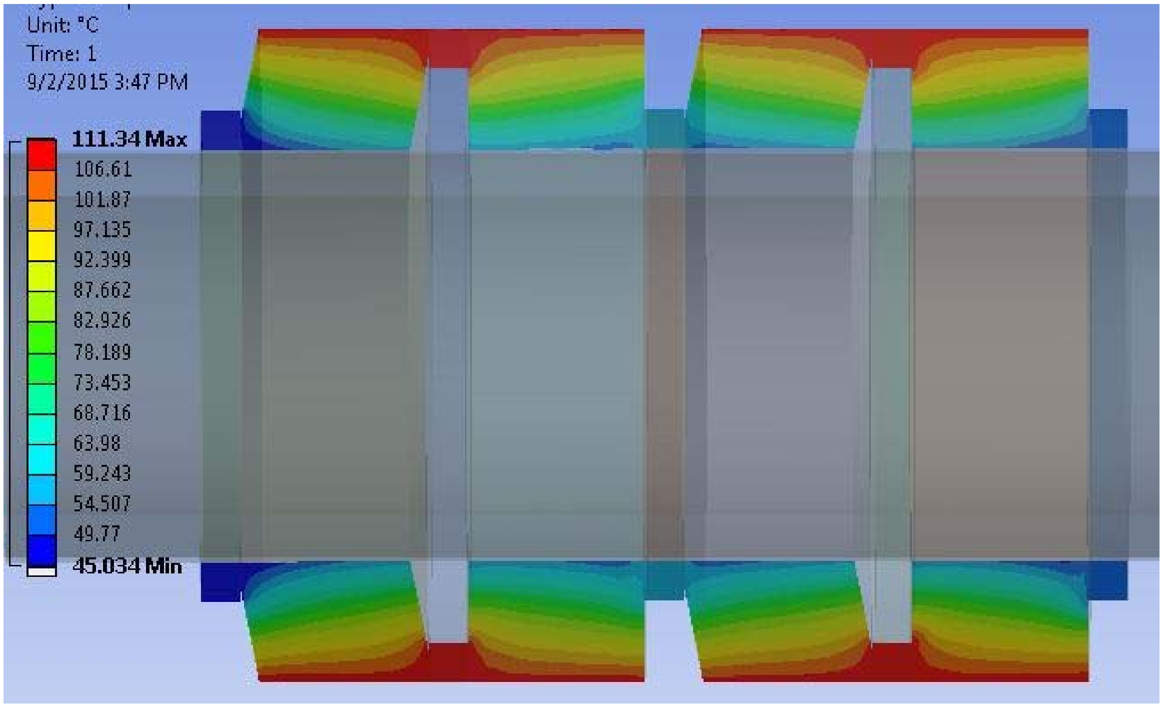

Figure 76 - Temperature gradient across V-shaped TEG module under constant hot side temperature condition

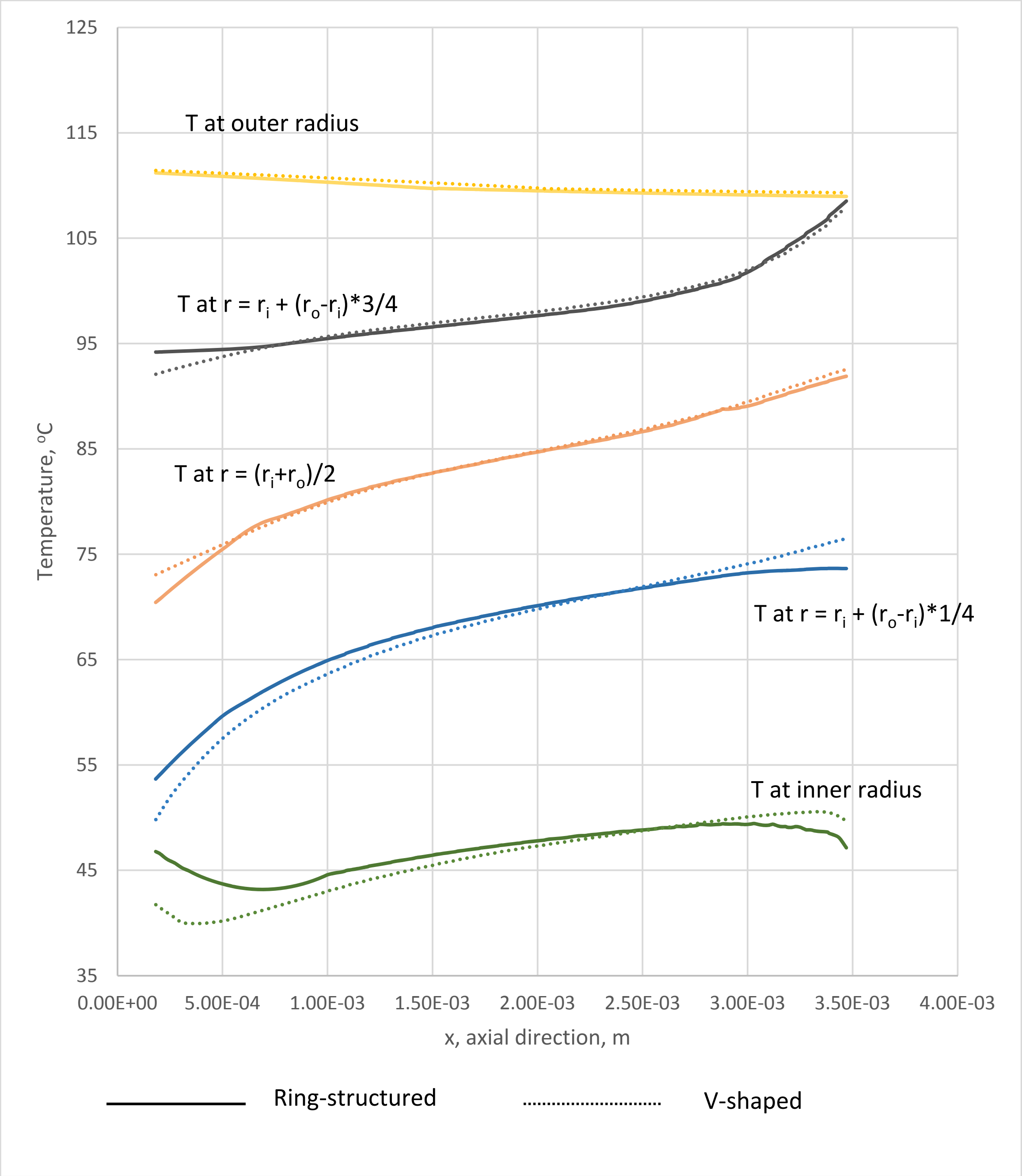

Figure 77- Temperature profiles in the axial direction from modeling at a constant temperature boundary condition for ring-structured vs V-shaped designs

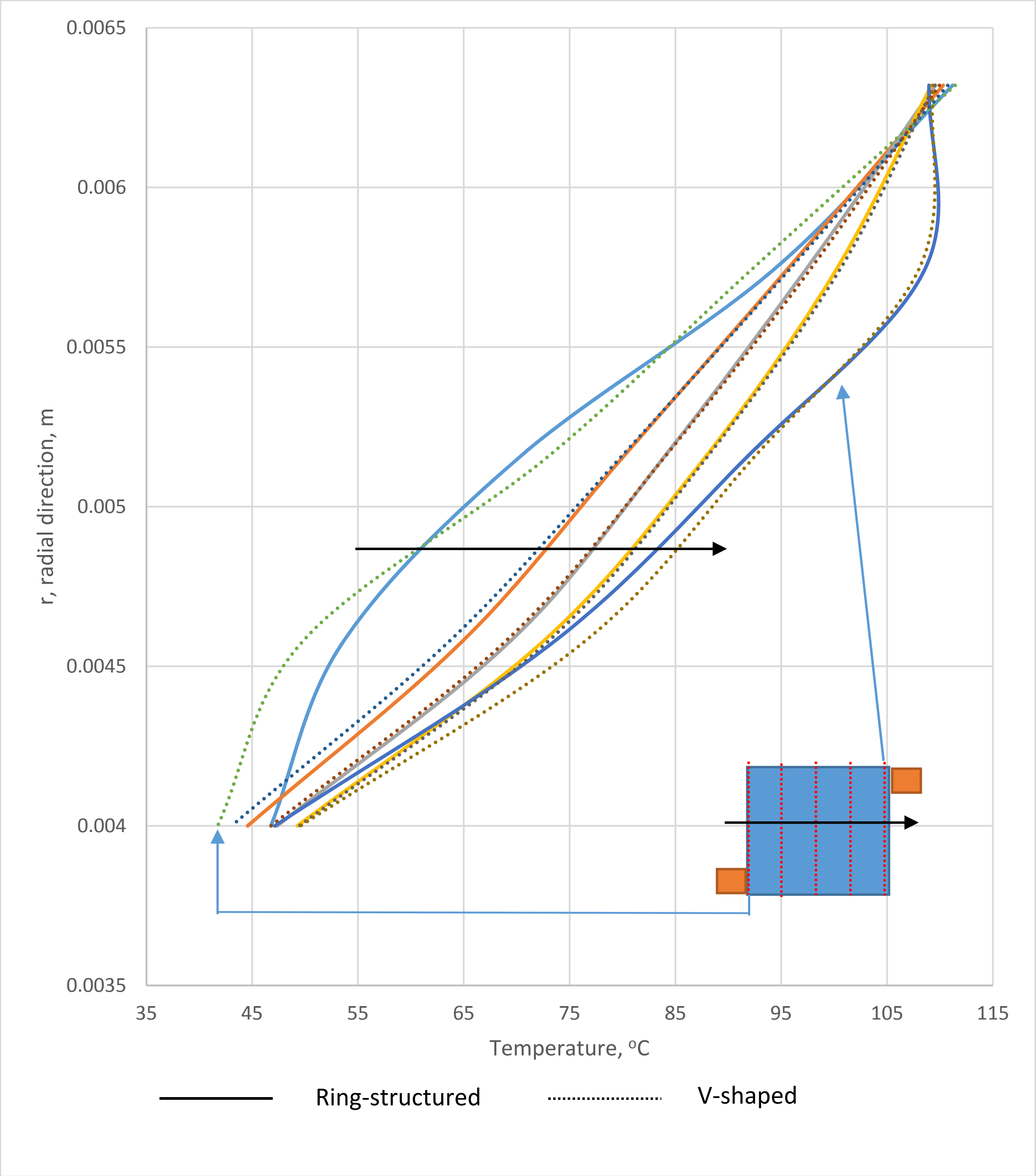

Figure 78 - Temperature profiles in the radial direction from modeling at a constant temperature boundary condition for ring-structured vs V-shaped designs

Plotted in Figure 77 are temperature profiles at different radiuses for both ring-structured and V-shaped models and plotted in Figure 78 are temperature profiles at different axial values. For the ring-structured design, smaller temperature gradient can be observed near contact areas with metal conductor rings. X value (axial direction) for V-shaped design has been corrected to allow comparison with the ring-structured design at the equivalent location.

The cold side temperature was found to be 49.32ºC and 45.034ºC for the ring-structured and the V-shaped respectively. Comparing the ring-structured and V-shaped confirms the before noticed improvement for V-shaped over ring-structured design within the same temperature range.

The heat flow through the module showed 16.25W and 16.00W flowing through ring-structured and V-shaped TEG modules respectively. V-shaped module design has a higher heat resistance, therefore creating a higher differential temperature across the module and allowing less heat to flow.

7.3.2.2 Open Circuit Voltage

A voltage probe on one end of the TEG module was used while the other end is grounded. Open circuit voltage was measured in the simulation to compare the electrical performance of different modules. Electrical performance is dependent on the thermal behaviour, therefore electrical results can be roughly forecasted from earlier temperature gradients and material utilization behaviour. Open circuit voltage under a constant hot side temperature of 125ºC imposed on the outer surface of the stainless steel block measured 40.09 mV and 43.63mV for the ring-structured and V-shaped TEG modules.

To conclude, V-shaped TEG module outperformed the ring-structured design similar to (Min & Rowe, 2007) design by 7% although less heat is flowing through it (higher efficiency). Performance improvement was found consistent with differential temperature and heat flow pattern behaviour for both designs.

7.3.3 Conceptual V-shaped with a Thin Conductor Ring

The conductor ring was found responsible for creating a region with a lower temperature gradient in the thermoelectric ring, therefore the thermoelectric material in this region is not contributing to the electric voltage produced. Reducing the contact area with the conductor ring in the V-shaped design caused the thermal gradient and thermoelectric performance to improve. Another approach is to reduce the conductor ring in size or eliminate it. Such concept needs to be investigated experimentally to validate the effect of the conductor material volume relative to the thermoelectric material volume. Figure 79 shows the proposed V-shaped design with a 0.25mm thickness conductor ring.

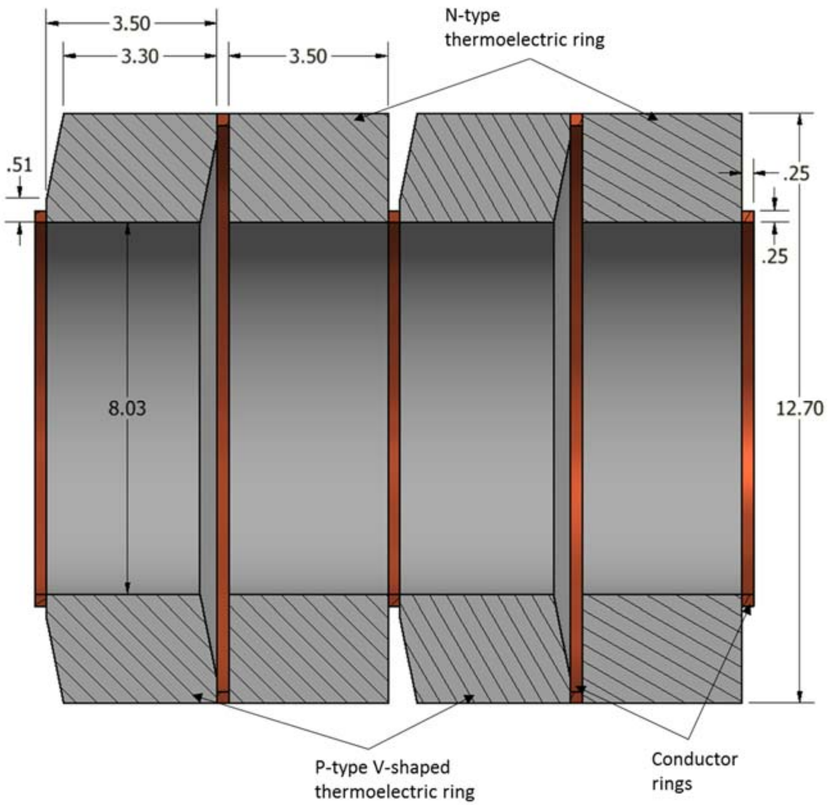

Figure 79- Proposed V-shaped with a thin conductor ring TEG module design, dimensions in mm

Under a constant heat flow boundary condition, differential temperatures of 57.14°C, 62.19°C and 65.7°C were achieved across the TEG module for ring-structured, V-shaped and V-shaped with a thin conductor ring designs respectively. A 15% increase in differential temperature was achieved moving from a ring-structured design to a V-shaped with a thin conductor ring design as shown in Figure 80.

The hot side temperature of the TEG module was 103.60°C, 105.17°C and 114.07°C, cold side temperature was 46.46°C, 42.98°C and 48.37°C for ring-structured, V-shaped and V-shaped with a thin conductor ring designs respectively. Comparing the ring-structured and V-shaped confirms the before noticed improvement for V-shaped over ring-structured modules within the same temperature range.

A voltage probe on one end of the TEG module was used while the other end is grounded. Open circuit voltage was measured in the simulation to compare the electrical performance of different modules. Open circuit voltage under a constant heat flow of 15W across the module measured 37.71 mV, 40.92mV and 43.31mV for ring-structured, V-shaped and V-shaped with a thin conductor ring designs respectively. A 15% improvement in open circuit voltage was achieved moving from a ring-structured design to a V-shaped with a thin conductor ring design.

A 250μm thickness conductor ring can be placed on the thermoelectric leg by sputtering. Further experimental investigation will be done to verify the conductor volume needed in the TEG module relative to the thermoelectric ring volume.

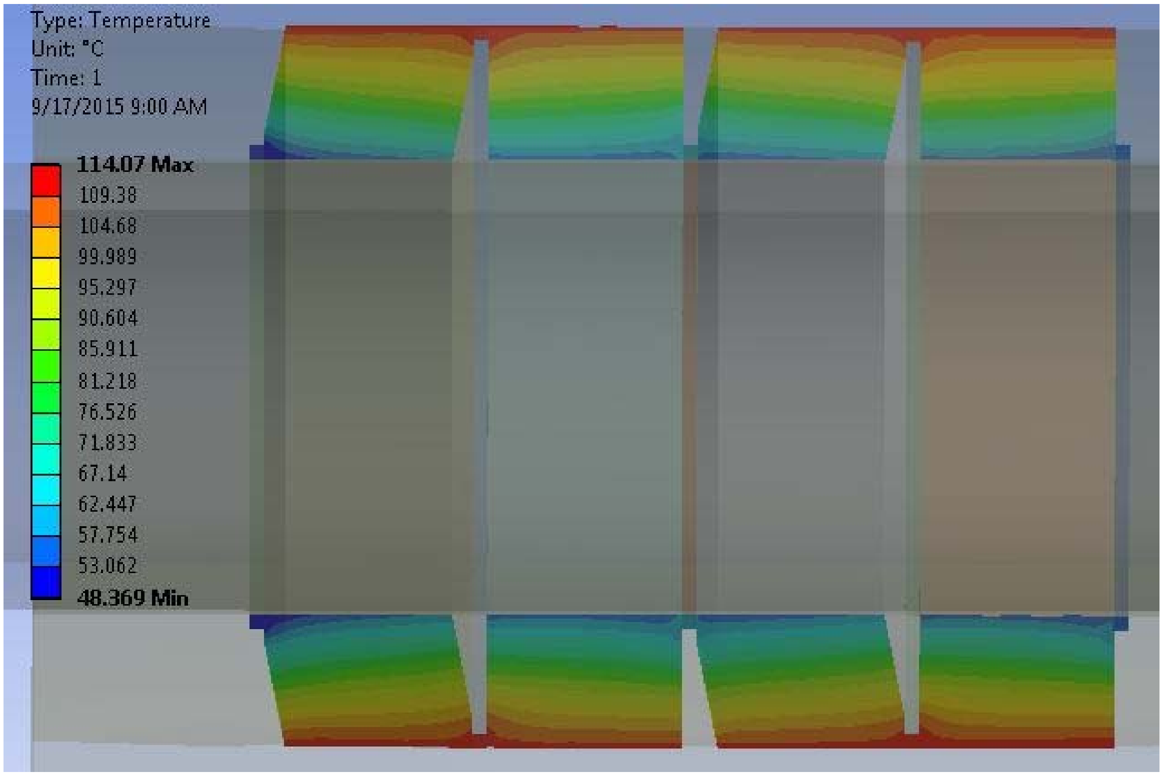

Figure 80 - Temperature gradient across V-shaped with a thin conductor ring TEG module under constant heat flow condition

7.4 Summary

A numerical simulation model was created to compare electrical and thermal behaviour for different TEG module geometries and identify the main mechanism for the performance gain in experimental results for V-shaped TEG module design to ring-structured TEG design. ANSYS Workbench® simulation results show that V-shaped TEG module electrically outperforms the ring-structured design by 7% to 9% for a constant temperature and a constant heat flux boundary conditions respectively. Performance improvement was found consistent with temperature gradients and heat flow path pattern behaviour for both designs.

Improvement in the effective Seebeck coefficient observed is much higher in experimental results moving from the ring-structured to V-shaped designs than numerical results. Experimentally, prototypes fabricated for geometry comparison used an oxidized powder, therefore improvement percentage is not reliable. The trend of improvement comparing both prototypes is trusted as both were fabricated from the same powder.

Chapter Eight: Conclusion and Future Recommendations

8. Conclusion and Future Recommendations

The process to fabricate a proposed annular thermoelectric generator design using powder methodology was developed. Effective Seebeck coefficient and thermal performance for prototypes were experimentally characterized. After developing key manufacturing parameters, V-shaped design prototype was tested and compared against the ring-structured prototype. Performance measured for the V-shaped prototype reached a Seebeck coefficient of 190.75 μV/K compared to a Seebeck coefficient of 145 μV/K measured by Min & Rowe (2007) for their ring-structured prototype and a theoretical Seebeck coefficient of 201 μV/K.

8.1 Design, Manufacturing and Results

A novel V-shaped design for the p-type ring geometry has been proposed to improve heat path inside the ring which would utilize more of the material into power production making the geometry more efficient than the ring-structured module produced by (Min & Rowe, 2007). Numerical simulations preformed to compare heat path in both designs, the ring-structured and the V-shaped designs showed improved heat flow patterns for the V-shaped design.

Starting from a mechanically alloyed bismuth telluride powder, an annular thermoelectric generator was produced using a powder methodology. First step would be preparing the powder. Bismuth telluride powder exposed to air was observed to oxidize and performance to deteriorate.

Reducing oxides has been done by heating the powder to 350°C degrees and flowing a stream of hydrogen for six hours. Hydrogen reacts with oxygen particles forming water vapor at such elevated temperature. Process has been found to remove oxides. Oxide reduced powder is then stored in a glove box which has a preserved inert environment.

Extra measures were taken afterwards to ensure the powder would not be exposed to oxygen during the manufacturing process. The powder was pre-pressed inside a glove box, then moved outside the glove box while still inside the die to be pressed on a more powerful press to the target pressure. After pressing the sample it was moved back to the glove box where it was put in a Pyrex vial. Capped Pyrex vials filled with argon from the glove box are then moved to where they are vacuumed, filled with argon and sealed. Samples in the sealed vials are then placed in a Klin (furnace) to be sintered at temperatures ranging from 390°C to 430°C degrees for 48 hours. Sintering process includes slow ramp up and down of temperatures.

Prototypes were experimentally tested to study and characterize annular TEG modules. Manufacturing procedure parameters investigated were sintering temperature, pressing pressure, oxide reduction and geometry.

A novel experimental test facility was developed to characterize thermal and electrical performance of annular thermoelectric generator (TEG) modules for different thermal and electric loads. Measurement of output electric power, voltage, current, and thermal conductance can be made simultaneously as a function of load resistance and surface temperatures. Energy balance between the cold and hot legs shows 70% of data points falling within ± 10%.

A prototype was assembled from the oxide reduced samples, tested and compared to the prototype that was contaminated with oxygen. Treated prototype successfully restored its original performance before contamination. Comparing the effective measured Seebeck coefficient of both samples showed more than 26% improvement due to oxide reduction process in addition to less permanent growth experienced due to temperature elevation (quantified using an XRD test) and better mechanical strength (observed but not quantified).

Storing the powder in a glove box in an oxygen free environment slows down the oxidation process but the powder was slowly oxidized over time. Deteriorating performance of the powder due to oxidation was observed experimentally. Results indicates that a mean of oxide reduction has to be performed on the powder just before the pressing process to obtain targeted performance.

A TEG module assembly of 2 p-type V-shaped and 2 n-type ring-structured elements was manufactured, experimentally tested and compared against an assembly of two thermocouple with all four rings manufactured into a ring-structured proposed Min & Rowe (2007) design. The V-shaped annular thermoelectric generator module prototype was tested measuring a Seebeck coefficient of 190.75 μV/K after assembly compared to (Min & Rowe, 2007) prototype measuring a Seebeck coefficient of 145 μV/K and a theoretical Seebeck coefficient of 201 μV/K.

A simulation model was created to compare electrical and thermal behaviour for different TEG module geometries. One comparison was aimed to identify the main mechanism for the performance gain in experimental results for V-shaped TEG module design to ring-structured TEG design. ANSYS Workbench® simulation results show that V-shaped TEG module electrically outperforms the ring-structured design by 7% to 9% for a constant temperature and a constant heat flux boundary conditions respectively. Performance improvement was found consistent with temperature gradients and heat flow path pattern behaviour for both designs.

8.2 Proposed Future Work

This project is one step towards producing an annular thermoelectric module using a powder methodology that can potentially later be automated for high volume manufacturing. Many challenges were overcome during the project, which has been illustrated and discussed through this document. For the next phase of the project, the following are recommendations and challenges that should be considered or addressed:

- A fast and reliable mean of oxide reduction for the mechanically alloyed powder needs to be adopted and executed before every sample manufacturing process
- Increasing the pressing pressure to 420 MPa
- Chemical bonding of the TEG module elements to lower contact resistance significantly than current mechanical bonding
- Once the module is bonded, replacing conductor rings with metal deposition should be tested experimentally
- If the conductor ring is found to be essential to the module after chemical bonding process and experimental tests, a V-shaped rings design is recommended for both P and N types
- Eliminating the air gap between the TEG module ring and cold side chilled water pipe will lower the TEG cold side temperature and improve performance
- Moving to a Spark Plasma Sintering (SPS) or hot pressing to produce bismuth telluride rings will produce TEG module with better thermoelectric and mechanical properties in a fraction of the manufacturing time needed by the current process

A numerical study was done on a novel proposed variation of annular TEG design. In both the ring-structured design and the V-shaped design, it is assumed that heat would only flow radially. Therefore, optimally 100% of the heat would flow between the extrados and intrados of the thermoelectric ring not through the conductor ring which was found not to be achievable with the current design. A new design that adopts an axial heat flow concept was developed aiming to utilize 100% of the ring module material and is shown in Figure 81.

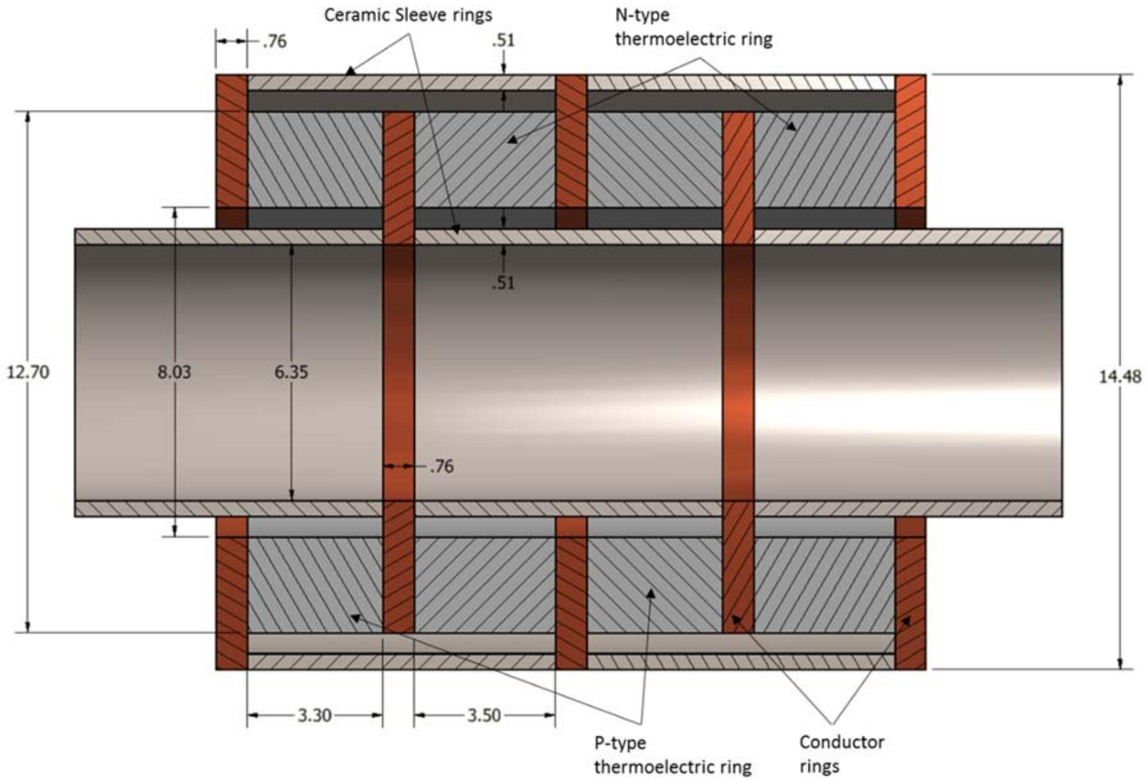

Figure 81 - Axial heat flow TEG module design

To reduce stresses on the module, the entire radial plane needs to be isothermal, therefore expanding equally. Introducing axial heat flow and axial temperature differential on the ring would reduce thermal stresses. To reduce mechanical stresses on the module, an outer and inner ceramic sleeve has been incorporated in the new design to withstand contact pressure from both the hot and cold sides.

ANSYS Workbench® simulation showed the axial heat flow design to produce 75% more open circuit voltage than the ring-structured module under a constant heat flux boundary condition with an almost three-fold the average temperature across the module. Although axial heat flow design performs better, there is a challenge in dissipating heat on the cold side. Further discussion about the proposed design is presented in Appendix B.

References

Antonova, E., & Looman, D. (2005). Finite elements for thermoelectric device analysis in ANSYS. In ICT 2005. 24th International Conference on Thermoelectrics, 2005. (pp. 215–218).

Arreguin-Zavala, J., Vasilevskiy, D., Turenne, S., & Masut, R. A. (2013). Microwave Sintering of Bi2Te3- and PbTe-Based Alloys: Structure and Thermoelectric Properties. Journal of Electronic Materials, 42(7), 1992–1998.

Bando, H., Koizumi, K., Oikawa, Y., Daikohara, K., Kulbachinskii, V. A., & Ozaki, H. (2000). The time-dependent process of oxidation of the surface of Bi 2 Te 3 studied by x-ray photoelectron spectroscopy. Journal of Physics: Condensed Matter, 12(26), 5607–5616.

Bergman, T. L., & Incropera, F. P. (2011). *Fundamentals of Heat and Mass Transfer*. John Wiley & Sons.

Böttner, H., Ebling, D. G., Jacquot, A., König, J., Kirste, L., & Schmidt, J. (2007). Structural and mechanical properties of spark plasma sintered n- and p-type bismuth telluride alloys. Physica Status Solidi (RRL) – Rapid Research Letters, 1(6), 235–237.

Britannica, T. E. of E. (n.d.). Thomas Johann Seebeck. Retrieved from http://www.britannica.com/EBchecked/topic/532353/Thomas-Johann-Seebeck

Callister, W., & Rethwisch, D. (2007). Materials science and engineering: an introduction.

Çengel, Y., Turner, R., Cimbala, J., & Kanoglu, M. (2008). Fundamentals of thermal-fluid sciences.

Cino, M. V. (2014, November 1). Design and Implementation of an Extensive Test Facility for Thermoelectric Materials and Devices. M.A.Sc. Thesis, McMaster University.

Cino, M. V. (2015). MATLS730 Course

Douglas, C. (1989). Giancoli, Physics for Scientists and Engineers.

Finnerty, D. A. (2013). The Development of Methodologies and a Novel Test Facility for the Characterisation of Thermoelectric Generators. M.A.Sc. Thesis, McMaster University.

Francombe, M. H. (1958). Structure-cell data and expansion coefficients of bismuth telluride. British Journal of Applied Physics, 9(10), 415–417.

Frankel, E. (1980). Dictionary of Scientific Biography. Charles Scribner's Sons, New York.

George, W. R., Sharples, R., & Thompson, J. E. (1959). The Sintering of Bismuth Telluride. Proceedings of the Physical Society, 74(6), 768–770

Gnielinski, V. (1976). New equations for heat and mass-transfer in turbulent pipe and channel flow. *International Chemical Engineering*, *16*(2), 359–368

Hyun, D.-B., Hwang, J.-S., Shim, J.-D., & Oh, T. S. (2001). No Title. Journal of Materials Science, 36(5), 1285–1291.

Ionescu, R., Jaklovszky, J., Nistor, N., & Chiculita, A. (1975). Grain size effects on thermoelectrical properties of sintered solid solutions based on Bi2Te3. Physica Status Solidi (a), 27(1), 27–34.

Jaklovszky, J., Ionescu, R., Nistor, N., & Chiculiţa, A. (1975). Grain Size Effect on the Figure of Merit of Sintered Solid Solutions Based on Bi2Te3. Physica Status Solidi (a), 27(2), 329–332.

Kauzlarich, Susan (Department of Chemistry, University of California, D. (2015). Synthesis and Characterization of Zintl Phases for Thermoelectric Applications. (invited talk) McMaster University, Hamilton. Private correspondence

Keshavarz Khorasgani, M. (2014, March 1). Synthesis and Characterization of Bismuth Telluride-Based Nanostructured Thermoelectric Composite Materials. Universite de Montreal.

Kosalathip, V., Kumpeerapun, T., Migot, S., Lenoir, B., & Dauscher, A. (2008). Thermoelectric Properties of BixSbyTezSew Nanocomposite Materials. In Advanced Materials Research (55–57), 809–812

Lee, J. S., Oh, T. S., & Hyun, D.-B. (2000). Thermoelectric properties of the hot-pressed (Bi0.2Sb0.8)2Te3 alloy with addition of BN and WO3 powders. Journal of Materials Science, 35(4), 881–887.

Min, G., & Rowe, D. M. (2007). Ring-structured thermoelectric module. Semiconductor Science and Technology, 22(8), 880–883.

Moffat, R. (1997). Notes on using thermocouples. Electronics Cooling, 3(1).

Navrátil, J., Starý, Z., & Plecháček, T. (1996). Thermoelectric properties of p-type antimony bismuth telluride alloys prepared by cold pressing. Materials Research Bulletin, 31(12), 1559–1566.

Poudel, B., Hao, Q., Ma, Y., Lan, Y., Minnich, A., Yu, Ren, Z. (2008). High-thermoelectric performance of nanostructured bismuth antimony telluride bulk alloys. Science, 320(5876), 634–638.

Ritter, J. J. (1994). A Novel Synthesis of Polycrystalline Bismuth Telluride. Inorganic Chemistry, 33(26), 6419–6420.

Ritter, J. J., & Maruthamuthu, P. (1995). Synthesis of Polycrystalline Bismuth Telluride by a Metal-Organo Complex Method. Inorganic Chemistry, 34(16), 4278–4280.

Rowe, D. M., & Min, G. (1998). Evaluation of thermoelectric modules for power generation. Journal of Power Sources, 73(2), 193–198.

Rowe, Francis, Taylor, Scherrer, H., & Scherrer, S. (2006). Thermoelectric Handbook–Macro to Nano.

Schmitz, A., Stiewe, C., & Müller, E. (2013). Preparation of Ring-Shaped Thermoelectric Legs from PbTe Powders for Tubular Thermoelectric Modules. Journal of Electronic Materials, 42(7),

Schultz, J. M., McHugh, J. P., & Tiller, W. A. (1962). Effects of Heavy Deformation and Annealing on the Electrical Properties of Bi2Te3. Journal of Applied Physics, 33(8), 2443–2450.

Silvester, P., & Ferrari, R. (1996). Finite elements for electrical engineers.

Weinberg, F. J., Rowe, D. M., & Min, G. (2002). Novel high performance small-scale thermoelectric power generation employing regenerative combustion systems. Journal of Physics D: Applied Physics, 35(13), L61–L63.

Weinberg, F. J., Rowe, D. M., Min, G., & Ronney, P. D. (2002). On thermoelectric power conversion from heat recirculating combustion systems. Proceedings of the Combustion Institute, 29(1), 941–947.

Yang, J. (2005). Potential applications of thermoelectric waste heat recovery in the automotive industry. In ICT 2005. 24th International Conference on Thermoelectrics, 2005. (pp. 170–174).

Yang, J. Y., Fan, X. A., Chen, R. G., Zhu, W., Bao, S. Q., & Duan, X. K. (2006). Consolidation and thermoelectric properties of n-type bismuth telluride based materials by mechanical alloying and hot pressing. Journal of Alloys and Compounds, 416(1-2), 270–273.

Zheng, J. (2008). Recent advances on thermoelectric materials. Frontiers of Physics in China, 3(3), 269–279.

Appendix A – Uncertainty Analysis

The Table below summaries the uncertainties of different parameters that were measured or calculated from measured data. Uncertainty was calculated in accordance with (Kline & McClintock, 1953). Temperature uncertainty was obtained from calibration curves. For both the hot and cold side each three thermocouples are in the same position and are averaged.

Parameter Symbol	Units	Description	Applicable Range of T_{Hot}	Absolute Uncertainty	Relative Uncertainty
$\delta T_{1a}, \delta T_{2a}, \ldots\ldots$	°C	Single thermocouple measurement	60°C to 125°C	± 0.30	
			125°C to 175°C	± 0.42	
			>175°C	± 0.52	
$\delta T_a, \delta T_b, \delta T_c$	°C	Average of three thermocouple measurements	60°C to 125°C	± 0.17	
			125°C to 175°C	± 0.24	
			>175°C	± 0.30	
δQ_w – see note 1	W	Heat transfer to the chilled water	60°C to 240°C	± 3.54	
$\delta Q_H/Q_H$	W	Heat transfer through the Hot block	60°C to 125°C		± 4.44%
			125°C to 175°C		± 4.28%
			>175°C		± 3.80%
δT_{Hot}	°C	Temperature of TEG hot side	60°C to 125°C	± 0.17	
			125°C to 175°C	± 0.24	
			>175°C	± 0.30	
δT_{Cold}	°C	Temperature of TEG cold side	60°C to 125°C	± 2.35	
			125°C to 175°C	± 2.31	
			>175°C	± 2.17	
$\delta \Delta T_{TEG}$	°C	Differential temperature over TEG module	60°C to 125°C	± 2.37	
			125°C to 175°C	± 2.35	
			>175°C	± 2.23	
$\delta T_{TEG\ avg}$	°C	Average temperature	60°C to 125°C	± 1.19	

		over the TEG module	125°C to 175°C	± 1.17	
			>175°C	± 1.12	
δα/α	μV/K	Seebeck Coefficient	60°C to 125°C		± 6.66%
			125°C to 175°C		± 4.30%
			>175°C		± 2.60%
δV	mV	Output measurement	60°C to 240°C		± 0.05%
δV̇	l/min	Water volumetric flow rate	60°C to 240°C		± 0.15%
Δk	W/(m. K)	Bismuth Telluride Thermal Conductivity	60°C to 240°C	± 0.05	

Table 13 - Uncertainty values for different parameters

Note 1: Heat transfer to chilled water was only calculated for mass flow rate of 0.2 Kg/min and less. Other experiments performed using a high flow rate (ranging 2 to 5 Kg/min), the difference of temperature between the water inlet and water outlet (ΔT_{water}) dropped down to be as low as 0.03°C while uncertainty of water measurement is + 0.17°C (average of three thermocouples). Therefore, heat transfer to chilled water at higher flow rate was not calculated.

Average of three thermocouples (Ta) were calculated from the equation:

$$\delta T_a = \frac{\delta T}{\sqrt{3}} \qquad \text{Eq. A. 1}$$

To calculate uncertainty for cold side heat transfer to water:

$$\frac{\delta Q_w}{Q_w} = \sqrt{\left(2\left(\frac{\delta T_a}{\Delta T}\right)^2 + \left(\frac{\delta m\prime}{m\prime}\right)^2\right)} \qquad \text{Eq. A. 2}$$

To calculate uncertainty for hot side heat transfer through hot block:

$$\frac{\delta Q_h}{Q_h} = \frac{\sqrt{2}}{\sqrt{3}}.\frac{\delta T_a}{\Delta T} \qquad \text{Eq. A. 3}$$

To calculate uncertainty for cold side temperature of the TEG module:

$$\delta T_{TEG-Cold} = \sqrt{\left(\delta T_H{}^2 + \left(\frac{ln(r_1/r_2)}{2\pi kt}\delta Q\right)^2 + \left(Q_H\frac{ln(r_1/r_2)}{2\pi t k^2}\delta k\right)^2\right)} \qquad \text{Eq. A. 4}$$

To calculate uncertainty for differential temperature over the TEG module:

$$\delta \Delta T_{TEG} = \sqrt{((\delta T_{TEG-Cold})^2 + (\delta T_H)^2)} \qquad \text{Eq. A. 5}$$

To calculate uncertainty for Seebeck coefficient:

$$\frac{\delta \alpha}{\alpha} = \sqrt{\left(\left(\frac{\delta \Delta T_{TEG}}{\Delta T_{TEG}}\right)^2 + \left(\frac{\delta V}{V}\right)^2\right)} \qquad \text{Eq. A. 6}$$

To calculate uncertainty for heat resistance of conviction to the water, conduction through the pipe and the air gap:

$$\frac{\delta R}{R} = \sqrt{\left(\left(\frac{\delta T_{TEG-Cold}}{\Delta T_{TEG}}\right)^2 + \left(\frac{\delta T_{TEG-avg}}{\Delta T_{TEG}}\right)^2 + \left(\frac{\delta Q}{Q}\right)^2\right)} \qquad \text{Eq. A. 7}$$

Appendix B – Axial Heat Flow Design

A third geometry was proposed for the next phase of the project. Its main concept is axial heat flow for better material utilization and lower thermal stresses. In both the ring-structured design and the V-shaped design, it is assumed that heat would only flow radially. Therefore, optimally 100% of the heat would flow from the extrados of the thermoelectric ring not from the side conductor ring in the axial direction which was found not possible, as shown in simulation results in chapter 7. A new design was developed with a better heat flow pattern aiming to utilize 100% of the ring module material.

For a TEG module, produced voltage can be increased by increasing the differential temperature across the module. For differential temperature between both sides to be as high as possible, the thermal resistance needs to be as high as possible for the module in the direction of heat flow. Doing a quick analytic calculation shows that for the current ring-structured design dimensions, heat flow resistance is higher in the axial direction than in the radial. Therefore, the developed design adopts an axial heat flow concept.

Either in real life application or experimentally, it is common for the hot and/ or the cold side heat exchanger to exert mechanical stresses on the TEG module to lower contact resistance between them. To protect the thermoelectric ring, a ceramic sleeve has been incorporated in the proposed design to withstand contact pressure on both the hot and cold sides.

When differential temperature difference is exerted on the module in the radial direction, hot on the extrados and cold on the intrados, material near the outer radius would be expanding more than material near the inner radius. Therefore the outer circumference would be increasing more than inner circumference, introducing thermal stresses on it and eventually introducing cracks starting from the inner circumference. To avoid such thermal stress, the radial plane needs to be isothermal to expand uniformly. Introducing the axial heat flow concept which would exert an axial temperature differential on the ring would achieve that.

For comparison reasons, same dimension and geometry of ring-structured thermoelectric rings mentioned earlier were kept, copper rings dimensions were altered (as shown in Figure 81) to allow equal temperature over the side of thermoelectric ring. Heat in this configuration would flow in the axial direction from the hot side copper ring to the cold side copper ring through the thermoelectric ring uniformly creating an axial temperature gradient.

Since heat and cold sources are in the radial direction of the TEG module and the design anticipates that heat should flow axially, insulation and air gaps were included in the model to verify the needed heat flow pattern is achievable.

Table 14 lists material assignments for the different model components,

Component	Material	Key properties	Value	Reference
Thermoelectric ring	Bismuth telluride	Thermal conductivity	1.358 Wm^{-1}K^{-1}	(Keshavarz Khorasgani, 2014)
		Seebeck coefficient	201 μVK^{-1}	(Min & Rowe, 2007)
		Electric resistivity	1.09 E-05 ohm m	
Conductor ring	Copper	Thermal conductivity	401 to 379 Wm^{-1}K^{-1}	(Callister & Rethwisch, 2007; Çengel et al., 2008; Douglas, 1989)
		Seebeck coefficient	1.5 E-06 VK^{-1}	
		Electric resistivity	1.7 E-08 to 5.19 E-08 ohm.m	
Hot Block cylinder	Stainless Steel	Thermal conductivity	15 to 17 Wm^{-1}K^{-1}	
Chilled water pipe	Aluminum	Thermal conductivity	144 to 175 Wm^{-1}K^{-1}	
Air gaps filling	Air	Thermal conductivity	0.024 Wm^{-1}K^{-1}	
Insulation layer	-estimated value-	Thermal conductivity	0.08 Wm^{-1}K^{-1}	-
Outer and inner sleeves for axial heat flow design	Ceramic-estimated value-	Thermal conductivity	0.04 Wm^{-1}K^{-1}	-

Table 14 - Material assignments for different model components

B. 1 Constant Heat Boundary Condition

A constant heat flow of 15 W was exerted on the outer side of the stainless steel block. On the inner surface of the pipe, a convection boundary condition was imposed to simulate a chilled water flow. Convection heat transfer coefficient was set to 10,000 W/(m^2K) on other models, estimating a chilled water flow of about 4.8 Kg/min. For the axial heat flow design, thermoelectric rings with same dimensions as the ring-structured module were used for comparison reasons resulting in a smaller chilled water pipe. Heat transfer coefficient was adjusted for that case to result in a constant Ah (Area (A) x heat transfer coefficient (h)) across all three modules, i.e. constant convection condition. Water temperature was set to be constant at 12^{o}C.

B .1.1 Temperature Distribution

Figure 82 show temperature gradient over the module under a 15 kW heat flow for the axial heat flow TEG module. The higher the temperature difference achieved across the module, the higher voltage produced, therefore the more power produced from the same thermoelectric ring. Under a constant heat flow boundary condition, differential temperatures of 57.14^{o}C, 62.19^{o}C and 85.78^{o}C were achieved across the TEG module for ring-structured, V-shaped and axial heat flow designs. A 50% improvement was achieved moving from a ring-structured design to an axial heat flow design which is a significant increase in the achieved differential temperature.

The absolute temperature values T_{hot} (hot side temperature) of the TEG module was observed to be 103.6^{o}C, 105.17^{o}C and 326.53^{o}C for the ring-structured, V-shaped and axial heat flow designs. The hot side temperature for the axial heat flow design seems to be very high. The cold side temperature was found to be 240.75^{o}C for the axial heat flow design, which is very high compared to 46.46^{o}C and 42.98^{o}C for the ring-structured and the V-shaped. It seems that although the design is exerting a very high heat resistance on the heat flow, which is beneficial for power production, the design lakes a better approach to dissipate heat on the cold side.

Heat is expected to flow radially for the circular and V-shaped designs and axially for the proposed axial heat flow design. No discrepancy was noticed in directional heat flux for the proposed design.

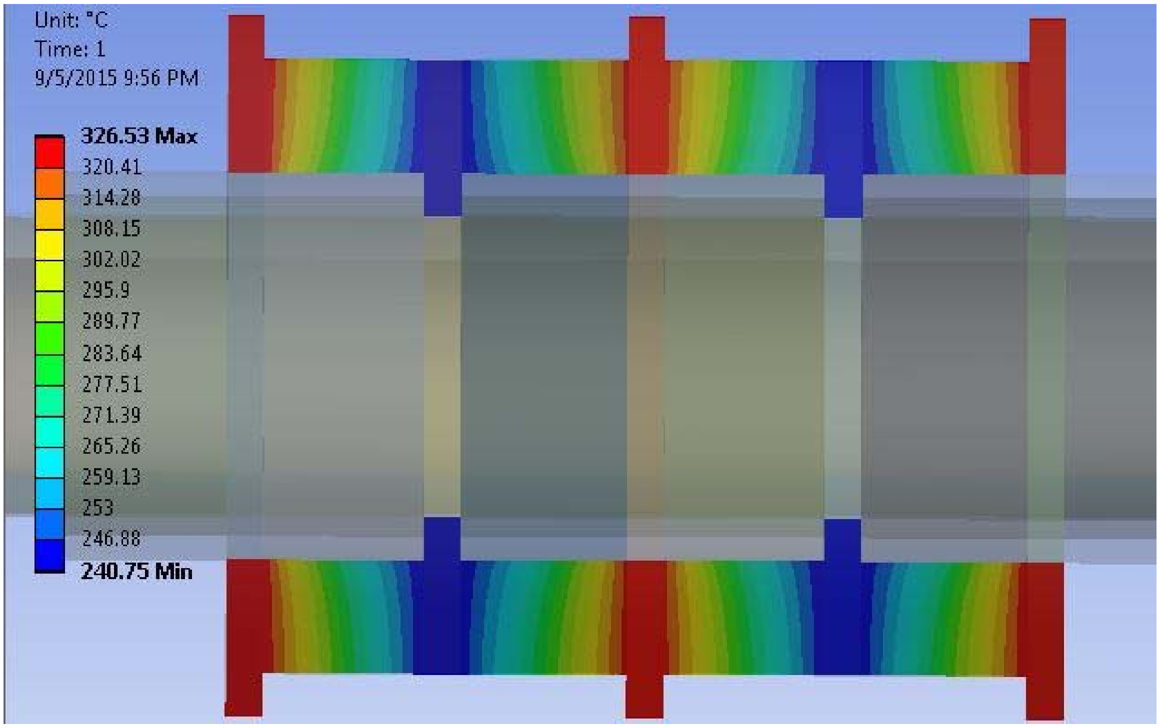

Figure 82 - Temperature distribution over axial heat flow TEG module under constant heat flow condition

B .1.2 Open Circuit Voltage

A voltage probe on one end of the TEG module was used while the other end is grounded. Open circuit voltage was measured in the simulation to compare the electrical performance of different modules. Electrical performance is dependent on the thermal behaviour, therefore electrical results can be roughly forecasted from earlier temperature gradient and material utilization behaviour. Open circuit voltage under a constant heat flow of 15W across the module measured 37.71 mV, 40.92mV and 66.07mV for the ring-structured, V-shaped and the axial heat flow TEG modules.

Axial heat flow design was found to produce 75% more open circuit voltage than the circular module under the same heat flow condition, but three-fold the average temperature across the module was observed. Although axial heat flow design performs better, a challenge in dissipating heat on the cold side exists.

B. 2 Constant Temperature Boundary Condition

A constant hot side temperature of 150°C was imposed on the outer side of the stainless steel block. On the inner surface of the pipe, a convection boundary condition was imposed to simulate a chilled water flow. Convection heat transfer coefficient was set to 10,000 W/(m^2K), estimating a chilled water flow of about 4.8 Kg/min. For axial heat flow design (3rd module), thermoelectric rings with the same dimensions as the ring-structured module was used for comparison resulting in a smaller chilled water pipe. Heat transfer coefficient was adjusted for that case to result in a constant Ah (Area (A) x heat transfer coefficient (h)) across all three modules, i.e. constant convection condition. Water temperature was set to be constant at 12^{o}C.

B .2.1 Temperature Distribution

Figure 83 shows temperature gradient axial heat flow TEG module. Under a constant hot side temperature boundary condition, differential temperatures of 75.7^{o}C, 81.11^{o}C and 34.52^{o}C were achieved across the TEG module for regular circular, V-shaped and axial heat flow designs. A 55% deterioration was observed moving to an axial heat flow design.

The cold side temperature was found to be 111.13^{o}C for the axial heat flow design, which is very high compared to 57.66^{o}C and 52.42^{o}C for the ring-structured and the V-shaped. Axial heat flow design lakes a better approach to dissipate heat on the cold side.

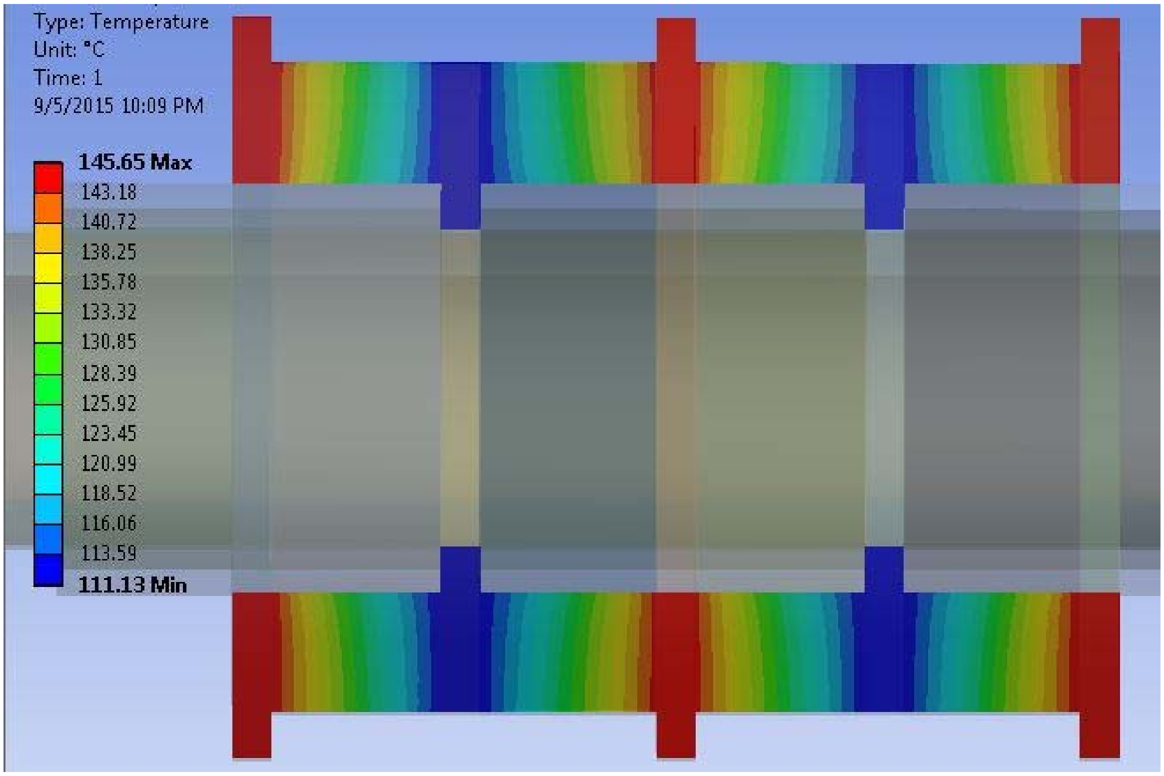

Figure 83 - Temperature distribution over axial heat flow TEG module under constant hot side temperature condition

Measuring heat flow through the module showed 19.882W, 19.572W and 5.314W flowing through ring-structured, V-shaped and axial heat flow TEG modules respectively. Axial heat flow design is showing 75% less heat flowing through the module. Same as discussed before, axial heat flow design lakes a better approach to dissipate heat on the cold side.

B .2.2 Open Circuit Voltage

Open circuit voltage under a constant hot side temperature of 150^{o}C imposed on the outer surface of the stainless steel block measured 50.01 mV, 53.4mV and 26.653mV for the circular, V-shaped and the axial heat flow TEG modules. Axial heat flow design was found to produce 50% less open circuit voltage than the circular module due to a relatively high cold side temperature.

Appendix C

The following table lists prototypes that were mentioned in chapter 6,

Date	Prototype Name	Geometry	Sintering Temperature (°C)	Sintering Hold Time (hour)	Pressing pressure (MPa)
05-20-2014	TEG-R-420-1-30-O	Ring-structured	420	1	30
05-23-2014	TEG-R-420-1-30-O	Ring-structured	420	1	30
06-04-2014	TEG-R-430-1-30-O	Ring-structured	430	1	30
07-24-2014	TEG-R-410-8-230-O	Ring-structured	410	8	230
08-20-2014	TEG-R-410-48-230-O	Ring-structured	410	48	230
10-03-2014	TEG-V-410/200-48-230-O	V-shaped	410	48	230
10-08-2014	TEG-V-410-48-230-O	V-shaped	410	48	230
10-24-2014	TEG-V-410-48-130-OF	V-shaped	410	48	130
12-17-2014	TEG-V-410-48-130-A+54	V-shaped	410	48	130
03-05-2015	TEG-V-430-48-130-OR	V-shaped	430	48	130
05-28-2015	TEG-V-390-48-130-A+84	V-shaped	390	48	130
06-16-2015	TEG-V-390-48-130-A+103	V-shaped	390	48	130

Table 15 - TEG prototypes experimentally tested and displayed in chapter 6

Appendix D

Antonova & Looman (2005) published the basic governing equations for solving ANSYS® thermoelectric models. The governing equation of heat flow is

$$\rho C \frac{\partial T}{\partial t} + \nabla . q = q' \qquad \textit{Eq. D. 1}$$

Where,

ρ : desity, kg/m^3

C= specific heat capacity, J(kg.K)

T= absolute temperature, K

q'= heat generation rate per unit volume, W/m^3

q = heat flux vector

The governing equation used for continuity of electric charge

$$\nabla . \left(J + \frac{\partial D}{\partial t} \right) = 0 \qquad \textit{Eq. D. 2}$$

Where,

J = electric current density vector, A/m^2

D = electric flux density vector, C/m^2

The set of thermoelectric constitutive equations

$$q = [\Pi]. J - [\lambda]. \nabla T \qquad \textit{Eq. D. 3}$$

$$J = [\sigma]. (E - [\alpha]. \nabla T) \qquad \textit{Eq. D. 4}$$

$$D = [\varepsilon]. E \qquad \textit{Eq. D. 5}$$

Where,

E = electric field intensity vector, V/m

[λ] = thermal conductivity matrix, w/m-K

[σ] = electrical conductivity matrix, S/m

[α] = Seebeck coefficient matrix, V/K

[Π] = T [α] = Peltier coefficient matrix, V

D = electric flux density vector, C/m^2

[ε] = dielectric permittivity matrix, F/m

E can be derived from

$$\mathrm{E} = -\nabla\varphi \qquad \textit{Eq. D. 6}$$

Where,

Φ = an electric scalar potential

Therefore,

$$\rho\mathrm{C}\frac{\partial \mathrm{T}}{\partial \mathrm{t}} + \nabla.([\Pi].\mathrm{J}) - \nabla.([\lambda].\nabla\mathrm{T}) = \mathrm{q}' \qquad \textit{Eq. D. 7}$$

$$\nabla.\left([\varepsilon].\nabla\frac{\partial\varphi}{\partial \mathrm{t}}\right) + \nabla.([\sigma].[\alpha].\nabla\mathrm{T}) + \nabla.([\sigma].\nabla\varphi) = 0 \qquad \textit{Eq. D. 8}$$

Galerkin FEM procedure (Silvester & Ferrari, 1996) can be applied to obtain the system of thermoelectric finite element equations.

An energy balance was checked for the module. The linear temperature profile at the outer surface of the TEG module (r=6.32mm) was subtracted from a second linear profile 0.4mm away from the surface (r=5.82mm) to calculate the radial conductive heat flux. Linear profiles are plotted in Figure 84. Local heat flux was calculated at each of the 200 nodes in the linear profile. The average heat flux was found to be 27.13 kW/m^2 and the total heat flow through the area was found to be 16.37 W. The total heat flow was found to be within 1% of the total heat flow from either the stainless steel block outer surface (constant temperature B.C.) or the inner pipe surface (convection B.C.).

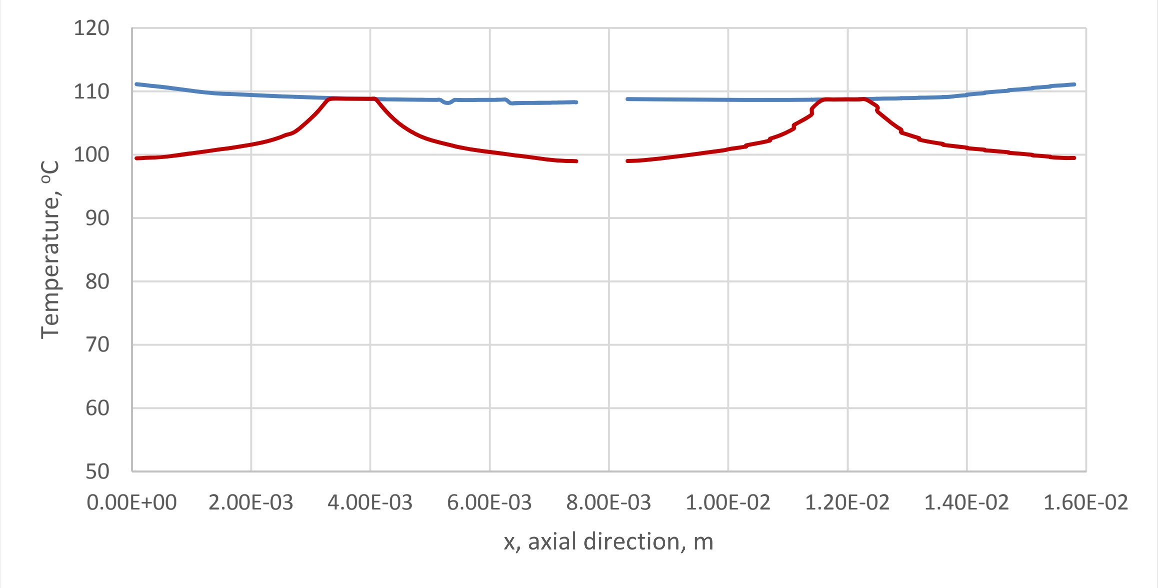

Figure 84 – Temperature profiles along the TEG module at different radiuses